Journal of Sensors

Cost-Effective Techniques for Sensors Technology

Lead Guest Editor: Almudena Rivadeneyra
Guest Editors: José Fernández-Salmerón, Aniello Falco, and Alfonso Salinas-Castillo

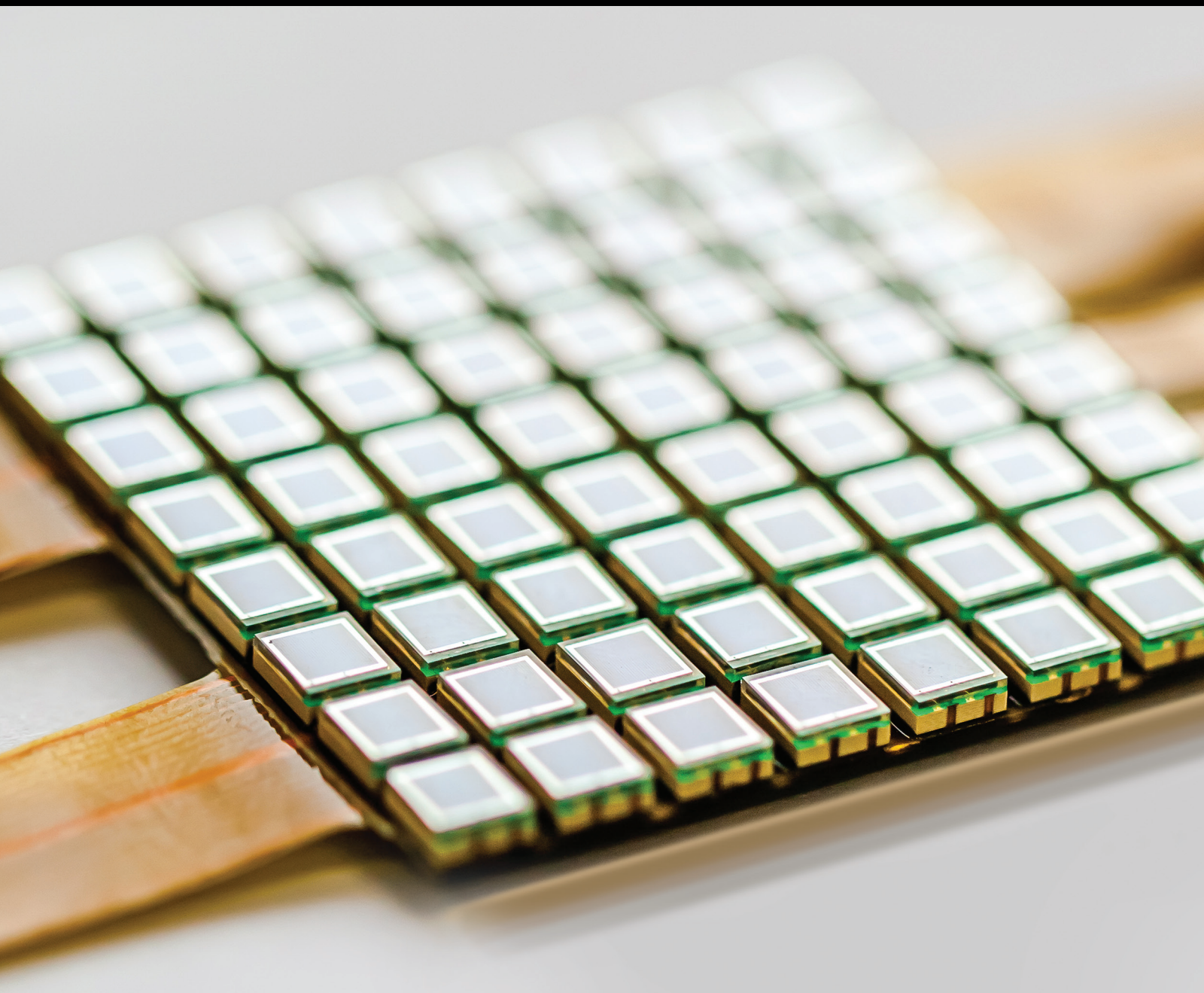

Cost-Effective Techniques for Sensors Technology

Journal of Sensors

Cost-Effective Techniques for Sensors Technology

Lead Guest Editor: Almudena Rivadeneyra
Guest Editors: José Fernández-Salmerón, Aniello Falco, and Alfonso Salinas-Castillo

Editorial Board

Contents

Hindawi
Journal of Sensors
Volume 2019, Article ID 2513493, 2 pages
https://doi.org/10.1155/2019/2513493

Editorial

Cost-Effective Techniques for Sensors Technology

Almudena Rivadeneyra,[1] **José F. Salmerón**,[1] **Aniello Falco**,[2] **and Alfonso Salinas-Castillo**[3]

[1]*Institute for Nanoelectronics, Technical University of Munich, Munich, Germany*
[2]*Faculty of Science and Technology, Free University of Bozen-Bolzano, Bolzano, Italy*
[3]*Department of Analytical Chemistry, University of Granada, Granada, Spain*

Correspondence should be addressed to Almudena Rivadeneyra; arivadeneyra@ugr.es

Received 31 December 2018; Accepted 31 December 2018; Published 17 March 2019

The concept of the Internet of Things (IoT) has opened a new paradigm in the interaction between objects and human beings. In the IoT, sensors and actuators are embedded in physical objects and interconnected through wired and wireless networks, creating new opportunities from hardware, software, and applications. In this regard, sensors play a fundamental role to extract valuable information of the object and its environment. The enormous significance of sensors for developing valuable applications in the IoT makes them a hot spot in research activities, where miniaturization, performance, and power consumption are the most important lines of development. It is expected that more than 25 billion connected "Things" will be in use by 2020. Each of this IoT entitites will contain at least one sensor; therefore, it is desirable to integrate cost-effective sensors. This special issue is aimed at serving as a major platform to facilitate the discussion and exchange of research ideas and technology development, encourage multidimensional knowledge sharing, and enhance research activities in investigating strategies to optimize techniques for sensor technology. In total, seven papers are included in this special issue and are summarized as follows.

Three papers describe different technologies to develop cost-effective sensors. In particular, shear force sensors fabricated by inkjet printing, piezoelectric sensors to detect adulteration in liquor, and spray-deposited temperature sensors. The shear force sensor consists of four miniaturized printed capacitors, exhibiting a normal force sensitivity of $S_z = 5.2$ fF/N and a shear force sensitivity of $S_y = 13.1$ fF/N in the force range from 0.1 N to 8 N. In the case of the piezoelectric sensor, authors demonstrate the capability of the quartz crystal resonator (QCR) to characterize samples of liquor at different concentrations of adulteration and classify them according to their viscosity, detecting fake liquor. The transparent nanomaterial-based temperature sensors are fabricated with different material combinations. The highest Seebeck coefficient is found for a junction made of carbon nanotubes (CNTs) on top of silver nanowires (AgNWs), whereas its efficiency in terms of power is the lowest because of the higher sheet resistance of the CNTs. The best combination for energy harvesting purposes would be poly(3,4-ethylenedioxythiophene) polystyrene sulfonate (PEDOT:PSS) and AgNWs.

The other four papers investigate different algorithms for optimizing sensing performance. First, a study on attenuation properties of surface wave of acoustic emission (AE) simulation source based on piezoelectric composite material (OPCM) sensing element is presented. Then, a robust data interpolation for incomplete acquisition in wireless sensor networks is shown based on back propagation artificial neural network operator. Also, an indoor and outdoor positioning system is described using a hybrid of support vector machine and deep neural network algorithms. The results also show that the proposed approach can provide scalable positioning, and 100% of the estimation accuracies are with errors less than 1 m and 1.9 m for indoor and outdoor positioning, respectively. Finally, an attack resistant VANETs

security algorithm (VANSec) is detailed in terms of trust computation error and normalized routing overhead to establish communication among vehicles (V2V) and road-side infrastructure (V2I).

Conflicts of Interest

The authors declare that there is no conflict of interest regarding the publication of this article.

Acknowledgments

The guest editors hope the information provided in this special issue is useful. Finally, we would like to thank the authors for an excellent contribution of their research works as well as very warmly acknowledged the reviewers for their valuable comments.

Almudena Rivadeneyra
José F. Salmerón
Aniello Falco
Alfonso Salinas-Castillo

Hindawi
Journal of Sensors
Volume 2019, Article ID 1864239, 11 pages
https://doi.org/10.1155/2019/1864239

Research Article

Shear-Force Sensors on Flexible Substrates Using Inkjet Printing

Andreas Albrecht,[1] **Mauriz Trautmann**,[1] **Markus Becherer**,[1] **Paolo Lugli**,[2] **and Almudena Rivadeneyra**[2]

[1]*Institute for Nanoelectronics, Technical University of Munich, Arcisstraße 21, 80333 Munich, Germany*
[2]*Free University of Bozen-Bolzano, Universitätsplatz 1 39100 Bozen-Bolzano, Italy*

Correspondence should be addressed to Andreas Albrecht; Andreas.albrecht@tum.de

Received 10 August 2018; Accepted 24 December 2018; Published 3 March 2019

Academic Editor: Franz L. Dickert

Printing techniques are a promising way of fabricating low-cost electronics without the need for masking and etching. In recent years, additive printing techniques, such as inkjet and screen printing, have been adopted to fabricate low-cost and large-area electronics on flexible substrates. In this work, a three-axial normal and shear force sensor was designed and printed that consists of four miniaturized, printed capacitors. The partially overlapping electrodes are arranged in a manner, so that force sensitivity in orthogonal directions is achieved. A silicone rubber is used as an elastic dielectric and spacer between the two electrodes. The base unit of this sensor has been fabricated using inkjet printing and characterized for normal and shear forces. The force response was investigated in a force range from 0.1 N to 8 N, the normal-force sensitivity was determined to be Sz = 5.2 fF/N, and the shear-force sensitivity was Sy = 13.1 fF/N. Due to its sensing range, this sensor could be applicable in tactile sensing systems like wearables and artificial electronic skins.

1. Introduction

Printed electronics possess the advantage of reducing the number of production steps by applying several components with similar process technologies. In contrast to conventional electronics manufacturing, sensors can be printed instead of assembled [1–3]. The present work deals with the development, fabrication, and characterization of a capacitive normal and shear force sensor. Such sensors could be used for basic force and pressure measurements [4, 5]. They could also be part of a tactile sensing system in robotics. Advanced robotic systems need reliable information about friction and strain when interacting with the environment and while handling objects [6–9]. Additionally, the ability of printed electronics to fabricate devices on flexible substrates could bring us a step closer to an artificial skin, which can be wrapped around the robot's surface [9–14].

In a previous work, we studied inkjet printing and photonic sintering for low-cost printing of electrodes and wiring [15]. Inkjet printing is able to print lines down to about 60 μm in width and can be conducted on a large range of flexible and low-cost substrates. Photonic sintering is a method that allows achieving highly conductive thin films on temperature-sensitive substrates with conductivities of up to 40% of the bulk conductivity [15] Therefore, these two technologies are well suited for the production of electrodes for sensors.

In this work, we want to focus on a capacitive three-axial shear-force sensor as an alternative to resistive force sensors [16, 17] that is applicable in an artificial skin. A common approach for building capacitive flat force sensors are the use of two parallel plates that change their distance upon pressure [9, 18, 19]. The gap can be air-filled [20] or consist of an elastic dielectric [21]. Lee et al. [20] have modified this principle to additionally recognize shear forces by introducing several capacitors.

Several research groups have tried to produce thin-film three-axial force sensors. Chase and Luo [22] showed a parallel plate capacitor approach with four capacitances that change in the overlapping area for exposure to shear forces and in distance for normal forces. Khan et al. [23] presented an all-screen printed flexible pressure (normal force) sensor

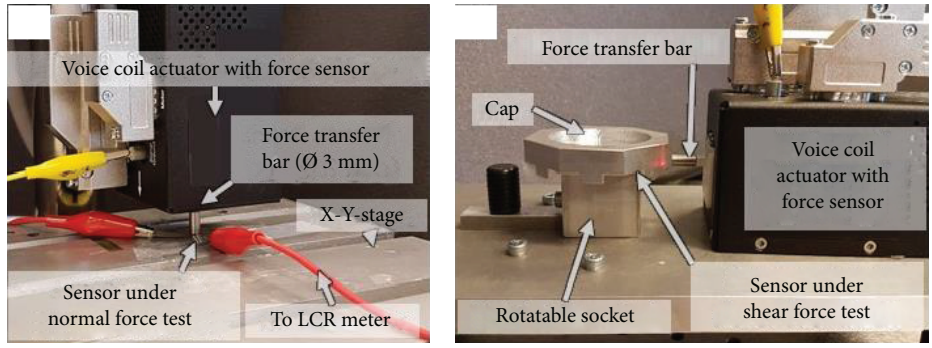

(a) (b)

Figure 1: Measurement setup for (a) normal forces and (b) shear forces. The metallic bar transfers the force generated by the voice coil actuator to the sensor and the cap where the sensor is fixed, respectively.

with a piezoelectric sensing principle. In their work, silver- (Ag-) based paste serves as a conductor for the electrodes. The piezoelectric material was polyvinylidene fluoride trifluoroethylene (P(VDF-TrFE)), which is a ferroelectric polymer that exhibits efficient piezoelectric and pyroelectric properties. The force response was characterized by the voltage readout.

A thin-film normal and shear force sensor was designed by Viry et al. [24] as well as Chase and Luo [22]. Their capacitive device senses normal and shear forces simultaneously. The operation is based on the deflection of a compressible filler material, which is sandwiched between two electrodes of a plate capacitor. Making a few adjustments, this design could be implemented using printing technologies.

A more advanced sensor design was reported by Dobrzynska and Gijs [25] using conventional semiconductor technology. Their capacitive approach is based on the deflection of an elastic dielectric spacer. They used multiple small capacitor areas leading to a higher sensitivity especially for shear force sensing. However, the fabrication of similarly small features is a challenging task using printed electronics techniques. A similar approach was used by Surapaneni et al. [26] who also developed a portable readout device.

In the present work, the basic idea of their sensor was adopted for printed electronics. The rest of the paper is structured as follows: in Section 2, we present the materials, the printing process, the elastic dielectric, and its application as well as the characterization tools used to produce the presented results. Section 3 discusses the design, a theoretical model thereof as well as the evaluation of the print quality and the measured electromechanical behavior of out sensors. In Section 4, we summarize the main findings and conclude the paper.

2. Materials and Methods

The shear-force sensors were fabricated on the transparent, coated Polyethylene Terephthalate (PET) film Screenfilm Waterbased (ColorGATE Digital Output Solutions GmbH, Germany). The film was developed for inkjet printing and has a nanoporous surface coating, a grammage of 210 gm^{-2}, and a thickness of 170 μm.

For inkjet printing, we used the nanoparticle-based silver ink DGP 40LT-15C (ANP Co., South Korea). The ink contains 35% silver nanoparticles dispersed in TGME ($C_8H_{18}O_4$), which is a polar solvent. The dispersion was carefully shaken by hand prior to filling into the cartridge. The curing temperature is indicated with 120-150°C, and the specific resistivity is 11-12 $\mu\Omega$cm. As the dielectric spacer of our sensor, we used a two-component screen-printable silicone paste, Alpatec 30191 (CHT R. Beitlich GmbH). The two components were mixed equally (1 : 1) in a small dish. After mixing, the paste can be used for one hour before hardening. Both components are highly transparent.

2.1. Inkjet-Printed Electrodes. The printer used in this work is a Dimatix DMP-2850 (Fujifilm Dimatix Inc., Santa Clara, USA). The cartridge and plate temperature was set to 55°C with a drop-spacing of 30 μm. This value guarantees a yield rate higher than 90% while the distance between consecutive electrodes is close enough. Reducing this spacing will increase the capacitance and sensitivity of our sensors, but it would reduce the reproducibility of the fabrication. With these settings, the fabrication of one electrode took about ten minutes. By using more than one nozzle, the printing time can be reduced, but the probability of a failure due to a blocking in one of the nozzles is much higher. Through the heat of the platen, the pattern was quickly dried. To make sure that all the solvents evaporated, the samples were additionally cured in an oven for 60 min at 60°C. The substrate limited the temperature as it started to buckle at higher values.

To improve the conductivity of the electrodes, we employed Intense Pulsed Light (IPL) sintering using a Sinteron 2010 (Xenon, US). A double pulse (period of 3 s) at 2.5 kV was used. The pulse lengths were 500 μs for the first pulse and 1000 μs for the second pulse, which were identified as good values in previous work [15]. The manufacturer measured a light intensity of 2.6-3.9 Jcm^{-2} for a single pulse at 830 J of electrical power. Our light intensity for both pulses is assumed to be approximately in this range as the employed pulses are about 300 J and 600 J, respectively.

2.2. Elastic Spacer. The Polydimethylsiloxane (PDMS) spacer was applied onto the inkjet-printed silver layer on the PET

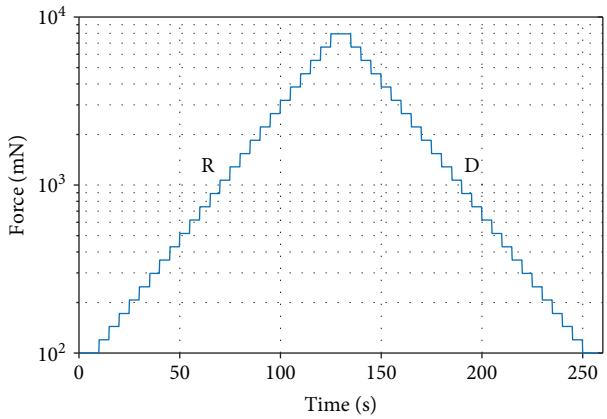

FIGURE 2: Force profile for normal and shear response measurements with increasing (R) force from 100 mN in steps of 20% up to 8 N and decreasing (D) force with the same values.

film using a stencil made of 75 μm thick Kapton film. After applying PDMS on both electrodes, they were placed on each other, aligned using dedicated marks, and baked on a hot plate at 60°C for about 30 min. To make sure that the electrodes did not detach, a slight pressure was exerted on the sample using a glass slide. In this way, we effectively used the PDMS as both an adhesive as well as a dielectric spacer of our sensor.

2.3. Characterization. Optical microscope images were taken with a Zeiss Germany Axio Lab.A1, equipped with a digital camera Axiocam 105. These images were used to assess the quality of the printed electrodes and to determine their lateral and longitudinal dimensions. Further, the drop diameter of the silver ink on the PET and Kapton substrates was identified.

The thickness of our printed electrodes and PDMS layer were measured with a DektakXT stylus surface profiler (Bruker Corporation, USA).

To generate the normal and shear force, we used the voice coil linear actuator V-275 PIMag (Physik Instrumente, Germany) with an integrated force sensor. Figure 1(a) shows the actuator mounted to a movable stage for the normal force application. The fabricated sensor was fastened to the table using double-sided adhesive tape. To reduce parasitic capacitive coupling, a 2.5 mm × 2.5 mm glass slide was put between the metallic bar of the motor and the sensor. The capacitance of a fabricated sensor was continuously recorded using an Agilent E4980A Precision LCR Meter (100 kHz, 0 V bias, and 1 V AC voltage). The characterization was automated by a LabVIEW program.

For the shear-force characterization, a different setup was developed and built using the same voice coil actuator. Figure 1(b) shows the measurement setup. The force is applied precisely on the sensor plane, thus parasitic forces are minimized. To characterize the samples from all directions, the socket can be rotated from -90 to +90. One side of the sensor is fixed with a double-sided tape to the socket and the other side to the cap. To route the wiring out, small grooves are milled into the bottom of the cap.

For the electromechanical characterization, we loaded the sensors with forces from 0.1 N to 8 N with incremental steps of 20% every five seconds, and subsequently, the force was reduced by the same factor. This was repeated three times. The time-force signal is shown in Figure 2. For the evaluation of the hysteresis, we differentiated between the rising and the declining edges of the profile. In Figure 2, the rising edges are labeled with R and the declining edges are denoted with D.

3. Results and Discussion

3.1. Sensor Design. The design of the sensor was defined by the requirements and technical capabilities described in the previous sections. Thus, we were looking for a sensor, which can be fabricated on flexible substrates, like Kapton and PET, using inkjet and screen printing.

In literature, different capacitive sensors were demonstrated. For example, Chase and Luo [22] presented a shear and normal force sensor where four squared electrodes form the bottom and a single squared electrode the top of the sensor. The operation was based on the deflection and compression of the filler layer between top and bottom electrodes.

The shear force and direction were then determined by calculating the ratios of the four single capacities. The downside of this configuration is that one only obtains very small delta in the capacitance, especially when measuring shear force. Therefore, the basic principles of the four individual capacitors had to be modified to achieve an improvement in sensitivity.

So, instead of using square electrodes, we chose an "E"-shaped pattern for both the top and the bottom electrode. This approach was presented by Dobrzynka and Gijs in 2013 [25]. Figure 3 shows the proposed design of our sensor that consists of four parallel-plate capacitors C1–C4. Each of them is formed between a finger structure at the bottom that has the size of one of the four squares plus a wiring. The bottom prints are shown in red and the top print is shown in yellow. The overlapping area of the top and the bottom print is shown in orange and the dielectric spacer (PDMS) is shown in beige. The contact pads on the right side are connected to each of the electrodes. They are all on one side and as far away from the sensing area as necessary to be able to contact them outside of our shear-force setup. The central one is connected to another contact pad that exists on both print patterns and links the top and bottom print next to the dielectric layer. We decided to number the capacitance values with the location of the contact pads from top to bottom. Thus, the counting starts with C1 in the top right corner and continues counterclockwise.

Figure 3 shows a magnification of a part of all electrodes on the right side and allows a closer look at the design of the electrodes. Again, the bottom electrodes are shown in red, the top electrodes in yellow, and the overlapping areas in orange. The top right and bottom left electrodes change the overlapping area of the fingers, if a force in the positive or negative x-direction is applied. For positive forces in the x-direction, the overlapping area increases for C1 and decreases for C3 and vice versa for negative forces. The

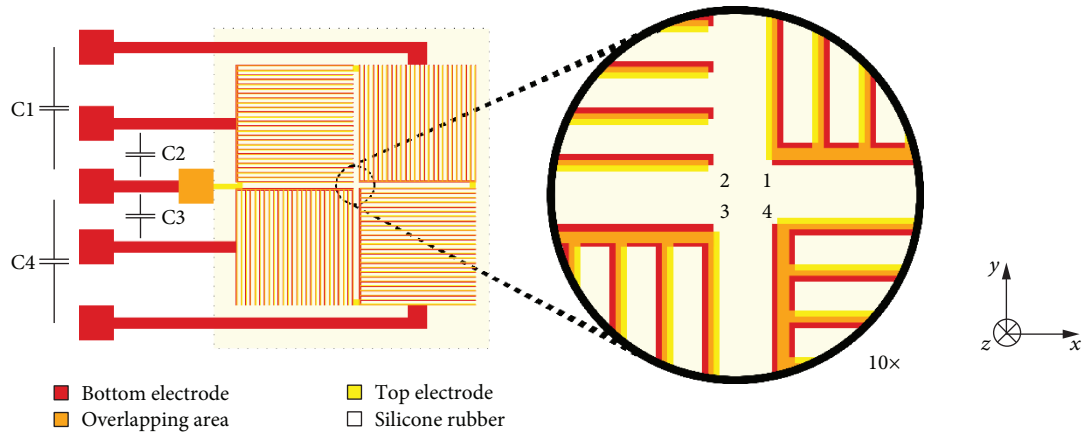

FIGURE 3: Design of our sensor with the four sectors that form the four capacitances $C_1 \ldots C_4$ that allow the differentiation of forces in x-, y-, and z-direction. In every sector, the top and bottom electrode is shifted in a different direction.

maximum allowable shift in the x-direction is half of the electrode width. For shear forces in the positive or negative y-direction, the overlapping area does not change until the same limits because the bottom electrodes are larger than the top ones. The top left (C2) and bottom right (C4) electrodes increase and decrease their overlapping area for a positive force in the y-direction. The tip of the fingers as can be seen in the magnification of C2 is extended for the bottom layer to allow a movement in x-direction without altering the overlap area.

The benefit of these "E"-shaped structures is that one obtains multiple edges, so that a deflection leads to a larger change in the parallel area of the capacitor. The top and bottom electrode are displaced by half of the finger width, so the initial capacitance amounts to 50% of the maximum capacitance. Two of the capacitors are x-axis--sensitive, and the other two are y-axis sensitive.

3.2. Theoretical Model. The sensor was modelled using a simple approach with a parallel-plate capacitor formed by the top and bottom electrodes. An exactly 50% overlap area for the fingers, a 100% overlap of the connection wires between the electrodes, and no influence of the wiring and the pads were assumed. The areas of all four squares were designed identically with the area $A = A_1 = A_2 = A_3 = A_4$. For the theoretical model, it is assumed that the dielectric is equally thick across the entire sensor with a thickness of d. Therefore, the basic parallel plate capacitor formula (1) can be employed for the initial capacitance C_0:

$$C_0 = \varepsilon_0 \varepsilon_r \frac{A}{d}. \tag{1}$$

A force in z-direction reduces the distance by Δd_z, which increases the capacitance of all four capacitors. A force in x-direction increases the area of the capacitor C_1 by ΔA_x and decreases the area of C_3 to the same extent while not influencing C_2 and C_4. The resulting capacitance values are shown in the first equation in (2). Similarly, a force in y-direction increases the overlap area of capacitor C_2 by ΔA_y and decreases the area of C_4 to the same extent and does not alter C_1 and C_3 as shown in the second equation:

$$\begin{aligned} C_{1/3} &= \varepsilon_0 \varepsilon_r \frac{A \pm \Delta A_x}{d - \Delta d_z}, \\ -C_{2/4} &= \varepsilon_0 \varepsilon_r \frac{A \pm \Delta A_y}{d - \Delta d_z}. \end{aligned} \tag{2}$$

The average value of all four capacitances cancels out all area changes caused by the x- and y-forces because we assumed that an area increase of one capacitor is equally compensated by an area decrease of another. The average value only depends on the distance between the parallel plates according to the normal force. This force in the z-direction can be determined by the change of the calculated average capacitance C_z divided by the initial capacitance C_0 as shown in (3). An approximation for small deflection of the top electrodes is given so it shows that for small forces, the behavior is almost linear:

$$C_z = \frac{1}{4} \sum_{n=1}^{4} C_n = C_0 \cdot \frac{d}{d - \Delta d_z} \approx C_0 \cdot \left(1 + \frac{\Delta d_z}{d}\right). \tag{3}$$

The increase or decrease of C_1 and C_3 for a shear force in the positive direction can be expressed in relation to C_z as shown in (4). Similarly, the expression for C_2 and C_4 is to be calculated.

$$C_{1/3} = \left(1 \pm \frac{\Delta A_x}{A}\right) \cdot C_z. \tag{4}$$

A subtraction of each pair of capacitance leads to an expression that reduces the z-dependence and can serve as indicators for the applied shear forces in the x- and y-direction as shown in (5). Each value remains constant for a force in the perpendicular direction because it is only depending on the changes in the area. If the subtraction of the pairs is divided by C_z, the z-direction dependence can be eliminated.

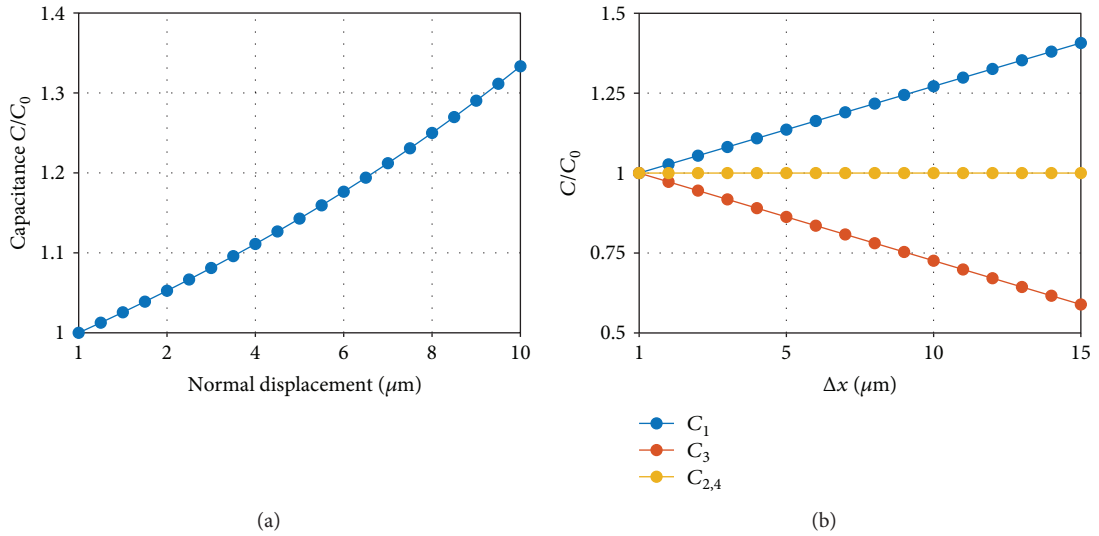

Figure 4: Theoretical model of the sensor's response on a displacement due to (a) normal force (z-direction) and (b) shear force in x-direction.

It has to be noted that the typical changes of the capacitance are low. A small noise caused by the measurement of the capacitance can introduce a large error when calculating this division.

$$C_x = \frac{(C_1 - C_3)}{2 \cdot C_z} = \frac{\Delta A_x}{A}, \qquad C_y = \frac{(C_2 - C_4)}{2 \cdot C_z} = \frac{\Delta A_y}{A}. \tag{5}$$

A numerical simulation was conducted to estimate the amount of the capacitance change and the influence of distance reduction to the difference of the capacitance pairs. One capacitor consists of 31 fingers with a width of about 60 μm and a length of 5.95 mm. The connecting bridge has an area of 1.22 μm^2. For the calculations, we took a 40 μm thick dielectric in idle position, and the relative dielectric permittivity of PDMS was taken as 2.5 [27]. The relative change of the capacitance due to a displacement of the top electrode by a certain distance on the impact of a normal force in the z -direction is depicted in Figure 4(a). It can be seen that the change for the capacitance is about linear for a small displacement until about 4 μm, which is 10% of the total dielectric's thickness. At a higher displacement, the capacitance changes at a higher rate according to (4) and is not linear anymore. As PDMS is hardly compressible, we assume that it is a reasonable assumption that the displacement is small enough to still follow a linear curve. Figure 4(b) shows the capacitance normalized to the initial capacitance C_0 for a shear force in the x-direction. As shown in (4), these are linearly dependent on the force-induced area change, which in turn is linear to the displacement. The slope of C_1 is positive with the same absolute slope than C_3, but C_3 is decreasing. A subtraction of C_3 from C_1 results in a linear relation, too.

A change in the normal force affects the change of the shown shear-force behavior. Figure 5 highlights the influence of the normal displacement on the individual capacitor values. Previous work by Dobrzynka and Gijs [25] neglected this effect. However, already small normal forces that compress the dielectric layer by a few percent can lead to a large error, especially when measuring small shear forces. This work suggests calculating the C_x and C_y values according to (5) to reduce this effect.

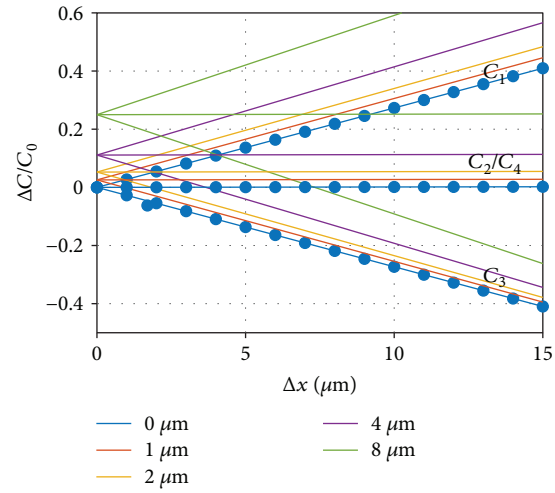

Figure 5: Calculated capacitance values for the individual capacitances for a shear load in x-direction at different constant z-forces.

3.3. Print Characterization. We decided to employ inkjet printing as the manufacturing technique for the sensor electrodes because the layer thickness is approximately one order of magnitude smaller than for screen printing. Figure 6 shows the inkjet-printed finger structures for two different finger geometries. On the left, fingers with a width of two drops to ensure the electrical connection even though one drop would not be correctly printed. A gap of three dots was necessary to achieve a suitable distance between the

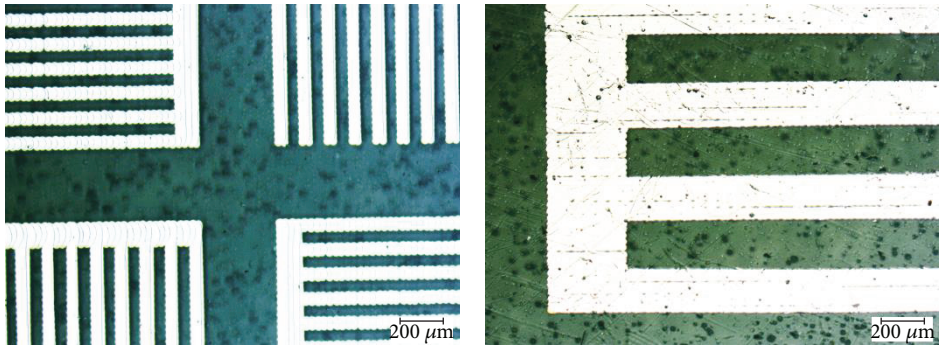

Figure 6: Inkjet-printed electrodes with different finger width of (a) 60 μm and (b) 210 μm. The silver can be seen bright while the substrate is dark. The individual droplets form small bulges on the edges.

fingers. A drop spacing of 20 μm was chosen to be ideal for the repro film (T6). Due to the drop gain of the inkjet-printed drops, the final finger width is about 60 μm and a gap of 40 μm. Still, inkjet printing of the pattern was not reproducible, and we obtained broken fingers on a regular basis. Furthermore, the alignment of the top and bottom electrodes turned out to be more difficult than initially assumed. These were the reasons why we decided to continue the work with larger fingers as shown in Figure 6(b). The finger width is 210 μm and the not perfectly printed areas on the fingers are of minor importance. To still reach relatively high capacitance values, we increased the length of the 22 fingers to 8.8 mm. The average thickness of the thin film forming the electrodes was 412 nm. It is about 1% of the thickness of the 40 μm thick dielectric that was applied by stencil printing on top of the fingers and can be neglected.

The profile measurement shown in Figure 7 was recorded perpendicular to the printing direction. We measured an average thickness of 412 nm. The green markers indicate drop rows where nozzle failure occurred and the thickness of the film is much lower. Since these gaps only appear locally, we expect them to have a small influence on the conductivity of the electrodes. However, the thickness of the silver layer greatly affects the conductivity of the electrodes. At this point, we were not aware of the fact that the conductivity could be a problem for the performance of the sensor.

The top electrode was then aligned on top of the bottom electrode and pressed with the help of a glass slide onto the still wet stencil-printed PDMS without squeezing it out of the defined area. For the first investigation, we built a sensor that only uses one-quarter of the final sensor. Figure 8 shows the assembled quarter of the sensor with the dielectric print across the entire area, except the left side of the photo where a white shadow is perceivable. Especially, the upper electrode, which is the bottom electrode, is shown milky because the employed PET film is milky. On contact with PET, it turns transparent and both electrodes can be clearly seen. The fabricated sensor was then contacted at the rectangular contact pads. Therefore, the overhanging PET foil was cut off, and the contact pads

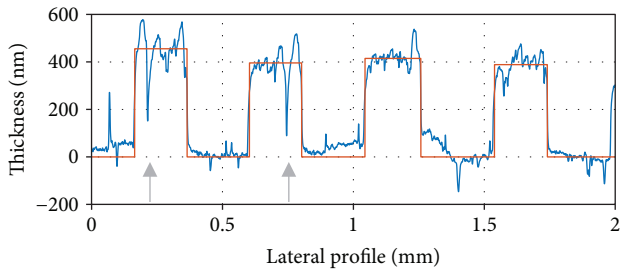

Figure 7: Profile of an inkjet-printed electrode. An average thickness of 412 nm was measured within the red marked areas. The spikes marked by green arrows may lead to an interruption of the conductive path.

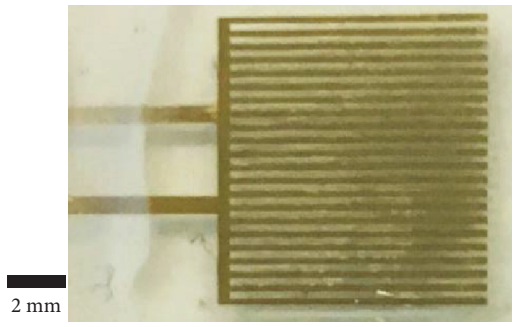

Figure 8: Optical image of one-quarter of the sensor including wiring.

were uncovered. To plug the sensor to the LCR meter, two small wires were attached by conductive epoxy.

3.4. Electromechanical Characterization. The results of the normal force sensing experiments are depicted in Figure 9. The data is collected from one characterization cycle, including three rising and declining force ramps. The blue lines represent the reference force signal and the red lines represent the capacitance signal. It can be seen that the capacitance signal follows the force signal accurately and reaches about 40 fF to 45 fF. A small delay between both signals was found that indicates a hysteresis. Furthermore, the sensor shows a small drift of several femtofarads. This is caused by the viscoelastic behavior of PDMS.

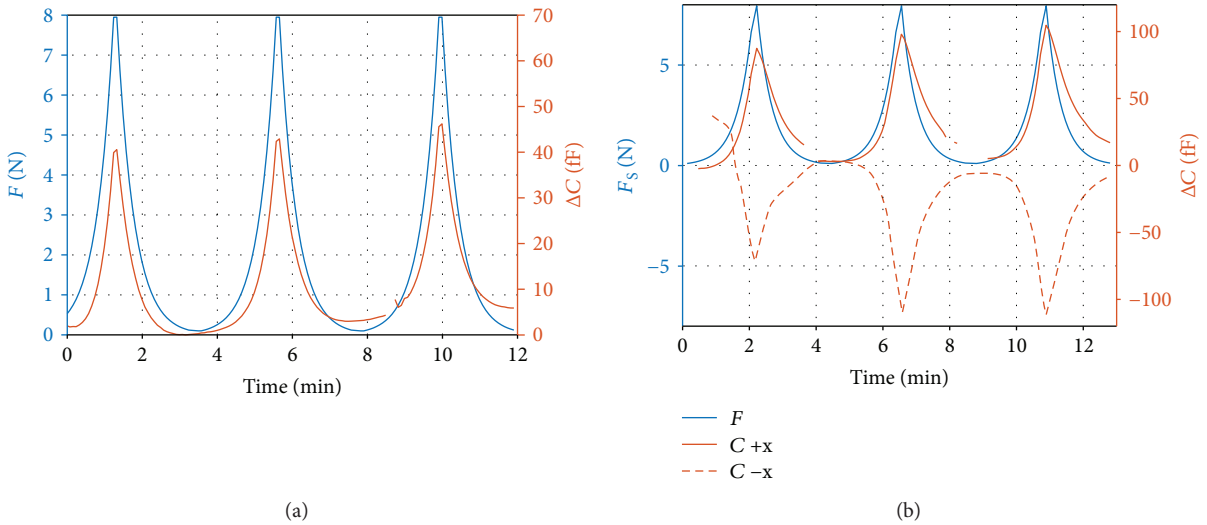

FIGURE 9: (a) Shows the capacitance response (red) to a normal force (blue) over time. (b) The solid red line corresponds to the capacitance change due to a force in $-x$-direction and the dashed line to the $+x$-direction.

The sensor was characterized with our custom-made shear-force setup. The sensor was put below the cap and characterized for shear forces in one direction. Then, the table was turned by 180° and the sensor could be characterized for the opposite force without removing it from the setup. In Figure 9(b), the solid line represents a shear force in -x-direction and the dashed lines a shear force in $+x$ -direction. The negative direction was conducted first and showed a very different behavior to the following cycles. Therefore, we aligned this signal according to the measured capacitance after finishing the first-force ramp. Then, the sensor responses were repeatable for the consecutive two ramps in the negative and three ramps in the positive x -direction. The sensor responses occur almost simultaneously with the application of a shear force, and the amplitudes for both directions are very similar (up to 110 fF and 105 fF for the negative and positive x-direction, respectively).

Due to the viscoelastic relaxation of the PDMS, the capacitance during unloading of the force is slightly higher than at loading. Furthermore, a permanent part is remaining that takes more time to vanish. This viscoelastic behavior is more pronounced for shear forces, for which the capacitance signal shows a small delay to the force signal. Especially for the unloading, the capacitance follows tens of seconds after the force signal. Again, a remaining part of the capacitance signal can be observed.

The response of the capacitance to different forces is investigated. For all the following plots, the solid lines represent the loading of the sensor and the dashed lines show the unloading response. To minimize errors in measurements and reduce noise, the 16 capacitance values which were measured immediately before a change in applied force have been considered in the analysis. Figure 10 shows that the response of the sensor is linear to the normal force, and it can be seen that the hysteresis is small. The sensitivity is approximately 5.2 ± 0.3 fF/N, which is rather small. The reason lies at the large area of the sensor. The area where the

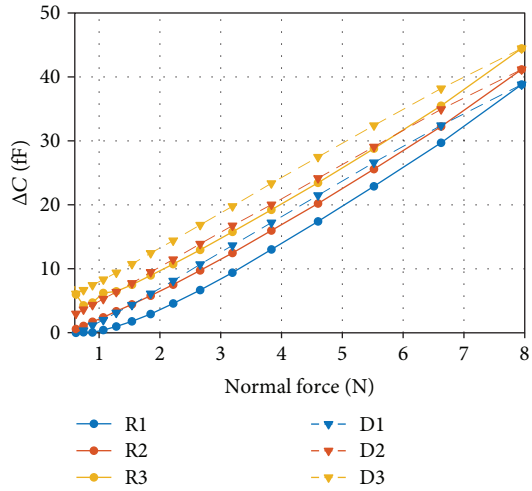

FIGURE 10: Characteristic of the sensor to three increasing (R: solid) and decreasing (D: dashed) cycles of normal force. A linear behavior was found. The drift of the signal can be explained by viscoelastic behavior of the PDMS and is reversed after a longer resting time.

PDMS was printed is approximately 2.5 × 2.5 cm^2 large, so that the maximal pressure was only about 12.8 kPa. Thus, the sensitivity to pressure is about 3.25 fF/kPa. As we only characterized one quarter of the sensor, the sensitivity for the full sensor would be four times higher, meaning 20.8 ± 0.6 fF/N or 13 fF/kPa. These values are slightly higher than in the work of Dobrzynska and Gijs [25], which achieved about 11 fF/kPa. The measured curve indicates that higher pressures would still produce higher changes in capacitance, but we were limited by our setup. Especially towards the higher force region, out sensor is linear in comparison to other sensors presented in the literature [25], and we expect that the linear region extends to a much higher force. Eventually, however, the sensor's capacitance values will saturate. The sensor's response is small and allows an accurate force

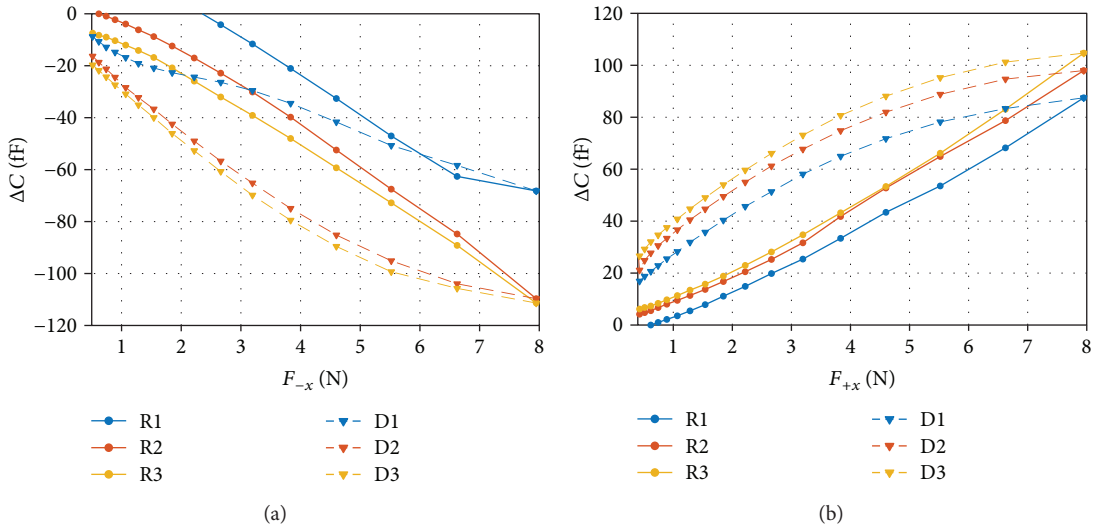

Figure 11: Characteristic of the sensor to three increasing (R) and decreasing (D) cycles of shear force in (a) $-x$-direction and (b) $+x$-direction. After the first force application, a linear behavior with a large hysteresis was found. The drift of the signal can be explained by viscoelastic behavior of the PDMS and is reversed after a longer resting time.

measurement with a temporal resolution in the order of seconds. The overall size in capacitance can be increased by increasing the area or lowering the thickness of the dielectric.

Figure 11 shows all measured values for forces in both $+x$- and $-x$-direction. The markers visualize every measured force value, which was kept for about 5 s, and the average force and capacitance values of the last four sampling points are marked. The blue markers show the first-force cycle, red the second, and yellow the third. Each rising (R) edge is shown by round markers connected by a solid line, and each decreasing (D) edge by triangular markers interconnected by a dashed line. The first measurement cycle is shown in blue in Figure 11(a) and deviates much from all other cycles. This is the reason why we decided to neglect it. Anyway, it must be shown to highlight the importance that the sensor may not work immediately as intended but may require one or more priming cycles. The following two cycles are close, with a slight drift towards lower capacitance values. This was observed for both positive and negative shear forces as well as for normal forces and is probably caused by viscoelastic deformations of the dielectric spacer PDMS. Our measurement times of only 5 s per point are rather short and does not allow the PDMS to completely adapt to the exerted force This may also be the reason for the large hysteresis with a width of up to 1.5 N. We expect that a longer measurement time would increase the absolute capacitance values of the rising edges and decrease the ones of the decreasing edges and decrease the hysteresis. Then, the capacitance values in respect to the force would follow a linear relation with a sensitivity between 12.3 ± 0.2 fF/N for the $+x$-direction and 13.8 ± 0.2 fF/N for the $-x$-direction. When the full sensor would be built, this would double to about 26 ± 0.4 fF/N because two capacitors will contribute to the measurements. Both shear-force sensitivities are similar and are about twice of the sensitivity values of the sensor in the work of Dobryzynska and Gijs [25], which was built similarly but without printing techniques.

The capacitance values of the sensors are considerably lower than the theoretical values. From the profilometer measurement, we know that the thickness of the PDMS layer is about 40 μm, and the area of the electrodes is about 44.4 mm^2. The theoretical capacitance value for 50% overlap is 12.3 pF. Our measured capacitance value was 6.82 pF and only half of the theoretical value. This capacitance would correspond to a distance of 96.8 μm. When checking the overlap of our sensor, we found that the overlap in resting state of about two-thirds (67%) was slightly higher than the desired value as can be seen in Figure 12(a) by the red-marked areas. This should lead to an even higher capacitance value of 16.5 pF. This significant deviation of the capacitance value originates most probably from some trapped air between the top electrode and the stencil-printed PDMS layer. Such trapped air bubbles are colored in red in the microscope images in Figure 12(b) and increase the average distance, but do not explain a factor of 2.5. Additionally, the lower relative permittivity of air (compared to PDMS) decreases the overall capacitance. The trapped air acts like a second capacitance connected in series. The capacitance as a function of the fraction of air $\chi = d_2/d$ and $d = d_1 + d_2$ is

$$C = \frac{\varepsilon_0 \varepsilon_r A}{d(1 - \chi + \varepsilon_r \chi)}. \quad (6)$$

Here, d is the total distance of the electrodes, d_1 denotes the thickness of the PDMS layer, and d_2 is the thickness of the air gap. For example, if the spacer contains 25% air and 75% PDMS the capacitance is reduced to 72.8% of its ideal value ($\chi = 0$, no trapped air). The combination of the higher distance due to trapped air and a lower effective permittivity leads to a reasonable relation of capacitance and distance.

The change in capacitance is originated by a displacement Δd of the top electrode with respect to the bottom

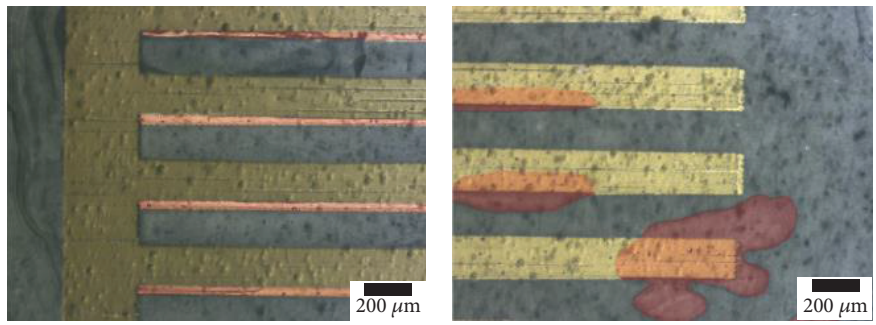

(a) (b)

Figure 12: (a) Overlapping area of the electrodes colored in red onto an optical microscope picture and (b) trapped air in the PDMS layer colored in red as well as for better visibility.

electrode. Using the distances in Table 1, we calculated the change in distance for each of the four possibilities that results in the measured change in capacitance of about 45 fF. The range of the calculated distance changes of less than a micrometer is reasonable since PDMS has a Poisson's ratio of almost 0.5 [28]. Therefore, the PDMS is only a little compressible as the lateral expansion is limited.

4. Discussion

In this work, a fully flexible, capacitive force sensor for two-axial force measurements has been developed by applying printed electronic technologies on a polymeric film. We successfully fabricated structured silver electrodes on PET foil by inkjet printing. We achieved a resolution with lines below 60 μm and an average thickness of about 500 nm. For a conducting layer, the inkjet-printed samples required an additional postproduction treatment. With photonic sintering, an ultrafast, selective, and cheap method was used to functionalize the thin films. PDMS, which was chosen for its good process ability and elastic properties, was found unsuitable for direct inkjet printing. Oxygen plasma treatment could be an effective way to overcome the hydrophobic surface properties of PDMS. Further research is required here. The most challenging task was to fabricate the stacked structure of a printed bottom electrode, a dielectric spacer, and a printed top electrode. The method of gluing the two printed sheets together to solve the problem was the best available. The main objective of this report to fabricate a printed normal and shear force sensor was achieved. By integrating this sensor into a 2-by-2 arrangement of four sensors, simultaneous normal and shear forces (three-axial) can be measured. Due to trapped air in the dielectric spacer, the experimental capacitance values were distinctly lower than the theoretical predictions.

In the force range of 0.1 to 8 N, we could find a linear relationship between the capacitance values and the exerted normal and shear forces. For normal forces, a sensitivity of 5.2 fF/N was determined and for shear forces, it was 13.1 fF/N. These values were measured only for one-quarter of the sensor of an area of about 80 mm^2. When employing four of the sensors in a different orientation, the shear force sensitivity can be doubled to 26.2 fF/N, and the normal force sensitivity quadrupled to 20.8 fF/N. These are comparable to other sensors in literature and have the main advantage that only printing techniques are employed. Only additive deposition techniques were used and the only difficult step is the alignment of both electrodes. The reduction of the finger width to the planned 60 μm or eventually 40 μm would either allow more fingers or a smaller sensor. The first would have an approximate increase of the sensitivity closer to the picofarad region. The second would decrease the area and increase the sensitivity with respect to forces as the local pressures are higher. Another improvement could be the use of structured dielectrics as in the previous section to reduce the stiffness of the dielectric. All of the materials and methods used here are low-cost and cause a very small amount of chemical waste, especially when compared to conventional semiconductor processes. This allows the production of sensors on large and flexible substrates as they are needed for artificial skins. Such skins may be employed in advanced humanoids as well as for patients without sensing capabilities on parts of their body.

Table 1: Comparison of the theoretical and measured capacitance values C_0 and their change ΔC_0, the thickness of the dielectric spacer $d_{0,}$ and the deflection Δd. Bold values are calculated from the other columns.

	C_0 (pF)	ΔC_0 (fF)	Overlap	ε_r	d_0 (μm)	Δd (nm)
Ideal 50%	**12.3**	45	50%	2.5	40.0	**146**
Ideal 67%	**16.5**	45	67%	2.5	40.0	**109**
Sensor	6.82	45	67%	2.5	**96.8**	**635**
S (25% air)	6.82	45	67%	**1.8**	**69.7**	**457**

Data Availability

The data used to support the findings of this study are available from the corresponding author upon request.

Conflicts of Interest

The authors declare no conflict of interest.

Authors' Contributions

A. Albrecht and P. Lugli contributed in the conceptualization of the study. A. Albrecht created the methodology, wrote and prepared the original draft, and did the visualization of the study. P. Lugli, M. Becherer, and M. Trautmann gathered resources. A. Rivadeneyra, P. Lugli, and M. Becherer wrote, reviewed, and edited the paper. P. Lugli and A. Rivadeneyra supervised the study. P. Lugli and M. Becherer acquired the funds for the study.

Acknowledgments

The authors want to thank Prof. Cheng of the Technical University of Munich (TUM) for the use of their lab to produce the inkjet-printed patterns used in this work and Prof. Wagner of the same university for the use of their workshop to build the two force setups. This work was partially supported by the Deutsche Forschungsgemeinschaft (DFG) within the German Excellence Initiative through the cluster of excellence "Nanosystems Initiative Munich" (NIM) and the Technical University of Munich (TUM) Graduate School.

References

[1] D. Lupo, W. Clemens, S. Breitung, and K. Hecker, "OE-A roadmap for organic and printed electronics," in *Applications of Organic and Printed Electronics*, Integrated Circuits and Systems, E. Cantatore, Ed., Springer, Boston, MA, USA, 2013.

[2] G. Nisato, D. Lupo, and S. Ganz, *Organic and Printed Electronics: Fundamentals and Applications*, CRC Press, 2016.

[3] M. Nir, D. Zamir, I. Haymov, and L. Ben-Asher, "Electrically conductive inks for inkjet printing," in *The Chemistry of Inkjet Inks*, S. Magdassi, Ed., pp. 225–254, 2010.

[4] A. Albrecht, M. Trautmann, M. Becherer, P. Lugli, and A. Rivadeneyra, "Multi-layer printed shear force sensor on flexible substrates," in *ALLSENSORS 2018, The Third International Conference on Advances in Sensors, Actuators, Metering and Sensing*, pp. 70–75, Rome, Italy, 2018.

[5] A. Albrecht, *Printed Sensors for the Internet of Things*, Technische Universität München, 2018.

[6] E. S. Hwang, J. H. Seo, and Y. J. Kim, "A polymer-based flexible tactile sensor for both normal and shear load detections and its application for robotics," *Journal of Microelectromechanical Systems*, vol. 16, no. 3, pp. 556–563, 2007.

[7] R. Pfeifer, M. Lungarella, and F. Iida, "The challenges ahead for bio-inspired 'soft' robotics," *Communications of the ACM*, vol. 55, no. 11, p. 76, 2012.

[8] N. Lu and D.-H. Kim, "Flexible and stretchable electronics paving the way for soft robotics," *Soft Robotics*, vol. 1, no. 1, pp. 53–62, 2014.

[9] R. S. Dahiya, P. Mittendorfer, M. Valle, G. Cheng, and V. J. Lumelsky, "Directions toward effective utilization of tactile skin: a review," *IEEE Sensors Journal*, vol. 13, no. 11, pp. 4121–4138, 2013.

[10] R. S. Dahiya, G. Metta, M. Valle, and G. Sandini, "Tactile sensing-from humans to humanoids," *IEEE Transactions on Robotics*, vol. 26, no. 1, pp. 1–20, 2010.

[11] J. A. Rogers, T. Someya, and Y. Huang, "Materials and mechanics for stretchable electronics," *Science*, vol. 327, no. 5973, pp. 1603–1607, 2010.

[12] T. Sekitani and T. Someya, "Stretchable organic integrated circuits for large-area electronic skin surfaces," *MRS Bulletin*, vol. 37, no. 3, pp. 236–245, 2012.

[13] G. Schwartz, B. C. K. Tee, J. Mei et al., "Flexible polymer transistors with high pressure sensitivity for application in electronic skin and health monitoring," *Nature Communications*, vol. 4, no. 1, p. 1859, 2013.

[14] M. Kaltenbrunner, T. Sekitani, J. Reeder et al., "An ultra-lightweight design for imperceptible plastic electronics," *Nature*, vol. 499, no. 7459, pp. 458–463, 2013.

[15] A. Albrecht, A. Rivadeneyra Torres, J. F. Salmerón, A. Abdellah, and P. Lugli, "Inkjet printing and photonic sintering of silver and copper oxide nanoparticles for ultra-low-cost conductive patterns," *Journal of Materials Chemistry C*, vol. 4, no. 16, pp. 3546–3554, 2016.

[16] W. Y. Chang, T. H. Fang, H. J. Lin, Y. T. Shen, and Y. C. Lin, "A large area flexible array sensors using screen printing technology," *IEEE/OSA Journal of Display Technology*, vol. 5, no. 6, pp. 178–183, 2009.

[17] C. L. Choong, M. B. Shim, B. S. Lee et al., "Highly stretchable resistive pressure sensors using a conductive elastomeric composite on a micropyramid array," *Advanced Materials*, vol. 26, no. 21, pp. 3451–3458, 2014.

[18] R. S. Dahiya and M. Valle, *Robotic Tactile Sensing : Technologies and System*, Springer, 2013.

[19] M. R. Cutkosky, R. D. Howe, and W. R. Provancher, "Force and tactile sensors," in *Springer Handbook of Robotics*, B. Siciliano and O. Khatib, Eds., pp. 455–476, Springer, Berlin, Heidelberg, 2008.

[20] H.-K. Lee, J. Chung, S.-I. Chang, and E. Yoon, "Normal and shear force measurement using a flexible polymer tactile sensor with embedded multiple capacitors," *Journal of Microelectromechanical Systems*, vol. 17, no. 4, pp. 934–942, 2008.

[21] S. C. B. Mannsfeld, B. C. K. Tee, R. M. Stoltenberg et al., "Highly sensitive flexible pressure sensors with microstructured rubber dielectric layers," *Nature Materials*, vol. 9, no. 10, pp. 859–864, 2010.

[22] T. A. T. A. Chase and R. C. R. C. Luo, "A thin-film flexible capacitive tactile normal/shear force array sensor," in *Proceedings of IECON '95-21st Annual Conference on IEEE Industrial Electronics*, pp. 1196–1201, Orlando, FL, USA, 1995.

[23] S. Khan, L. Lorenzelli, and R. S. Dahiya, "Screen printed flexible pressure sensors skin," in *25th Annual SEMI Advanced Semiconductor Manufacturing Conference (ASMC 2014)*, pp. 219–224, Saratoga Springs, NY, USA, 2014.

[24] L. Viry, A. Levi, M. Totaro et al., "Flexible three-axial force sensor for soft and highly sensitive artificial touch," *Advanced Materials*, vol. 26, no. 17, pp. 2659–2664, 2014.

[25] J. A. Dobrzynska and M. A. M. Gijs, "Polymer-based flexible capacitive sensor for three-axial force measurements," *Journal of Micromechanics and Microengineering*, vol. 23, no. 1, article 015009, 2013.

[26] R. Surapaneni, Q. Guo, Y. Xie, D. J. Young, and C. H. Mastrangelo, "A three-axis high-resolution capacitive tactile imager system based on floating comb electrodes," *Journal*

of Micromechanics and Microengineering, vol. 23, no. 7, article 075004, 2013.

[27] J. E. Mark, *Polymer Data Handbook*, Oxford University Press, 2009.

[28] S. Yao and Y. Zhu, "Nanomaterial-enabled stretchable conductors: strategies, materials and devices," *Advanced Materials*, vol. 27, no. 9, pp. 1480–1511, 2015.

Hindawi
Journal of Sensors
Volume 2018, Article ID 7853695, 16 pages
https://doi.org/10.1155/2018/7853695

Research Article

A Robust Data Interpolation Based on a Back Propagation Artificial Neural Network Operator for Incomplete Acquisition in Wireless Sensor Networks

Mingshan Xie[1,2] **Mengxing Huang**[1] **Yong Bai**[1] **Zhuhua Hu**[1] **and Yanfang Deng**[1]

[1]*State Key Laboratory of Marine Resource Utilization in South China Sea, College of Information Science & Technology, Hainan University, Haikou 570228, China*
[2]*College of Network, Haikou University of Economics, Haikou 571127, China*

Correspondence should be addressed to Yong Bai; bai@hainu.edu.cn

Received 13 July 2018; Revised 7 October 2018; Accepted 16 October 2018; Published 20 December 2018

Guest Editor: Aniello Falco

The data space collected by a wireless sensor network (WSN) is the basis of data mining and data visualization. In the process of monitoring physical quantities with large time and space correlations, incomplete acquisition strategy with data interpolation can be adopted to reduce the deployment cost. To improve the performance of data interpolation in such a scenario, we proposed a robust data interpolation based on a back propagation artificial neural network operator. In this paper, a neural network learning operator is proposed based on the strong fault tolerance of artificial neural networks. The learning operator is trained by using the historical data of the data acquisition nodes of WSN and is transferred to estimate the value of physical quantities at the locations where sensors are not deployed. The experimental results show that our proposed method yields smaller interpolation error than the traditional inverse-distance-weighted interpolation (IDWI) method.

1. Introduction

The purpose of a wireless sensor network (WSN) is to obtain the data field or data space of the physical world as accurate and complete as possible through acquisition technology. It is an important part of forecasting, simulation, and prediction to obtain the spatial-temporal distribution information of the monitored object accurately. However, in some scenarios, WSN can take an incomplete acquisition strategy, due to the development cost of the sensing device and the deployment environment factor, energy limitation, equipment aging, and other factors, or because it is not necessary to collect the data in each corner of the monitoring area. The incomplete acquisition strategy is divided into three cases: (a) spatial incomplete acquisition strategy—the actual collected area is smaller than the interested area or the actual acquisition location set is part of the entire acquisition locations in the monitoring area; (b) temporal incomplete acquisition strategy—the actual collection time period is less than the time period in which all devices work. The sleeping schedule is a temporal incomplete acquisition strategy. (c) Incomplete acquisition of attributes—the actual physical quantities collected are less than the interested physical quantities.

Because the constraints of interpolation are relatively small, it is more appropriate to use the interpolation algorithm to complete or refine the entire data space in the case of spatial incomplete acquisition. The interpolation completion algorithm takes advantage of the strong correlation between the data in the data space. At present, data interpolation is the main method to complement the data space of the entire region. In [1], Ding and Song used the linear interpolation theory to evaluate the working status of each node and the whole network coverage case. In [2], Alvear et al. applied interpolation techniques for creating detailed pollution maps.

However, WSN is often affected by many unfavorable factors. For example, it is usually arranged in a harsh

environment, the node failure rate is relatively high, it is very difficult to physically replace the failure sensor, and the wireless communication network is susceptible to interference, attenuation, multipath, blind zone, and other unfavorable factors. Data is prone to errors, security is not guaranteed, etc. Therefore, WSN data interpolation technology must be highly fault tolerant to ensure high credibility and robustness of the completed data space [3].

Data interpolation is used to predict and estimate the information at an unknown location by means of using known information. Transfer learning opens up a new path for data interpolation. The goal of transfer learning is to extract useful knowledge from one or more source domain tasks and apply them to new target tasks. It is essentially the transfer and reuse of knowledge. Transfer learning has gradually received the attention of scholars. In [4], the authors are motivated by the idea of transfer learning. They proposed a novel domain correction and adaptive extreme learning machine (DC-AELM) framework with transferring capability to realize the knowledge transfer for interference suppression. To improve the radar emitter signal recognition, Yang et al. use transfer learning to obtain the robust feature against signal noise rate (SNR) variation in [5]. In [6], the authors discuss the relationship between transfer learning and other related machine learning techniques such as domain adaptation, multitask learning, and sample selection bias, as well as covariate shift.

Artificial neural networks have strong robustness. One of the requirements to ensure the accuracy of transfer learning is the robustness of the learning algorithm. Many scholars have combined the neural artificial network with transfer learning. In [7] Pan et al. propose a cascade convolutional neural network (CCNN) framework based on transfer learning for aircraft detection. It achieves high accuracy and efficient detection with relatively few samples. In [8], Park et al. showed that the transfer learning of the ImageNet pretrained deep convolutional neural networks (DCNN) can be extremely useful when there are only a small number of Doppler radar-based spectrogram data.

The research aim of data interpolation of WSN is to complete the data space of the entire monitoring area by using the limited data of the acquisition node to estimate the data at the locations where sensors are deployed. However, data errors of WSN due to various reasons have great impact on the accuracy of data interpolation. Due to the strong robustness of an artificial neural network, an artificial neural network learning operator is generated by using historical measurement data of limited data acquisition nodes in this paper. At the same time, this paper applies the learning property of the artificial neural network to the inverse-distance-weighted interpolation method, which is conducive to improving precision and accuracy of data interpolation. On the basis of analyzing the demand of network models, this paper proposes a robust data interpolation based on a back propagation artificial neural network operator for incomplete acquisition in wireless sensor networks. The detailed steps of the algorithm are discussed in detail, and the algorithm is analyzed based on the MATLAB tool and the measured data provided by the Intel Berkeley Research laboratory [9]. The experimental results are good evaluations of the fault-tolerant performance and lower error of our proposed method.

The main contributions of this paper are as follows:

(1) Aiming at the data loss and disturbance error, we propose a fault-tolerant complementary algorithm based on the robustness of the artificial neural network

(2) We combine the artificial neural network with the inverse-distance-weighted interpolation algorithm to obtain a novel back propagation artificial neural network operator

(3) We use the inverse tangent function to reconcile the relationships among multiple prediction values

The rest of the paper is organized as follows. In Section 2, we summarize the related work. Section 3 introduces the interpolation model in the condition of data error. Section 4 presents how to construct the learning operator set of data acquisition nodes. Section 5 elaborates how to generate the interpolation by the method based on the back propagation artificial neural network operator. We will show the experimental results of our proposed methods compared with the inverse-distance-weighted interpolation in Section 6. The conclusions are given in Section 7.

2. Related Works

2.1. The Inverse-Distance-Weighted Interpolation Method. The inverse-distance-weighted interpolation (IDWI) method is also called "inverse-distance-weighted averaging" or the "Shepard Method." The interpolation scheme is explicitly expressed as follows:

Given n locations whose the plane coordinates are (x_i, y_i) and the values are z_i, where $i = 1, 2, \dots, n$, the interpolation function is

$$f(x,y) = \begin{cases} \dfrac{\sum_{i=1}^{n} \left(d_i / \text{dist}_i^p\right)}{\sum_{i=1}^{n} \left(1/\text{dist}_i^p\right)} & \text{if } (x,y) \neq (x_i, y_i), \quad i = 1, 2, \dots, n, \\ d_i & \text{if } (x,y) = (x_i, y_i), \quad i = 1, 2, \dots, n, \end{cases} \tag{1}$$

where $\text{dist}_i = \sqrt{(x - x_i)^2 + (y - y_i)^2}$ is the horizontal distance between (x, y) and (x_i, y_i), where $i = 1, 2, \dots, n$. p is a constant greater than 0, called the weighted power exponent.

It can easily be seen that the interpolation $f(x, y) = \sum_{i=1}^{n} (d_i/\text{dist}_i^p)/\sum_{i=1}^{n} (1/\text{dist}_i^p)$ of the location (x, y) is the weighted mean of $\text{dist}_1, \text{dist}_2, \dots, \text{dist}_n$.

The application of inverse-distance-weighted interpolation is more extensive. Because of its simple computation and having less constraints, the interpolation precision is higher. In [10], Kang and Wang use the Shepard family of interpolants to interpolate the density value of any given computational point within a certain circular influence domain of the point. In [11], Hammoudeh et al. use a

Shepard interpolation method to build a continuous map for a new WSN service called the map generation service.

From (1), we can see that the IDWI algorithm is sensitive to the accuracy of the data. However, WSN is usually deployed in a harsh environment, and the probability of data being collected is high. The error tolerance of the interpolation algorithm is required. This paper improves the robustness of interpolation algorithm on the basis of the inverse-distance interpolation algorithm.

2.2. Artificial Neural Network. An artificial neural network (ANN) is an information processing paradigm that is inspired from biological nervous systems, such as how the brain processes information. ANNs, like people, have the ability to learn by example. An ANN is configured for a specific application, such as pattern recognition, function approximation, or data classification, through a learning process. Learning in biological systems involves adjustments to the synoptic connections that exist among neurons. This is true for ANNs as well. They are made up of simple processing units which are linked by weighted connections to form structures that are able to learn relationships between sets of variables. This heuristic method can be useful for nonlinear processes that have unknown functional forms. The feed forward neural networks or the multilayer perceptron (MLP) among different networks is most commonly used in engineering. MLP networks are normally arranged in three layers of neurons; the input layer and output layer represent the input and output variables, respectively, of the model; laid between them is one or more hidden layers that hold the network's ability to learn nonlinear relationships [12].

The natural redundancy of neural networks and the form of the activation function (usually a sigmoid) of neuron responses make them somewhat fault tolerant, particularly with respect to perturbation patterns. Most of the published work on this topic demonstrated this robustness by injecting limited (Gaussian) noise on a software model [13]. Velazco et al. proved the robustness of ANN with respect to bit errors in [13]. Venkitaraman et al. proved that neural network architecture exhibits robustness to the input perturbation: the output feature of the neural network exhibits the Lipschitz continuity in terms of the input perturbation in [14]. Artificial neural networks have strong robustness. The robustness of the algorithm is a requirement to ensure the accuracy of artificial neural network operator transferring. We can see from the literatures [7, 8] that operator transferring can combine well with an artificial neural network. The learning operator in this paper also adopts an artificial neural network algorithm.

3. Problem Formulations

3.1. Data Acquisition Nodes. To assess the entire environmental condition, WSN collects data by deploying a certain number of sensors in the location of the monitoring area; thus, the physical quantity of the monitoring area is discretized and the monitoring physical quantity is digitized.

Definition 1. Interested locations: in the whole monitoring area, they are the central locations of the segment of the monitoring area that we are interested in.

Sensors can be deployed at each interested location to capture data. The data at all interested locations reflects the information status of the entire monitoring area.

We assumed that S is the set of the interested locations, which is a matrix of $1 \times n$.

$$S = \{s_1(x_1, y_1), s_2(x_2, y_2), s_3(x_3, y_3), \dots, s_n(x_n, y_n)\}, \quad (2)$$

where $s_i(x_i, y_i)$ is the ith interested location in the monitoring area. (x_i, y_i) is the coordinates of the s_i interested location in the monitoring area. Due to the difficulty and limitation of deployment, not all the interested locations can deploy sensors. This paper studies the spatial incomplete collection strategy. We select a subset of S as the data acquisition node. $\|S\|$ represents the potential of a set, that is, the number of elements of S. $\|S\| = n$.

Definition 2. Data acquisition nodes: they are the interested locations where the sensors are actually deployed.

The sensors are deployed in these interested locations, so that these locations become data acquisition nodes. The all-data acquisition nodes in the monitoring area act as the sensing layer of the WSN, and the information is transmitted to the server through the devices of the transport layer.

In our research, when the sensors are not deployed at the interested location, we use zero as a placeholder to replace the data acquisition node. When the interested location becomes the data acquisition node, we use 1 as a placeholder to replace the data acquisition node. Suppose that M is the set of data acquisition nodes.

$$M = \{s_i \mid s_i = 1, s_i \in S, i = 1 \dots n\}, \quad (3)$$

where $s_i = 1$ represents the ith interested location where the sensors are deployed. $\|M\|$ indicates the potential of the set M. It reflects the total number of elements in the set of data acquisition nodes. This paper investigates the case where multiple types of sensors are deployed at a data acquisition node. The data that the data acquisition node s_i can correctly collect at time t_l is defined as $\mathrm{d}_{s_i}(t_l) = [\mathrm{d}_{s_i,1}(t_l), \mathrm{d}_{s_i,2}(t_l), \dots, \mathrm{d}_{s_i,k}(t_l)]$, which is k dimensional data that is perceived by the ith data acquisition location s_i in S. The physical quantity of temperature, humidity, etc. can be measured at the same time. The data is defined as

$$D_M(t_l) = \left\{\mathrm{d}_{s_i}(t_l) \mid s_i \in \mathrm{M}, \mathrm{d}_{s_i}(t_l) \in \mathrm{R}^k\right\}. \quad (4)$$

If $\|M\| < \|S\|$, then WSN implements incomplete coverage; if $\|M\| = \|S\|$, then WSN implements complete coverage. The data of the interested location where the sensors are not deployed can be assessed by the data of the data acquisition node. The interested location where the sensors are not deployed is indicated as non-data acquisition location.

3.2. Data Acquisition Error. Because the wireless communication network is susceptible to interference, attenuation, multipath, blind zone, and other unfavorable factors, the data error rate is high. Nodes and links in wireless sensor networks are inherently erroneous and unpredictable. The error data which greatly deviated from the ideal truth value is divided into two types: data loss and data disturbance.

(1) Data Loss. These reasons, such as nodes cannot work, links cannot be linked, or data cannot be transmitted, cause the data of the corresponding data acquisition nodes to not reach the sink node.

(2) Data Disturbance. Due to the failure, the local function of the WSN is in an incorrect (or ambiguous) system state. This state may cause a deviation between the data measured by the sensors of the corresponding data acquisition node and the true value, or the signal is disturbed during the transmission, and the data received at the sink node is deviant from the true value. The data that corresponds to the data acquisition node is not the desired result. The collected data oscillate in the data area near the true value. In this paper, we assumed that the data disturbance obeys the Gauss distribution.

The main idea of our method is based on the fundamental assumption that the sensing data of WSN are regarded as a vector indexed by the interested locations and recovered from a subset sensing data. As demonstrated in Figure 1, the data acquisition consists of two stages: the data-sensing stage and the data-recovering stage. At the data-sensing stage, instead of deploying sensors and sensing data at all interested locations, a subset of interested locations which are the shaded ones in the second subfigure is selected to sense physical quantity and deliver the sensing data to the sink node at each data collection round. Some locations are drawn by the fork in the second subfigure because their data is lost or disturbed. The fork represented the data errors. When the hardware and software of the network node failures or the communication links of the network are broken, the set of sensors which encounter data errors is only the subset of M. At the data-recovering stage, the sink node receives these incomplete sensing data over some data collection rounds shown in the third subfigure in which the shaded entries represent the valid sensing data and the white entries are unknown. And then we could use them to recover the complete data by our method.

Here we adopt a mask operator $A()$ to represent the process of collecting data-encountering errors:

$$A(D_M(t_l)) = B(t_l), \tag{5}$$

where B is the data set that is actually received for interpolation. For the sake of clarity, the operator $A()$ can be specified as a vector product as follows:

$$A(D_M(t_l)) = Q \odot D_M(t_l), \tag{6}$$

where $\odot$ denotes the product of two vectors, i.e., $b_{s_i}(t_l) = d_{s_i}(t_l) \times q_{s_i}$. Q is a vector of $1 \times \|M\|$. b_{s_i} indicates the data that is actually received by the ith data acquisition node for interpolation.

$$q_{s_i} = \begin{cases} 1, & \text{if the data is not error,} \\ \begin{cases} 0, & \text{if the data is lost,} \\ \dfrac{\mathrm{No}\left(d_{s_i}(t_l), \sigma^2\right)}{d_{s_i}}, & \text{if the data is disturbed,} \end{cases} \end{cases} \tag{7}$$

where $\mathrm{No}(d_{s_i}(t_l), \sigma^2)$ represents Gauss distribution with a mean of $d_{s_i}(t_l)$ and a variance of σ^2.

In this paper, the error rate of the received data is defined as follows: $\|Q\|_{q_{s_i} \neq 1} / \|M\|$, where $\|Q\|_{q_{s_i} \neq 1}$ is the number of non-1 elements.

3.3. Completion of Data Space with Interpolation. Due to conditional restrictions, there is no way to deploy sensors in $S - M$. The data generated in $S - M$ can be estimated by interpolation based on the data in M. The data space of the entire monitoring area is set to

$$D_S(t_l) = D_M(t_l) \cup \widehat{D}_{S-M}(t_l), \tag{8}$$

where $D_M(t_l)$ represents the data set collected from the data acquisition node in M at epoch t_l. $D_{S-M}(t_l)$ is the data set collected from non-data acquisition locations $S - M$ at the epoch t_l in the ideal case, if the sensors are deployed in the non-data acquisition location. $\widehat{D}_{S-M}(t_l)$ is the data interpolation set based on the data in M.

The problem definition is how to process the $D_M(t_l)$ data so that $\widehat{D}_{S-M}(t_l)$ is as close as possible to $D_{S-M}(t_l)$, that is, the problem of minimizing the error between $\widehat{D}_{S-M}(t_l)$ and $D_{S-M}(t_l)$. Its mathematical expression is as follows:

$$\begin{aligned} \arg\min \quad & \left\| \widehat{D}_{S-M}(t_l) - D_{S-M}(t_l) \right\| \\ \text{s.t.} \quad & Q \neq 1, \end{aligned} \tag{9}$$

where $\|\cdot\|$ is the Euclidean norm form used to evaluate the error between $\widehat{D}_{S-M}(t_l)$ and $D_{S-M}(t_l)$; $Q \neq 1$ indicates that Q is not a full 1 matrix.

$$\begin{aligned} \widehat{D}_{S-M}(t_l) = \Big\{ & \widehat{d}_{s_j}(t_l) \mid \widehat{d}_{s_j}(t_l) \\ & = E\left(\widehat{d}'_{s_j}(t_l), \widehat{d}''_{s_j}(t_l), \ldots, \widehat{d}^n_{s_j}(t_l)\right), s_j \in S - M \Big\}, \end{aligned} \tag{10}$$

where $d'_{s_j}(t_l), d''_{s_j}(t_l), \ldots, d^n_{s_j}(t_l)$ represents each value close to $d_{s_j}(t_l)$. Suppose s_i is the closest data acquisition node to s_j. The value received from the data acquisition node nearest the non-data acquisition location is also close to $d_{s_j}(t_l)$.

$$\because \mathrm{dist}_{s_i \longrightarrow s_j} = \min\left(\mathrm{dist}_{M \longrightarrow s_j}\right), \quad s_i \in M, \tag{11}$$

where $\mathrm{dist}_{M \longrightarrow s_j}$ indicates the distance from each data acquisition node in M to the non-data acquisition location s_j. The

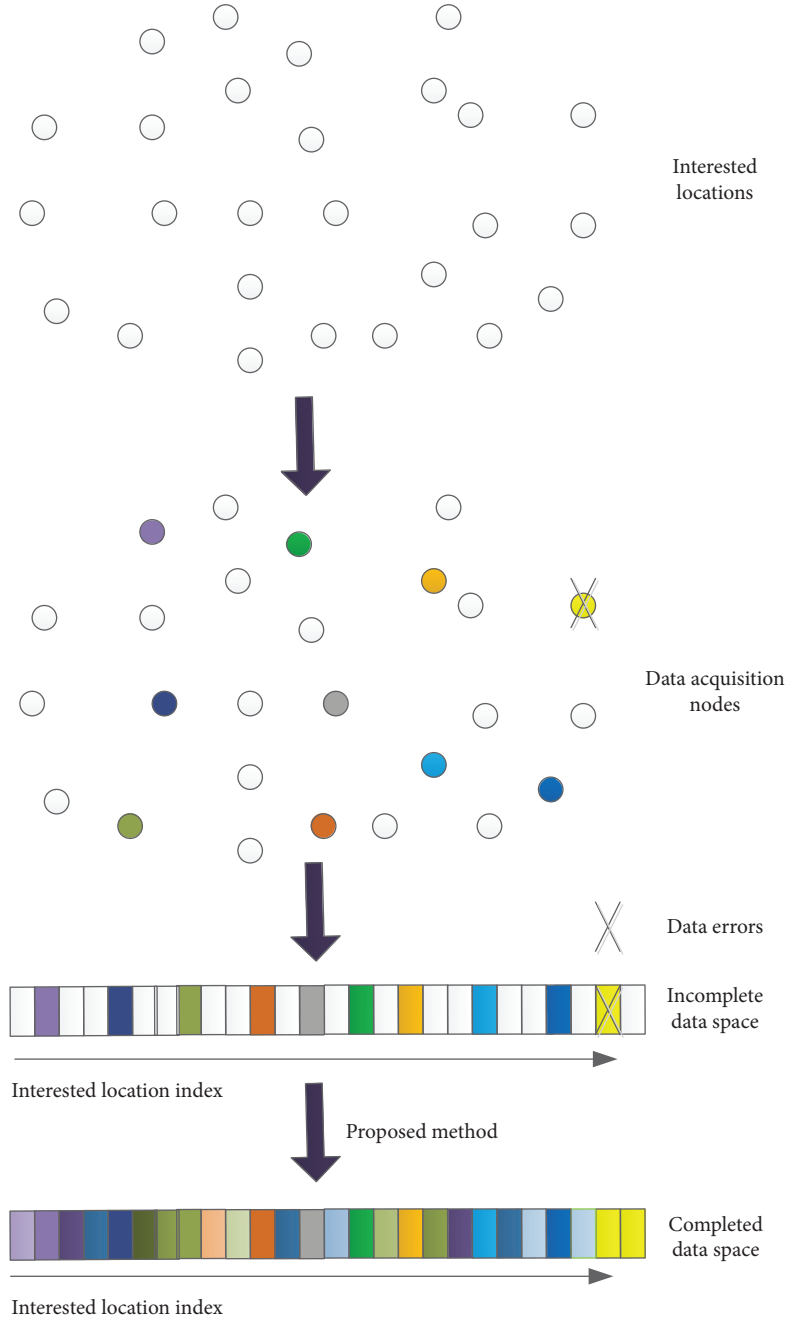

Figure 1: Incomplete acquisition process based on our proposed method.

closer the information collected by the node, the greater the correlation [15].

$$\therefore d'_{s_j}(t_l) = d_{s_i}(t_l), \tag{12}$$

where $d_{s_i}(t_l)$ represents the value of the physical quantity actually collected by the s_i data acquisition node.

Suppose that $\widehat{d}''_{s_j}(t_l)$ represents the assessed value at the jth non-data acquisition location, which is obtained by the back propagation artificial neural network operator. In this paper, we get the $\widehat{d}''_{s_j}(t_l)$ that is close to $d_{s_j}(t_l)$.The data set of non-data acquisition locations for interpolation is

$$\begin{aligned} d''_{s_j}(t_l) &= \Upsilon_{s_j}\left(\mathrm{b}_{s_i}(t_l)\right), \quad s_j \in S - M, s_i \in M, \\ \widehat{D}''_{S-M}(t_l) &= \Upsilon_{S-M}(B(t_l)), \end{aligned} \tag{13}$$

where $\Upsilon_{S-M}(\cdot)$ represents the learning operator to assess $d_{s_j}(t_l)$. $B(t_l)$ represents the received data set at the epoch t_l. We can use the back propagation artificial neural network operator of the data acquisition node closest to the non-

data acquisition location to predict the data of the non-data acquisition location.

4. Learning Operator Set of Data Acquisition Nodes

The mathematical model of the learning operator for the reconstruction is as follows:

$$\begin{aligned} \arg\min \quad & \|\Upsilon(\mathrm{Inp}) - \mathrm{Tar}\| \\ \text{s.t.} \quad & \mathrm{Inp} \neq \mathrm{Tar}. \end{aligned} \tag{14}$$

where Tar represents the learning goals, $\Upsilon(\cdot)$ is the learning operator of Inp, and Inp can be individuals, variables, and even algorithms or functions, sets, and so on. The input of $\Upsilon(\cdot)$ is Inp. Inp and Tar are different. If they do not have differences, there is no need to learn for reconstruction. The purpose of learning is to make $\Upsilon(\mathrm{Inp})$ gradually approach Tar.

Because data of WSN is error-prone, we need fault-tolerant and robust learning operators. The learning operator in this paper uses a back propagation (BP) artificial neural network. We can use data of data acquisition nodes to predict the data of the non-data acquisition location, thus assessing the data space of the entire monitoring area. Because of the strong robustness and adaptability of the artificial neural network, we can use the artificial neural network to interpolate the data of non-data acquisition locations in the case of data error.

The BP artificial neural network is a multilayer (at least 3 levels) feedforward network based on error backpropagation. Because of its characteristics, such as nonlinear mapping, multiple input and multiple output, and self-organizing self-learning, the BP artificial neural network can be more suitable for dealing with the complex problems of nonlinear multiple input and multiple output. The BP artificial neural network model is composed of an input layer, hidden layer (which can be multilayer, but at least one level), and output layer. Each layer is composed of a number of juxtaposed neurons. The neurons in the same layer are not connected to each other, and the neurons in the adjacent layers are connected by means of full interconnection [16].

After constructing the topology of the artificial neural network, it is necessary to learn and train the network in order to make the network intelligent. For the BP artificial neural network, the learning process is accomplished by forward propagation and reverse correction propagation. As each data acquisition node is related to other data acquisition nodes, and each data acquisition node has historical data, it can be trained through the historical data of data acquisition nodes to generate the artificial neural network learning operator of the data acquisition node.

4.1. Transform Function of the Input Unit. The data of the non-data acquisition location s_j is assessed by using the inverse-distance learning operator of the data acquisition node s_i closest to s_j. Because there is spatial correlation between interested locations in space acquisition, in this paper, we adopt the IDWI algorithm combined with the BP artificial neural network algorithm.

At a certain epoch t_l, the data set of all other data acquisition nodes except the s_i is as follows:

$$B_{M-s_i}(t_l) = \begin{bmatrix} b_{s_o,1}(t_l) & \cdots & b_{s_o,1}(t_l) \\ \vdots & b_{s_q,i}(t_l) & \vdots \\ b_{s_m,k}(t_l) & \cdots & b_{s_m,k}(t_l) \end{bmatrix}, \quad b_{s\cdot} \in M - s_i. \tag{15}$$

In this paper, the inverse-distance weight is used to construct the transform function. The transform function $h_{s_i}(B_{M-s_i}(t_l))$ of the input unit $B_{M-s_i}(t_l)$ of the artificial neural network with data acquisition node s_i is as follows:

$$h_{s_i}\left(B_{M-s_i}(t_l)\right) = \frac{\left(1/\mathrm{dist}^{\gamma}_{s_q \longrightarrow s_i}\right) \times B_{M-s_i}(t_l)}{\sum_{s_q \in M}^{\|M\|-1}\left(1/\mathrm{dist}^{\gamma}_{s_q \longrightarrow s_i}\right)}, \quad s_q \in M - s_i, s_i \in M, \tag{16}$$

where $\mathrm{dist}_{s_q \longrightarrow s_i}$ represents the distance between the data acquisition node s_i and the non-data acquisition location s_q. γ represents the weighted power exponent of the distance reciprocal. $\sum_{s_q \in M}^{\|M\|-1}(1/\mathrm{dist}^{\gamma}_{s_q \longrightarrow s_i})$ represents the sum of the weighted reciprocal of the distance from the data acquisition node s_i to the rest of data acquisition nodes.

The artificial neural network requires a training set. We take the historical data of the period T of all data acquisition nodes as the training set. $T = [t_0, t_1, \cdots, t_l, \cdots, t_m]$. In practical engineering, it is feasible for us to get the data from data acquisition nodes in a period to learn.

In this paper, data collected from all data acquisition nodes are used as the training set $B_{M-s_i}(T)$. $B_{M-s_i}(T)$ is a three-order tensor, as shown in the following Figure 2. $B_{M-s_i}(T) \in R^{k \times \|M-s_i\| \times t_m}$. The elements of the training set are indexed by physical quantities, acquisition node, and epoch.

The $B_{M-s_i}(T)$ matrix is obtained by

$$B_{M-s_i}(T) = \left[\begin{vmatrix} b_{s_o,1}(t_0) & \cdots & b_{s_o,1}(t_0) \\ \vdots & b_{s_q,i}(t_l) & \vdots \\ b_{s_m,k}(t_0) & \cdots & b_{s_m,k}(t_0) \end{vmatrix} \begin{vmatrix} b_{s_o,1}(t_1) & \cdots & b_{s_o,1}(t_1) \\ \vdots & b_{s_q,i}(t_1) & \vdots \\ b_{s_m,k}(t_1) & \cdots & b_{s_m,k}(t_1) \end{vmatrix} \cdots \begin{vmatrix} b_{s_o,1}(t_l) & \cdots & b_{s_o,1}(t_l) \\ \vdots & b_{s_q,i}(t_l) & \vdots \\ b_{s_m,k}(t_l) & \cdots & b_{s_m,k}(t_l) \end{vmatrix} \cdots \begin{vmatrix} b_{s_o,1}(t_m) & \cdots & b_{s_o,1}(t_m) \\ \vdots & b_{s_q,i}(t_l) & \vdots \\ b_{s_m,k}(t_m) & \cdots & b_{s_m,k}(t_m) \end{vmatrix} \right], \quad b_{s\cdot} \in M - s_i. \tag{17}$$

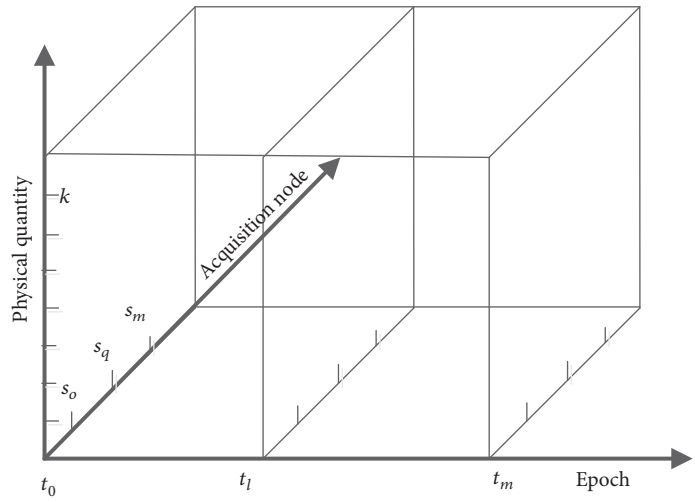

Figure 2: The model of $B_{M-s_i}(T)$.

In actual engineering, $B_{M-s_i}(T)$ has a lot of noise. It is necessary to clean it. If it is not cleaned, it will affect the estimation accuracy of the artificial neural network and the precision of learning. Data cleaning is the process of reexamining and verifying data to remove duplicate information, correct existing errors, and provide data consistency. We can use various filter algorithms to get $\bar{B}_{M-s_i}(T)$.

4.2. Artificial Neural Network Learning Operator. The sensing data of the real network include several physical quantities, such as temperature, humidity, and illumination. Usually, a variety of sensors are deployed at an acquisition node, and multiple physical quantities are collected at the same time. Physical quantities at the same acquisition node have the same temporal and spatial variation trend, but in the process of recovery using the artificial neural network, each quantity has a mutual promotion effect. The distance between data acquisition nodes and non-data acquisition locations is very easy to obtain. Based on the inverse-distance interpolation algorithm and BP artificial neural network algorithm, we propose a multidimensional inverse-distance BP artificial neural network learning operator.

The BP artificial neural network, which is the most widely used one-way propagating multilayer feedforward network, is characterized by continuous adjustment of the network connection weight, so that any nonlinear function can be approximated with arbitrary accuracy. The BP artificial neural network is self-learning and adaptive and has robustness and generalization. The training of the BP artificial neural network is the study of "supervisor supervision," The training process of the BP artificial neural network is shown in Figure 3.

For the input information, it is first transmitted to the node of the hidden layer through the weighted threshold summation, and then the output information of the hidden node is transmitted to the output node through the weighted threshold summation after the operation of the transfer function of each element. Finally, the output result is given. The purpose of network learning is to obtain the right weights and thresholds. The training process consists of two parts: forward and backward propagation.

The BP artificial neural network is a multilayer feedforward network trained by the error backpropagation algorithm. The BP artificial neural network structure is a multilayer network structure, which has not only input nodes and output nodes but also one or more hidden nodes. As demonstrated in Figure 3, according to the prediction error, the v and w are continuously adjusted, and finally the BP artificial neural network learning operator for reconstructing the data of data acquisition node s_i can be determined, as shown in the part $\Upsilon_{s_i}(\cdot)$ of Figure 3.

The input layer of the BP artificial neural network learning operator is the data collected at a certain time at all acquisition nodes except the s_i acquisition node, which is the vector $h_{s_i}(\bar{B}_{M-s_i}(t_l))$. The input of the jth neuron in the hidden layer is calculated by

$$\Sigma_j = \sum_{q=1}^{\|M\|-1} \sum_{p=1}^{k} v_{q,j,p} h_{s_i}\left(\bar{B}_{M-s_i}(t_l)\right) - \theta_j, \tag{18}$$

where $v_{q,j,p}$ represents the weight between the (q,p)th input neurons and the jth neurons in the hidden layer. The (q,p)th input neurons are $h_{s_i}(b_{s_q,k}(t_l))$, that is, the k-th dimension data of the s_q acquisition node at time t_l. θ_j is the threshold of the jth neuron in the hidden layer. The output of neurons in the hidden layer is calculated by

$$\mathrm{ho}_j = \frac{1}{1+e^{-\Sigma_j}}. \tag{19}$$

Similarly, the output of each neuron in the output layer is set to o_p.

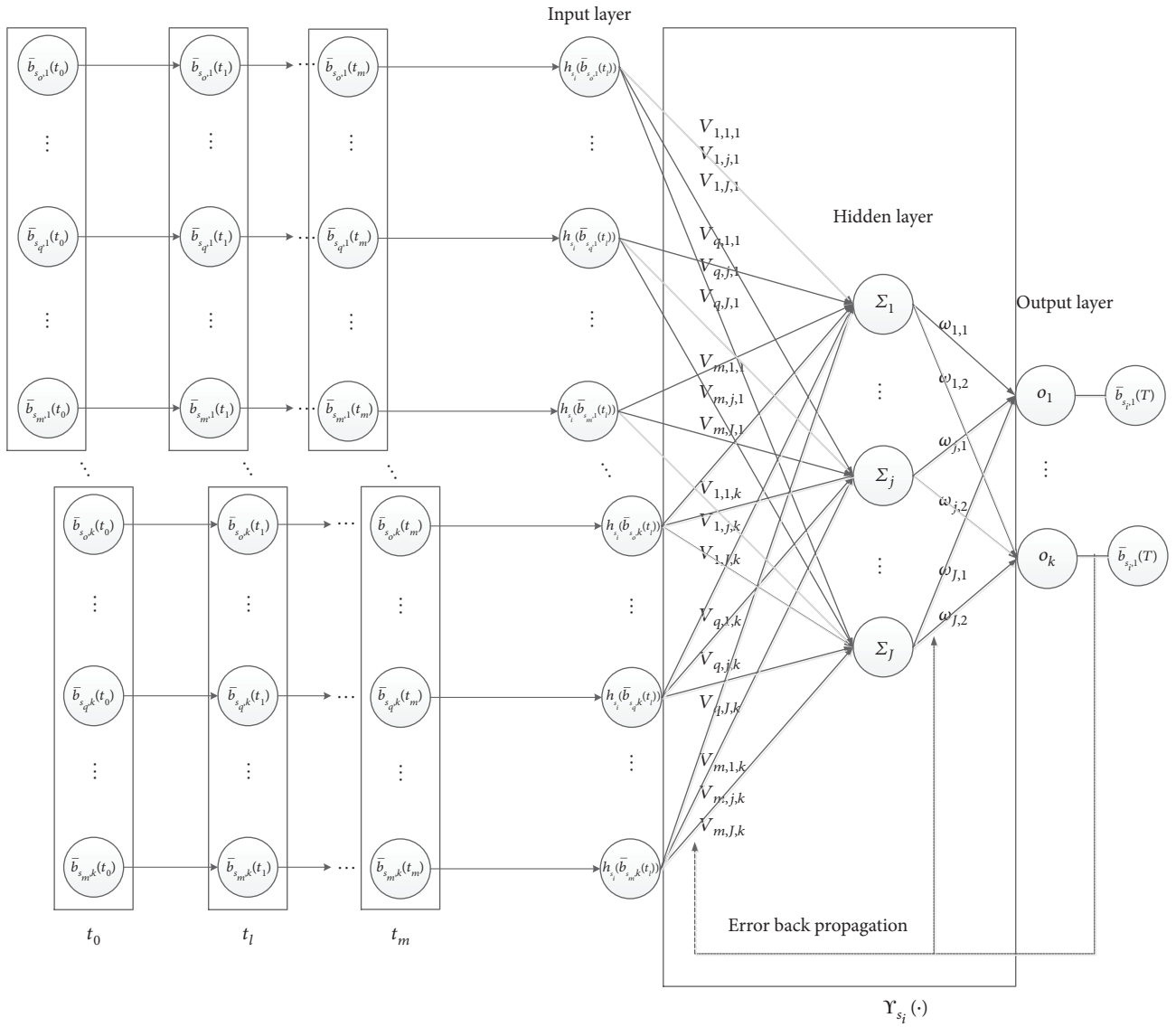

Figure 3: The training process of the BP artificial neural network.

The sum of squared errors of all neurons in the output layer is the objective function value optimized by the BP artificial neural network algorithm, which is calculated by

$$E = \frac{1}{(\|M\| - 1) \times k \times k} \sum_{q=1}^{\|M\|-1} \sum_{p=1}^{k} \sum_{p=1}^{k} \left(\bar{b}_{s_i,p} - o_p\right)^2, \tag{20}$$

where $\bar{b}_{s_i,p}$ represents the expected output value of neuron o_p in the output layer, corresponding to the value of the pth physical quantity sensed by the data acquisition node s_i. According to the gradient descent method, the error of each neuron in the output layer is obtained by

$$E_p = o_p \times \left(1 - o_p\right) \times \left(\bar{b}_{s_i,p} - o_p\right). \tag{21}$$

The weights and thresholds of the output layer can be adjusted by

$$\Delta\omega = \partial \times E_p \times ho_j, \tag{22}$$

$$\Delta\theta_p = \partial \times E_p, \tag{23}$$

where $\partial \in [0, 1]$ is the learning rate, which reflects the speed of training and learning. Similarly, the weight and threshold of the hidden layer can be obtained. If the desired results cannot be obtained from the output layer, it needs to constantly adjust the weights and thresholds, gradually reducing the error. The BP neural network has strong self-learning ability and can quickly obtain the optimal solution.

The mathematical model of Figure 3 is as follows:

$$f_{o_p}\left(\sum_{j=1}^{J}\sum_{p=1}^{k}\omega_j f_{\Sigma_j}\left(\sum_{q=1}^{\|M\|-1}\sum_{p=1}^{k}\nu_{q,j,p}h_{s_i}\left(\bar{B}_{M-s_i}(T)\right)\right)\right)\longrightarrow \bar{b}_{s_i,p}(T), \tag{24}$$

where $\bar{B}_{s_q}(T)$ is the training data, that is, the historical data of acquisition nodes except s_i in the period T. $h_{s_i}(\cdot)$ is the transform function of the input layer. $\nu_{q,j}$ is the weight of the input layer. $f_{\Sigma_j}(\cdot)$ is the transfer function of the input layer to the hidden layer. w is the weight of the hidden layer to the output layer. $f_{o_p}(\cdot)$ is the transfer function of the hidden layer to the input layer. $\bar{b}_{s_i}(T)$ is the "supervisor supervision" that is the historical data of acquisition node s_i in the period T.

From (14) and (24), the following formula can be obtained:

$$\Upsilon_{s_i}(\cdot)=f_{o_p}\left(\sum_{j=1}^{J}\omega_j f_{\Sigma_j}\left(\sum_{q=1}^{\|M\|-1}\sum_{p=1}^{k}\nu_{q,j,p}(\cdot)\right)\right)|\bar{b}_{s_i}(T), \tag{25}$$

where $\Upsilon_{s_i}(\cdot)$ represents the inverse-distance BP artificial neural network learning operator of acquisition node s_i. $|\bar{b}_{s_i}(T)$ represents that this neural network operator $\Upsilon_{s_i}(\cdot)$ is a learning operator trained by the data of s_i as tutor information.

The data collected by each data acquisition node in the monitoring area is related to each other. The data of a data acquisition node can be learned by inputting the data of other data acquisition nodes into the learning operator. The learning operator set of data acquisition nodes in the whole monitoring area is as follows:

$$\Upsilon(\cdot)=\left\{\Upsilon_{s_i}(\cdot)\mid s_i\in M\right\}. \tag{26}$$

5. Interpolation at Non-Data Acquisition Locations

We transfer the BP artificial neural network operators from data acquisition nodes to non-data acquisition locations. We can use the learning operator of the data acquisition node closest to the non-data acquisition location to estimate the data of the non-data acquisition location. There are four ways to implement the learning operator transferring, including sample transferring, feature transferring, model transferring, and relationship transferring. In this paper, model transferring (also called parameter transferring) is used to better combine with the BP artificial neural network; that is, we can use the pretrained BP artificial neural network to interpolate. The BP artificial neural network learning operator has strong robustness and adaptability. In the interested area, if the physical quantity collected is highly correlated, and there is no situation in which the physical quantity changes drastically between the various interested locations, the learning operator can be transferred.

Since the construction of the artificial neural network requires historical data for training, and there is no historical data at the non-data acquisition location deployed without sensors, it is very difficult to construct the artificial neural networks of the non-data acquisition location. However, we can predict the physical quantities of non-data acquisition locations by using the learning operator from the nearest data acquisition node.

5.1. Transform Function Corresponding to Nonacquisition Location s_j. First, we use the IDWI method to construct the transform function. The transform function of the artificial neural network input unit s_q of the acquisition node s_i is defined as $h_{s_i}(B_{M-s_i}(t_l))$:

$$h_{s_j}\left(B_{M-s_i}(t_l)\right)=\frac{B_{M-s_i}(t_l)/\mathrm{dist}_{s_q\longrightarrow s_j}^{\gamma}}{\sum_{s_q\in M-s_i}^{\|M\|-1}\left(1/\mathrm{dist}_{s_q\longrightarrow s_j}^{\gamma}\right)}, \tag{27}$$

where $\mathrm{dist}_{s_q\longrightarrow s_j}$ represents the distance between s_q and s_j. γ represents the weighted exponentiation of the distance reciprocal. $\sum_{s_q\in M}^{\|M\|-1}(1/\mathrm{dist}_{s_q\longrightarrow s_j}^{\gamma})$ represents the sum of the weighted reciprocal of the distance from the non-data acquisition location s_j to the rest of the acquisition nodes. The physical data collected from the remaining $\|M\|-1$ data acquisition nodes except s_i are as follows:

$$B_{M-s_i}=\left\{b_{s_q}(t_l)\mid s_q\in M-s_i\right\}. \tag{28}$$

5.2. Learning Operator Transferring. Since the data of the data acquisition node closest to the non-data acquisition location is important to the non-data acquisition location, and its data is most correlated with the data of the non-data acquisition location, we estimate the data of the non-data acquisition location with data from the nearest data acquisition node and its learning operator.

Since the data we are targeting is spatially correlated, the smaller the distance between the two interested locations is, the smaller the difference of the collected data is. Conversely, the greater the difference of the collected data is. We can use the data of the data acquisition node close to the non-data acquisition location to assess the data at the non-data acquisition location.

Because the BP artificial neural network learning operator has strong robustness and adaptability, we can transfer the inverse BP artificial neural network learning operator of s_i to s_j in order to estimate the data at s_j in this paper. The transform function $h(\cdot)$ does not change with time, and it is a function of the distance between the sampling locations. $h_{s_i}(B_{M-s_i}(t_l))\longrightarrow h_{s_j}(B_{M-s_i}(t_l))$, the number of input parameters is constant, while the input parameters vary with time. So the change of the transform function will not affect the

trend of input parameters. The change of the transform function will not affect the accuracy of prediction, and the operator transferring can be implemented.

$$\begin{aligned}\widehat{d}''_{s_j}(t_l) &= \Upsilon_{s_i}\left(h_{s_j}\left(B_{M-s_i}(t_l)\right)\right)\\ &= f_{s_i}\left(\sum_{j=1}^{J}\omega_j f_{z_j}\left(\sum_{q=1}^{\|M\|}\nu_{q,j}h_{s_j}\left(B_{M-s_i}(t_l)\right)\right)\right).\end{aligned} \tag{29}$$

The assessment network based on the BP artificial neural network operator is shown in Figure 4.

In this paper, our proposed method is improved on the basis of the BP artificial neural network. According to spatial correlation, the physical quantities of the monitored and interested location close to the data acquisition nodes s_q can be approximated by learning the operator of s_q.

Suppose d_{s_j} represents the estimated value of the physical quantity of the interested location s_j. Due to conditional restrictions, no sensor is deployed at the interested location s_j. We choose the physical quantity of the data acquisition node s_i nearest to the non-data acquisition location s_j for estimation. We can use Algorithm 1 to achieve the determination of s_i.

5.3. Assessment at the Non-Data Acquisition Location. s_i is the nearest data acquisition node to s_j. We can use the learning operator of the data acquisition node s_i to estimate d_{s_j}. This paper is an improvement on the inverse-distance interpolation method. Because s_i is closest to s_j, the correlation of their data is the largest. The data collected actually by s_i have the greatest impact on the predictive value at s_j.

$$\begin{aligned}d_{s_j} &= E\left(\widehat{d'}_{s_j}(t_l), \widehat{d''}_{s_j}(t_l)\right)\\ &= \alpha\times\widehat{d'}_{s_j}(t_l) + \beta\times\widehat{d''}_{s_j}(t_l), \quad s_i\in M, s_j\in S-M,\end{aligned} \tag{30}$$

where α and β denote the weight of $\widehat{d'}_{s_j}(t_l)$ and $\widehat{d''}_{s_j}(t_l)$, respectively, to estimate physical quantities at s_j. $\alpha+\beta=1$.

$\widehat{d'}_{s_j}(t_l)$ is the value of the actual measurement, so its credibility is higher. The closer s_i is to s_j, the greater the correlation between physical quantity at s_i and the data collected by s_i based on spatial correlation.

We assume that $\mathrm{dist}_{s_i\longrightarrow s_j}$ represents the distance between s_i and s_j. The influence weight of data collected by s_i on the assessment of s_j decreases with increasing $\mathrm{dist}_{s_i\longrightarrow s_j}$. Conversely, the greater the distance $\mathrm{dist}_{s_i\longrightarrow s_j}$, the smaller the impact. The change field of $\mathrm{dist}_{s_i\longrightarrow s_j}$ is $[0,+\infty)$. We find that the inverse tangent function is an increasing function on $[0,+\infty)$. The function curve is shown in Figure 5.

We use the boundedness and monotonically increasing characteristics of the arctangent function curve and are inspired by the idea of IDWI. The formula for calculating β is as follows:

$$\beta = \frac{\arctan\left(\mathrm{dist}_{s_i\longrightarrow s_j}\right)}{\pi/2}, \quad \mathrm{dist}_{s_i\longrightarrow s_j}\in[0,+\infty). \tag{31}$$

We limit the value of β to the interval [0, 1]. When $\mathrm{dist}_{s_i\longrightarrow s_j}$ is close to 0, β is close to 0, and $1-\beta$ is close to 1, then the data measured by the data acquisition point is closer to the value at the non-data acquisition location. When $\mathrm{dist}_{s_i\longrightarrow s_j}=0$, it means that the sensors have deployed in s_j, and we do not need other values calculated by the prediction algorithm and directly use the actual measured data.

$$\begin{aligned}\widehat{d}_{s_j} &= \frac{\arctan\left(\mathrm{dist}_{s_i\longrightarrow s_j}\right)}{\pi/2}\times\widehat{d''}_{s_j}(t_l)\\ &\quad+\left(1-\frac{\arctan\left(\mathrm{dist}_{s_i\longrightarrow s_j}\right)}{\pi/2}\right)\times\widehat{d'}_{s_j}(t_l), \quad s_i\in M, s_j\in S-M.\end{aligned} \tag{32}$$

If the interested location of the interpolation is still far from the nearest data acquisition node, then this algorithm will cause a large error. Since we are using the sensor placement based on the iterative dividing four subregions, the sensors of the data acquisition node are omnidirectional throughout the space, not only concentrated in a certain domain. The error is not too large.

6. Experiments and Evaluation

6.1. Parameter Setup. The data set we used is the measured data provided by the Intel Berkeley Research lab [9]. The data is collected from 54 data acquisition nodes in the Intel Berkeley Research lab between February 28th and April 5th, 2004. In this case, the epoch is a monotonically increasing sequence number from each mote. Two readings from the same epoch number were produced from different motes at the same time. There are some missing epochs in this data set. Mote IDs range from 1–54. In this experiment, we selected the data of these 9 motes as a set of interested locations, because these 9 points have the same epoch.

$$\begin{aligned}S=\{&s_7(22.5,8), s_{18}(5.5,10), s_{19}(3.5,13), s_{21}(4.5,18),\\ &s_{22}(1.5,23), s_{31}(15.5,28), s_{46}(34.5,16), s_{47}(39.5,14),\\ &s_{48}(35.5,10)\}.\end{aligned} \tag{33}$$

When the environment of the monitoring area is not very complicated, the physical quantity of acquisition is a very spatial correlation, and it is feasible to use the placement based on the iterative dividing four subregions to deploy sensors. In this experiment, we use the method of the iterative dividing four subregions to select the interested locations from S as data acquisition nodes. The closest $s_i(x_i,y_i)$ $(s_i(x_i,y_i)\in S)$ to the deployment location

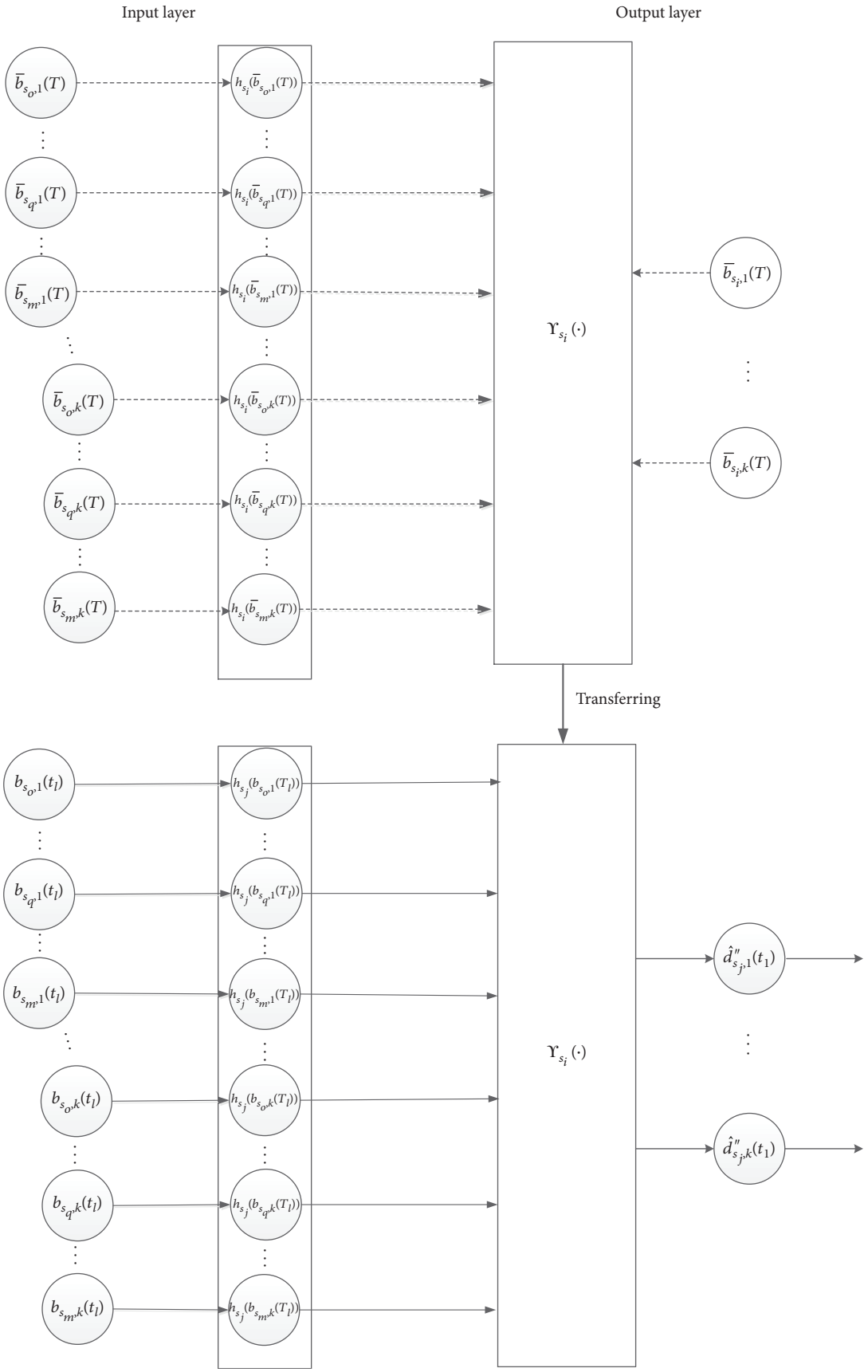

Figure 4: The assessment network based on the BP artificial neural network operator.

generated by the method of the iterative dividing four subregions is selected in M.

In this experiment, we set the dimension of the collected data to 2, that is, $k = 2$. We take two physical quantities: temperature and humidity. Data acquisition nodes need at least two, i.e., $\|M\| \geq 2$. Because one data acquisition node should be the closest node from the interested location for interpolation, and $s_i \notin \varnothing$, the data of other acquisition nodes should be used as the training set of the artificial neural network. $M - s_i \notin \varnothing$, $\|M - s_i\| \geq 1$.

The epochs we chose are: $T = \{33,35,42, 44,51,56,61,62, 70,73,86,88,89,91,95,99,102,107,112,113,123,124,127\}$. These data whose epoch is an element in T are used as a training set epoch. Unfortunately, the actual sampling sensing data are always corrupted and some values go missing. We need real clean sensing data to train the BP artificial neural networks to improve the interpolation precision.

In order to not lose the trend of data change in the process of data filtering, we simply use the mean processing with a filter window on the temporal direction of the measurements as the clean sensing data. If $|d_{s_i}(t-1) - d_{s_i}(t)| \gg \delta \times |\bar{d}_{M-s_i}(t-1) - \bar{d}_{M-s_i}(t)|$, then $d_{s_i}(t)$ can be replaced by the value calculated

$$d_{s_i}(t) = \frac{d_{s_i}(t-1) + d_{s_i}(t+1)}{2}, \tag{34}$$

where δ is the adjusting coefficient. In this experiment, we take $\delta = 10$.

The filtered result of the temperature measurements is shown in Figure 6(a), and the actual sensing data is shown in Figure 6(b). The filtered result of the humidity measurements is shown in Figure 7(a), and the actual sensing data is shown in Figure 7(b).

When comparing the test results, we need that the epoch of the data supplied by each mote is the same. Because in the actual application, the data space of the monitoring area we built is the data space at a certain moment. We assumed that $t_l = 138$. In this experiment, the time we selected was the 138th epoch for interpolation. We compare the actual collected value at the 138th epoch with the interpolation calculated by algorithms.

To evaluate the accuracy of the reconstructed measurement, we choose the mean relative error (MRE). It reflects the precision of the estimated data relative to the measured data. The formula for the calculation of MRE is as follows [17]:

$$\text{MRE} = \frac{1}{n}\sum_{i=1}^{n}\left|\frac{d(x_i) - \widehat{d}(x_i)}{d(x_i)}\right|, \tag{35}$$

where $d(x_i)$ is the actual acquisition value of the ith sensor. Correspondingly, $\widehat{d}(x_i)$ is the assessed value. n is the total number of data acquisition nodes.

6.2. Results of the Experiment. This experiment is in a small range, the physical quantity of the collected data is highly correlated, and there is no situation in which the physical quantity changes drastically between the various interested locations, so the learning operator can be transferred.

Input: M, $s_j(x_j, y_j)$
Output: s_i
Initialize mindist
For each s_i in M
  $\text{dist}_{s_j \longrightarrow s_q} = \sqrt[2]{(x_j - x_q)^2 + (y_j - y_q)^2}$
  if mindist > $\text{dist}_{s_j \longrightarrow s_q}$
    then $i = q$, mindist = $\text{dist}_{s_j \longrightarrow s_q}$
  end if
End for

Algorithm 1: Culling s_i from M.

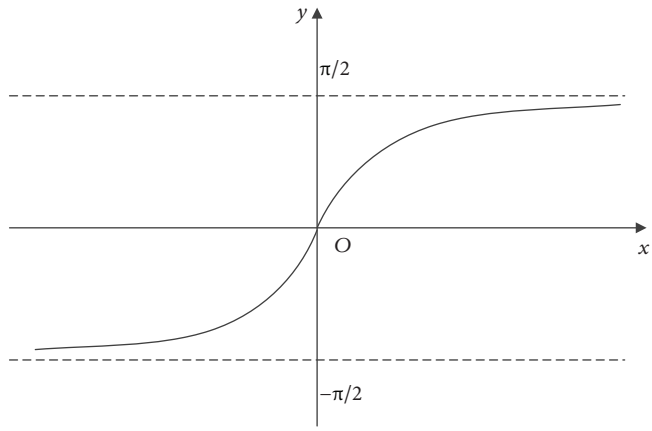

Figure 5: Inverse tangent function curve.

In the case of data loss, we compare our method with the inverse-distance-weighted interpolation algorithm in terms of interpolation accuracy. Then $q_{s_i} = 0$. Since the data acquisition nodes for data loss are random, we conducted 20 tests for a more accurate comparison. Obviously, it is necessary that the number of acquisition node points for data loss be less than or equal to the total number of acquisition nodes. The results are shown in Figures 8 and 9.

As can be seen from Figures 8 and 9, as the proportion of lost data in all collected data decreases, the error of interpolation is gradually reduced. The curve of the proposed algorithm is relatively flat, indicating that it is less affected by data loss.

In the case of data loss, especially when the number of data acquisition nodes is relatively small, the interpolation error of our algorithm is much smaller than that of the inverse-distance-weighted interpolation.

In the case of data disturbance, we compare our method with the inverse-distance-weighted interpolation algorithm in terms of interpolation accuracy. Then $q_{s_i} = \text{No}(d_{s_i}(t_l), \sigma^2)/d_{s_i}$. For the interpolation of temperature, we use the mean temperature of all acquisition nodes as the mean value of the Gauss distribution. We set the parameters

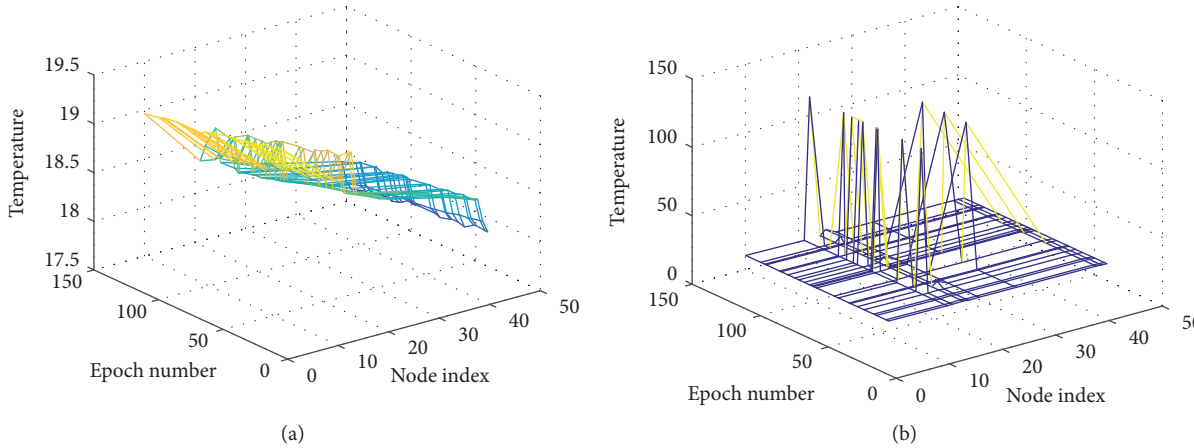

Figure 6: The temperature sensing data from the Intel Berkeley Research lab: (a) the filtered sensing data; (b) the actual sensing data.

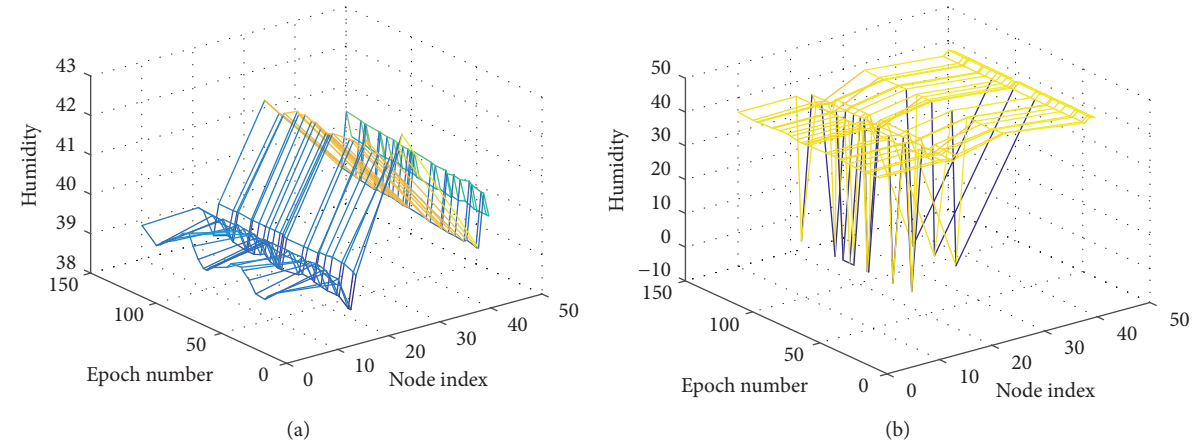

Figure 7: The humidity sensing data from the Intel Berkeley Research lab: (a) the filtered sensing data; (b) the actual sensing data.

as $d_{s_i}(t_l) = 18.47895$ and $\sigma^2 = 18$; for the interpolation of humidity, we use the mean humidity of all acquisition nodes as the mean value of the Gauss distribution. We set the parameters as $d_{s_i}(t_l) = 39.44691$ and $\sigma^2 = 39$. Again, we did 20 tests. The results are shown in Figures 10 and 11.

It can be seen from Figures 10 and 11 that the variation curve of the proposed algorithm is relatively flat, while the curve of the inverse-distance-weighted interpolation algorithm fluctuates greatly. The interpolation error of the IDWI algorithm is not only affected by data disturbance but also affected by the deployment location of the data acquisition nodes. When 7 acquisition nodes are deployed, the error of the IDWI algorithm is the smallest. Because sensor placement based on the iterative dividing four subregions is near uniform deployment when 7 acquisition nodes are deployed, the interpolation error is small.

In the case where there are not many acquisition nodes, the density of the acquisition nodes where data disturbance occurs is large, so the error of interpolation is more prominent. The number of sensors that can be deployed increases, and the error of interpolation is also reduced.

As we can see from Figures 8–11, our algorithm is insensitive to errors and strong in robustness when the data is wrong, while the inverse-distance interpolation method has a great influence on the interpolation accuracy of the error data. In particular, when the error rate is high, the relative error of our algorithm is much lower than that of the inverse-distance interpolation algorithm. When the error rate is 50%, our algorithm has a relative error of 0.1 and the relative error of the inverse-distance interpolation algorithm is 3.5, as shown in Figure 9(a).

7. Conclusions

In this paper, we proposed a robust data interpolation based on a back propagation artificial neural network operator for incomplete acquisition in a wireless sensor network. Under the incomplete collection strategy of WSN, the effect of complete acquisition can be approximately obtained by interpolation. In the case of limited data acquisition nodes, the data of the acquisition nodes are used to train to obtain the learning operator. Then, the learning operator of the acquisition node

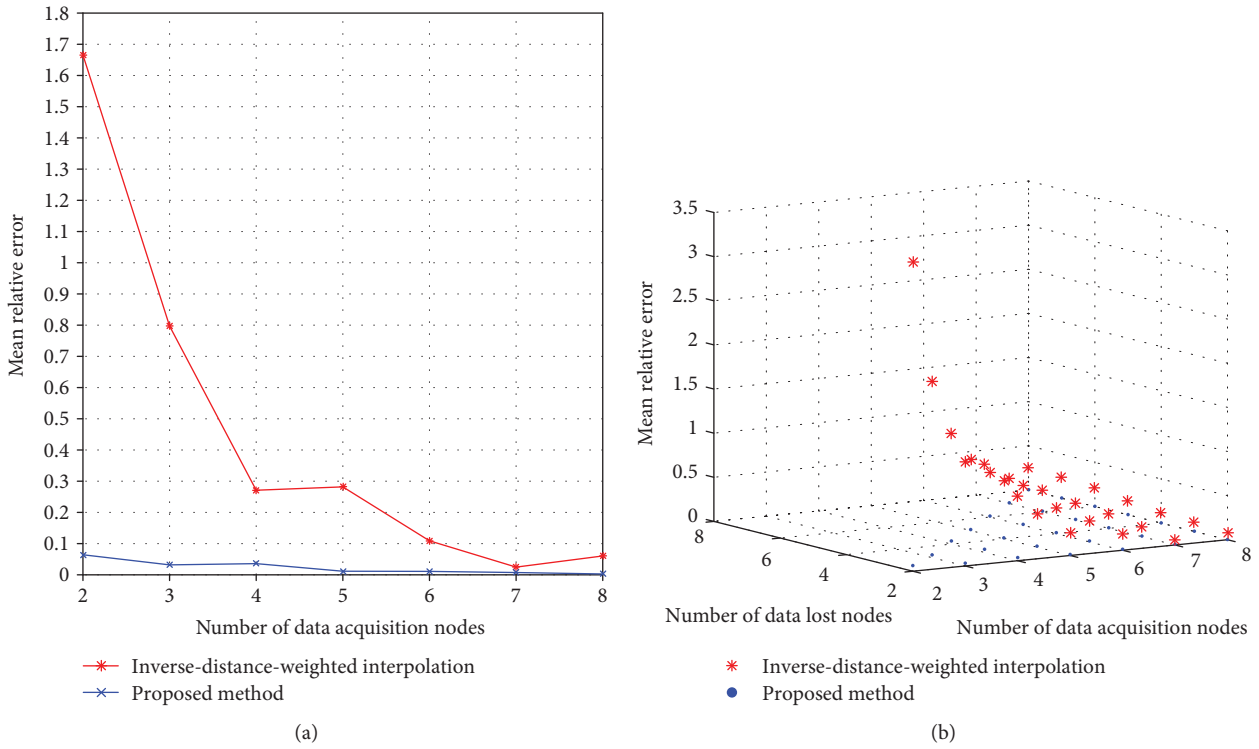

Figure 8: The temperature sensing data from the Intel Berkeley Research lab: (a) data loss occurred at 1 data acquisition node; (b) data loss occurred at data acquisition nodes increased from 2 to 8.

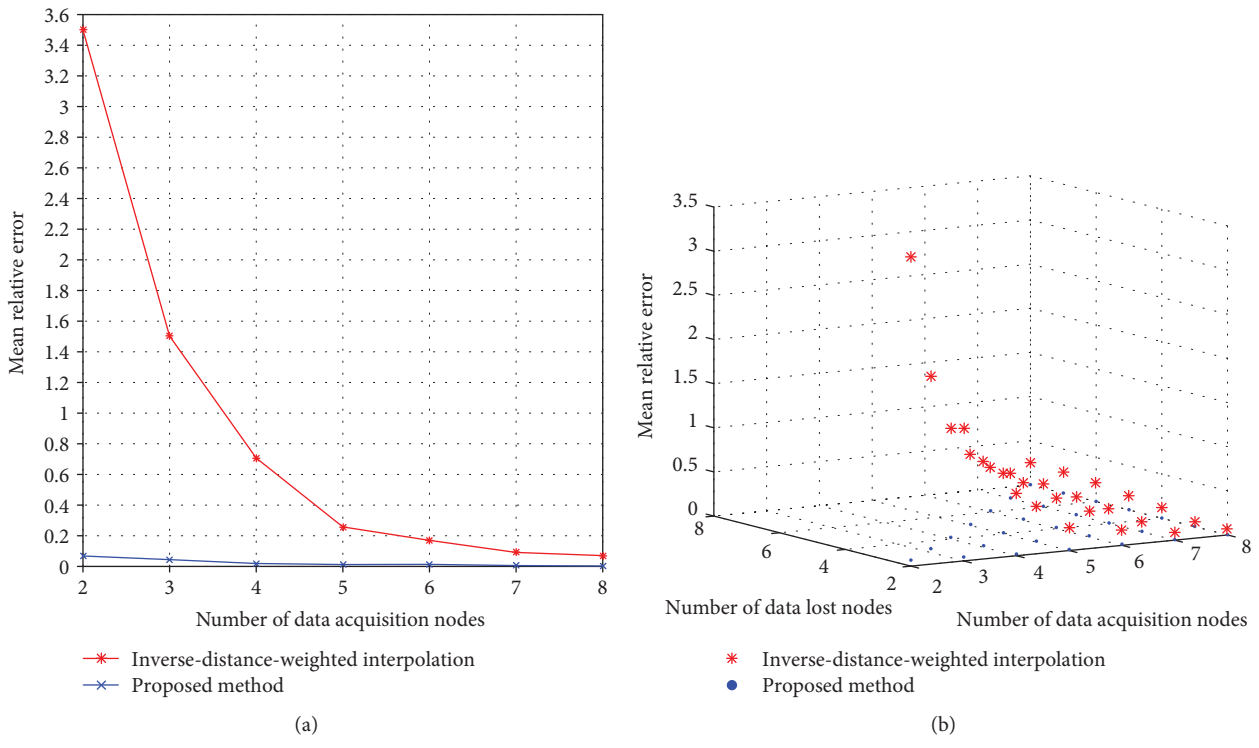

Figure 9: The humidity sensing data from the Intel Berkeley Research lab: (a) data loss occurred at 1 data acquisition node; (b) data loss occurred at data acquisition nodes increased from 2 to 8.

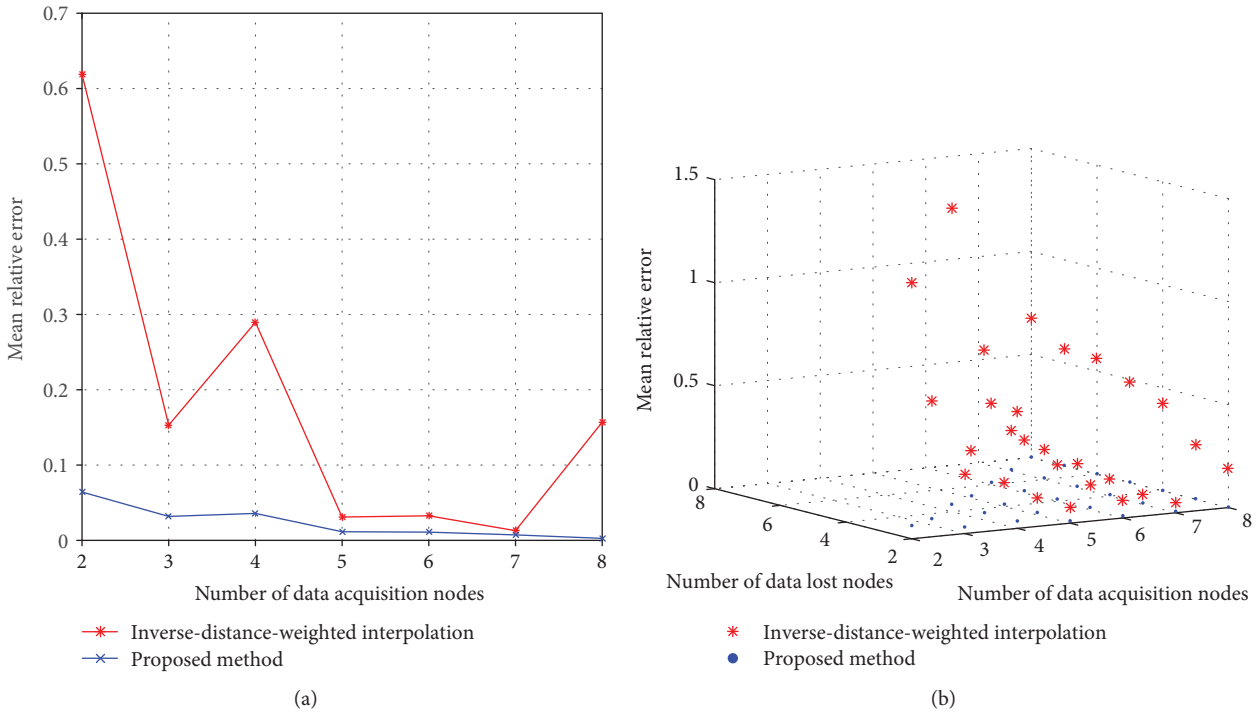

Figure 10: The temperature sensing data from the Intel Berkeley Research lab: (a) data disturbance occurred at 1 data acquisition node; (b) data disturbance occurred at data acquisition nodes increased from 2 to 8.

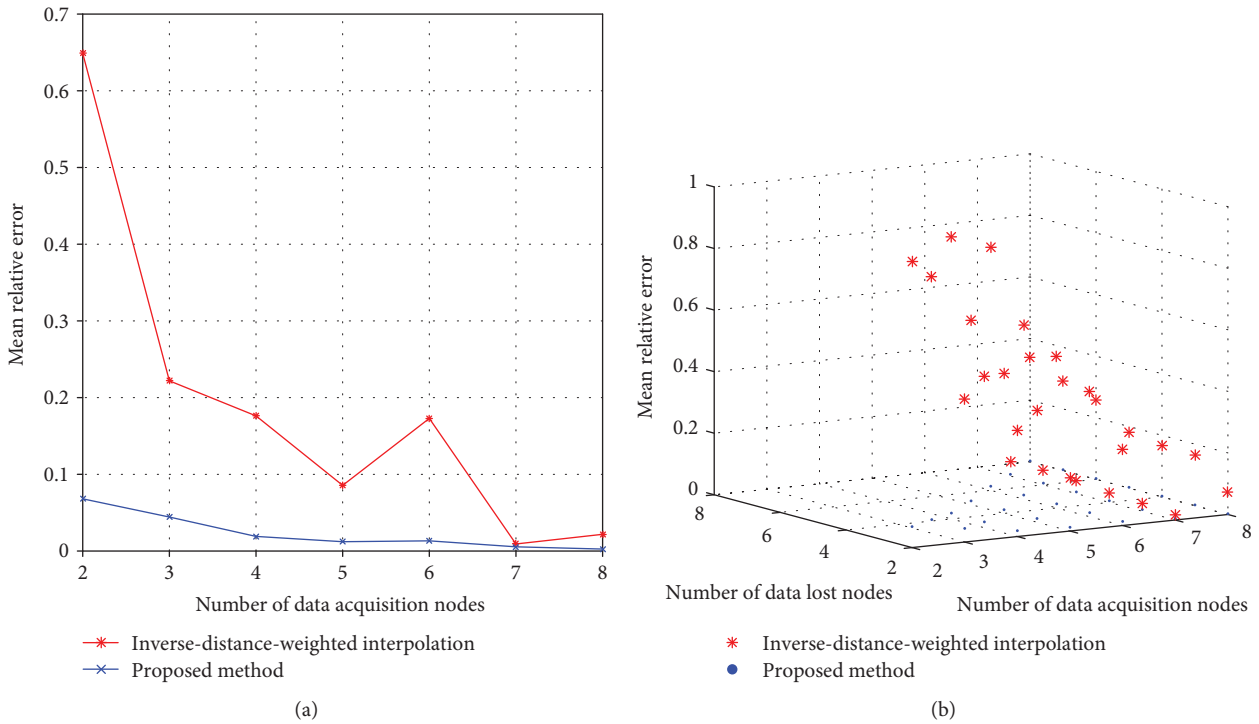

Figure 11: The humidity sensing data from the Intel Berkeley Research lab: (a) data disturbance occurred at 1 data acquisition node; (b) data disturbance occurred at data acquisition nodes increased from 2 to 8.

closest to the non-data acquisition location is transferred to the non-data acquisition location for interpolation. Considering that the data collected by WSN is prone to error, we analyzed the reasons for the error. In order to improve the fault tolerance and robustness of the interpolation algorithm, we proposed a BP artificial neural network learning

operator. From the experiments, we demonstrated that our algorithm has strong robustness, and it has a lower error in the case of data errors collected by the WSN. This method has strong potential for practical data visualization, data analysis, WSN monitoring, etc.

Data Availability

The measured data that support the findings of this study are supplied by Intel Berkeley Research lab. They are available from http://db.csail.mit.edu/labdata/labdata.html.

Conflicts of Interest

The authors declare that there is no conflict of interests regarding the publication of this paper.

Acknowledgments

This work was financially supported by the National Natural Science Foundation of China (Grant Nos. 61561017 and 61462022), the Innovative Research Projects for Graduate Students of Hainan Higher Education Institutions (Grant No. Hyb2017-06), the Hainan Province Major Science & Technology Project (Grant No. ZDKJ2016015), the project of the Natural Science Foundation of Hainan Province in China (Grant No.617033), the open project of the State Key Laboratory of Marine Resource Utilization in South China Sea (Grant No. 2016013B), and the Key R&D Project of Hainan Province (No. ZDYF2018015).

References

[1] F. Ding and A. Song, "Development and coverage evaluation of ZigBee-based wireless network applications," *Journal of Sensors*, vol. 2016, Article ID 2943974, 9 pages, 2016.

[2] O. Alvear, W. Zamora, C. Calafate, J. C. Cano, and P. Manzoni, "An architecture offering mobile pollution sensing with high spatial resolution," *Journal of Sensors*, vol. 2016, Article ID 1458147, 13 pages, 2016.

[3] W. Xiao, *The Key Technology of Adaptive Data Fault Tolerance in Wireless Sensor Networks*, National Defense University of Science and Technology, Hunan, China, 2010.

[4] Z. Liang, F. Tian, C. Zhang, H. Sun, A. Song, and T. Liu, "Improving the robustness of prediction model by transfer learning for interference suppression of electronic nose," *IEEE Sensors Journal*, vol. 18, no. 3, pp. 1111–1121, 2017.

[5] Z. Yang, W. Qiu, H. Sun, and A. Nallanathan, "Robust radar emitter recognition based on the three-dimensional distribution feature and transfer learning," *Sensors*, vol. 16, no. 3, pp. 289–303, 2016.

[6] S. J. Pan and Q. Yang, "A survey on transfer learning," *IEEE Transactions on Knowledge and Data Engineering*, vol. 22, no. 10, pp. 1345–1359, 2010.

[7] B. Pan, J. Tai, Q. Zheng, and S. Zhao, "Cascade convolutional neural network based on transfer-learning for aircraft detection on high-resolution remote sensing images," *Journal of Sensors*, vol. 2017, Article ID 1796728, 14 pages, 2017.

[8] J. Park, R. Javier, T. Moon, and Y. Kim, "Micro-Doppler based classification of human aquatic activities via transfer learning of convolutional neural networks," *Sensors*, vol. 16, no. 12, pp. 1990–2000, 2016.

[9] http://db.csail.mit.edu/labdata/labdata.html.

[10] Z. Kang and Y. Wang, "Structural topology optimization based on non-local Shepard interpolation of density field," *Computer Methods in Applied Mechanics and Engineering*, vol. 200, no. 49-52, pp. 3515–3525, 2011.

[11] M. Hammoudeh, R. Newman, C. Dennett, and S. Mount, "Interpolation techniques for building a continuous map from discrete wireless sensor network data," *Wireless Communications and Mobile Computing*, vol. 13, no. 9, pp. 809–827, 2013.

[12] M. Saberi, A. Azadeh, A. Nourmohammadzadeh, and P. Pazhoheshfar, "Comparing performance and robustness of SVM and ANN for fault diagnosis in a centrifugal pump," in *19th International Congress on Modelling and Simulation*, pp. 433–439, Perth, Australia, 2011.

[13] R. Velazco, P. Cheynet, J. D. Muller, R. Ecoffet, and S. Buchner, "Artificial neural network robustness for on-board satellite image processing: results of upset simulations and ground tests," *IEEE Transactions on Nuclear Science*, vol. 44, no. 6, pp. 2337–2344, 1997.

[14] A. Venkitaraman, A. M. Javid, and S. Chatterjee, "R3Net: random weights, rectifier linear units and robustness for artificial neural network," 2018, https://arxiv.org/abs/1803.04186.

[15] C. Zhang, X. Zhang, O. Li et al., "WSN data collection algorithm based on compressed sensing under unreliable links," *Journal of Communication*, vol. 37, no. 9, pp. 131–141, 2016.

[16] H. L. Chen and W. Peng, "Improved BP artificial neural network in traffic accident prediction," *Journal of East China Normal University (Natural Science)*, vol. 2017, no. 2, pp. 61–68, 2017.

[17] G. Y. Lu and D. W. Wong, "An adaptive inverse-distance weighting spatial interpolation technique," *Computers & Geosciences*, vol. 34, no. 9, pp. 1044–1055, 2008.

Hindawi
Journal of Sensors
Volume 2018, Article ID 1253752, 12 pages
https://doi.org/10.1155/2018/1253752

Research Article

An Indoor and Outdoor Positioning Using a Hybrid of Support Vector Machine and Deep Neural Network Algorithms

Abebe Belay Adege,[1] **Hsin-Piao Lin**,[2] **Getaneh Berie Tarekegn**,[1] **Yirga Yayeh Munaye**,[1] **and Lei Yen**[2]

[1]*Department of Electrical Engineering and Computer Science, National Taipei University of Technology, Taipei, Taiwan*
[2]*Department of Electronic Engineering, National Taipei University of Technology, Taipei, Taiwan*

Correspondence should be addressed to Abebe Belay Adege; abbblybelay@gmail.com

Received 9 July 2018; Accepted 25 October 2018; Published 16 December 2018

Guest Editor: Almudena Rivadeneyra

Indoor and outdoor positioning lets to offer universal location services in industry and academia. Wi-Fi and Global Positioning System (GPS) are the promising technologies for indoor and outdoor positioning, respectively. However, Wi-Fi-based positioning is less accurate due to the vigorous changes of environments and shadowing effects. GPS-based positioning is also characterized by much cost, highly susceptible to the physical layouts of equipment, power-hungry, and sensitive to occlusion. In this paper, we propose a hybrid of support vector machine (SVM) and deep neural network (DNN) to develop scalable and accurate positioning in Wi-Fi-based indoor and outdoor environments. In the positioning processes, we primarily construct real datasets from indoor and outdoor Wi-Fi-based environments. Secondly, we apply linear discriminate analysis (LDA) to construct a projected vector that uses to reduce features without affecting information contents. Thirdly, we construct a model for positioning through the integration of SVM and DNN. Fourthly, we use online datasets from unknown locations and check the missed radio signal strength (RSS) values using the feed-forward neural network (FFNN) algorithm to fill the missed values. Fifthly, we project the online data through an LDA-based projected vector. Finally, we test the positioning accuracies and scalabilities of a model created from a hybrid of SVM and DNN. The whole processes are implemented using Python 3.6 programming language in the TensorFlow framework. The proposed method provides accurate and scalable positioning services in different scenarios. The results also show that our proposed approach can provide scalable positioning, and 100% of the estimation accuracies are with errors less than 1 m and 1.9 m for indoor and outdoor positioning, respectively.

1. Introduction

In the Internet of Things (IoT) era, indoor and outdoor positioning plays various roles to find the location of people, mobile devices, and equipment. Because of the popularities of social networks and the widespread usage of mobile devices, demands for location-based services (LBS) are increased in both indoor and outdoor environments [1, 2]. Positioning can be considered as a key technology to IoT, since it uses to provide situation-awake services in various applicable areas [3, 4]. Human daily life is also becoming highly integrated with the IoT as the Internet attracts much attention with respect to the outlook of future life and rapidly increases communication networks. Additionally, rapid technological growths cause to increase positioning services. In [5], positioning is one of the primary services in the IoT era.

Indoor and outdoor positioning can be applied in university, airport, military system, security system, Metro Service-Route Map (MRT), farming, and forest areas. Moreover, we can apply in diverse services, such as emergency management, track mobile users, context awareness, advertisement, environmental monitoring, military surveillance, and medical care applications [6]. According to [7, 8], positioning serves to address problems such as traffic loads in 5G networks. Therefore, indoor and outdoor positioning

requires enormous attention to be effectively implemented in industry and academia, since precise positioning is used as an enabling factor for the future IoT [4, 9].

There are two main positioning schemes: range-based scheme and range-free scheme [10, 11]. In the range-based scheme, the distances and/or angles are used for positioning. This scheme includes received signal strength (RSS), time of arrival (ToA), time difference of arrival (TDoA), and angle of arrival (AoA) as a means of positioning. However, the range-free scheme performs positioning using the connections between different devices or the pattern matching between different devices. It includes the centroid algorithm (CA), the distance vector hop (DV-hop) algorithm, the multidimensional scaling map (MDS-MAP) algorithm, and convex programming approaches. It is highly depending upon regular sensor deployment area, which is very difficult in irregular and hierarchical environments. According to [7, 10], range-based positioning is more accurate, simpler, and lower-cost than the range-free approach.

Wireless local area network (WLAN), infrared (IR), radio-frequency identification (RFID), ultrasound, and Bluetooth technologies are the main indoor positioning approaches. However, Wi-Fi is common in IoT eras, because we can mount the Wi-Fi connections in various locations without any new infrastructures and additional cost. Besides, data collection using Wi-Fi devices is cheaper, for example, using access points (APs) [12].

As discussed in [11], GPS and the standalone cellular system are the most promising and accurate positioning technologies for outdoor positioning. According to [13], an outdoor positioning can be done by using the ubiquitous mobile network Base Stations (BS). However, the accuracy in outdoor positioning is highly depending on the number of surrounding BS [14]. The highly irregular and nonstatic environments easily affect the positioning accuracies in an outdoor environment, since even small changes lead to significant changes in the corresponding scans. GPS-based positioning has limitations to outdoor navigation and experience severe signal loss in urban areas [15]. Outdoor positioning using fixed sensors or GPS-based sensors is very expensive [8]. Hence, both indoor positioning and outdoor positioning require special attention to be accurate and have cheaper application.

There are two types of Wi-Fi-based positioning technologies [16]: time and space attributes of received signal- (TSARS-) based technology and received-signal strength- (RSS-) based positioning technology. The former approach includes TDoA, AoA, and ToA. This type of approach has many difficulties when measuring the radiofrequency (RF) signal in a complex environment, so that it affects positioning accuracies. Contrarily, RSS-based positioning technology uses RSS to find the users' position. RSS-based positioning technology has advantages of lower cost, fewer operational complexity, lower power consumption, and easiness in mapping into different areas [12, 16]. Positioning using RSS in wireless environments helps to provide location services without additional sensor costs. In wireless positioning techniques, we can possibly develop a system through error minimization in cheaper cost and lower computational time. Generally, Wi-Fi-based positioning can be functional anywhere wireless services are available.

As pointed in [16], there are three kinds of RSS-based positioning: trilateration, approximate or similarity perception, and scene analysis. The trilateration approach requires at least three APs to convert received signal into spatial distance. However, it is very difficult to convert signal into distance in complicated and hierarchical environments. The approximation-perception method is relatively simple although it has lower positioning accuracy. Scene analysis, also known as fingerprint matching, does not require the locations of the APs. In this approach, the algorithms can obtain the precise position of Wi-Fi users. The scene analysis is characterized by low cost, high precision, and low-energy consumption, so that this method gets much attention [7, 8, 12, 16].

According to [17], Wi-Fi-ranging and Wi-Fi-fingerprinting are the two main methods to deliver Wi-Fi-based positioning. The former approach is implemented by measuring the distance towards the node. This type of approach is impractical inside complex, dynamic, and hierarchical environments due to numerous signal obstructions. Conversely, in Wi-Fi fingerprinting methods, positioning is operated by comparing the current data through the prerecorded datasets. This approach requires larger amounts of stored datasets. The wireless signal variations are not also considered, which affect positioning accuracies.

Previous researchers have proposed different machine learning methods, such as radial basis function network and particle filter [3], support vector regression (SVR) [9], artificial neural network (ANN) [18], K-nearest neighbors (KNN) [19, 20], feed-forward neural network (FFNN) [21], weighted KNN (WKNN) [22], and KNN and ANN backpropagation (ANNBP) [23] to maintain positioning accuracies. In [3], radial basis function network and particle filter algorithms did the positioning and tracking. The authors used RFID and IR as a means of data sources using sensors. This type of approach requires higher cost, since it needs additional hardware and requires aggressive data collection processes. In [9], SVM and ANN were used to locate in an indoor environment. This work focused to locate APs in an indoor environment, and outdoor positioning was not considered. An ANN algorithm and ToA and AoA data sources were used for indoor positioning [18]. This approach has operational complexity, and it is difficult to locate accurately because of line-of-sight (LoS) problems. In [20], KNN was used to estimate the current position of a mobile user using historical data. This approach is very difficult to get accurate positioning values, since RSS is highly time-dependent. The KNN and Kalman filter algorithms were applied for indoor positioning [19]. This work required extra hardware for data collection.

In [24], the combination of indoor and outdoor positioning was done in athletic training and gymnasium areas. The authors used GPS with microelectromechanical system (IMU-MEMS) technology for outdoor positioning and ultra-wideband (UWB) with IMU-MEMS technology for indoor positioning to provide high precision positioning services. In [15], single body-mounted camera and computer

vision techniques were applied for outdoor positioning. This approach is too expensive because of requiring extra hardware and much storages. Authors in [25] compared GPS, global system for mobile communication (GSM), WLAN, and Bluetooth to apply to indoor and outdoor positioning, and the result showed that GPS and WLAN offer the most harmonizing accuracy. However, this work required extra terminals to integrate GPS and WLAN devices.

Positioning accuracy, in complex environments, using shallow-learning approaches is usually unsatisfactory in larger datasets, because the algorithms learn poorly. More specifically, traditional approaches have poor learning capabilities in complex and dynamic wireless environments, since there are many Wi-Fi-signal changing factors, such as multipath fading, attenuation of objects, or non-line of sights.

In this paper, we propose to use the integration of FFNN, linear discriminate analysis (LDA), SVM, and deep neural network (DNN) algorithms for scalable and accurate positioning, as proposed in our previous work [26]. We use LDA for dimension reduction, as well as hybrid of SVM and DNN as a means to locate the actual position of smartphone users. Additionally, we apply the FFNN algorithm for automatic bursting the missed RSS values before LDA is applied in both training and testing phases. If there will be more than one feature having missed RSS values, then the proposed system fills RSS values in each feature iteratively. The use of IoT helps to enhance accuracy, minimize computational time, and yield benefits of larger numbers of datasets. To find the target of smartphone users, we use a hybrid of SVM and DNN algorithms. The performances of our proposed method are evaluated in different scenarios, which helps to evaluate the scalability and the accuracy of our system performances.

The main contribution of this paper is to provide universal positioning services as it focuses on indoor and outdoor positioning, to deliver accurate positioning as we apply IoT and minimize positioning time complexities. Additionally, the proposed approach provides scalable positioning whenever trained APs are unable to offer Wi-Fi signal. To the best of our knowledge, this article is the first to present the integration of IoT, such as FFNN, LDA, SVM, and DNN algorithms to provide scalable and accurate positioning in indoor and outdoor environments.

The rest of this paper is organized as follows. In Section 2, we discuss related works. In Section 3, we discuss data collection approaches. Section 4 presents the details of the proposed technique. The results and discussions are presented in Section 5. Finally, conclusions of the work are given in Section 6.

2. Related Works

Indoor positioning and outdoor positioning using traditional machine-learning techniques in a Wi-Fi-based dynamic environment are not accurate and robust because the machine is unable to adapt to signal oscillations, noises, and radio signal fluctuations. DNN has been proposed as a new strategy due to the fact that it helps to handle traditional learning problems. The discussion in [12] shows that DNN is used for easy adaptation of data variations, management of the dins of Wi-Fi signal, and device and time obsessions of wireless signal because it has advanced learning capability from complex and larger datasets. According to [17, 27, 28] discussions, the DNN is used to reduce positioning workloads, to improve the accuracy of Wi-Fi-based positioning, and to provide efficient positioning services, because DNN has deeper learning capabilities and efficient prediction performances.

In [29], the four-layered DNN was proposed for indoor and outdoor positioning. In this work, the stacked denoising autoencoder (SDA) and Hidden-Markov model (HMM) were used to minimize features without affecting information contents and to smooth the original locations, respectively. The performance of the work was evaluated using root mean square errors (RMSEs) in various testing sets. In this work, the scalability issue was not addressed for indoor and outdoor positioning. Additionally, system performances for indoor and outdoor positioning were evaluated at different numbers of layers and neurons, which makes it difficult to reach concise points about system performances. Kim et al. [12] used DNN for indoor positioning via radio signal values. In this work, system performance is evaluated by comparing epoch sizes only. However, other machine learning factors such as gradients and batch sizes were not considered. In [17], the deep learning algorithm was applied for building and floor-level classification using publicly offered data. In this work, SDA and deep learning were used for dimensional reduction and classification-based positioning, respectively. In [30, 31], deep learning was applied for indoor positioning. In these papers, researchers used channel state information (CSI) as means of data sources. However, this approach is very difficult to validate the system performances since the actual target is not clearly known because of data natures.

The FFNN-based algorithm was applied for indoor positioning using datasets collected from multiple buildings and floors experimentally and attained 99.82% and 91.27% accuracies, respectively [32]. This work did not focus the outdoor scenarios. In [33], classification-based positioning was applied using RSS values. In this work, the largest RSS values were selected to train the positioning algorithm. However, this approach is very problematic to evaluate when there are similar RSS distributions. In [34], the radial basis function (RBF) was applied to locate the mobile users in an indoor environment only. Since AoA was used as a means of data collection approach, the proposed technique has LoS problem. In [35], multilayer perceptron (MLP) was applied for indoor positioning. A limited number of APs were used in a building. Additionally, the scalability and robustness of the proposed method were not considered. In [36], MLP and KNN were used as a range-free positioning approach to select the better algorithm and found that MLP has better performances in different sample sizes.

Petr et al. [13] used UWB to indoor positioning and real-time kinematic global navigation satellite system (GNSS) through several BS to outdoor positioning. This work used TDoA to collect required datasets. In [37], indoor positioning and outdoor positioning were operated using two sensors, and system performance was assessed

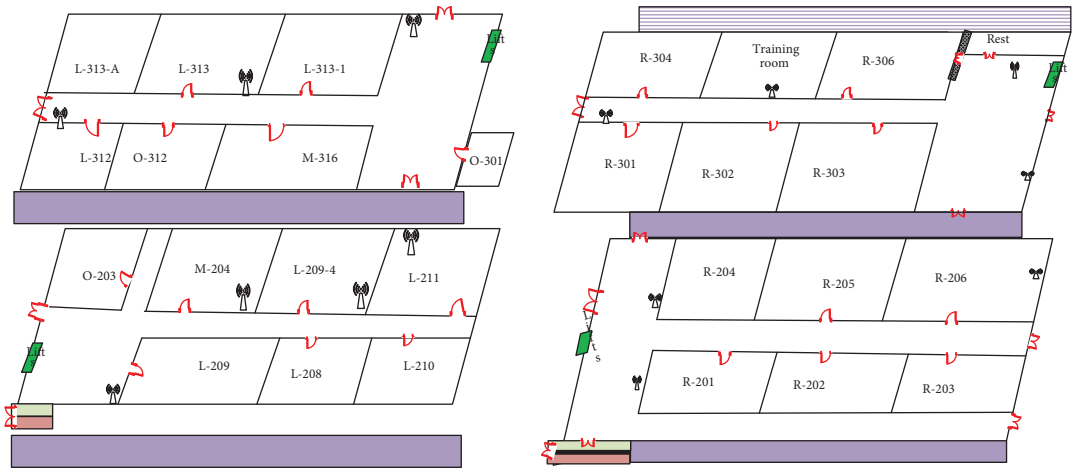

(a) Internal structures of building-1

(b) Internal structures of building-2

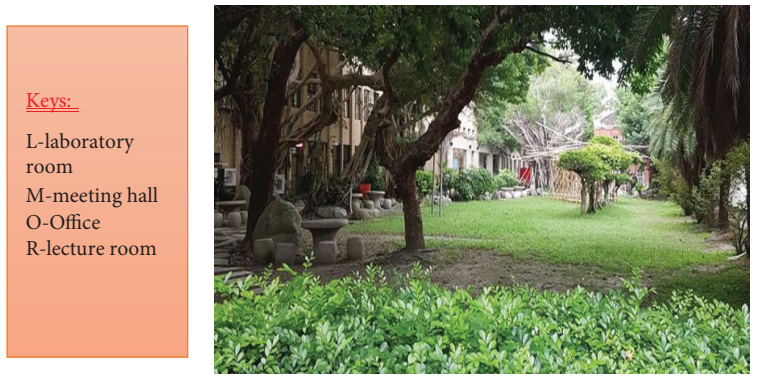

(c) Outdoor environment

Figure 1: Structures of the indoor and outdoor environments.

using high-speed robot Kurt 3D equipped with the 3D laser scanner. This approach is accurate positions; however, it is not cost-effective because of using robots and sensors. In [2], a distributed-based positioning was implemented for indoor and outdoor positioning. This approach used infrared sensors and a GPS receiver deployed in working environments. The range-free approach using the DV-hop algorithm in DNN technology was implemented to locate positions [6]. This work focused on range-free positioning, which causes high computational complexity in a larger number of users. The authors in [38] combined the SVM and ANN to estimate users' position using RSS values. Scholars showed that the combination of SVM and ANN increased the accuracy rate by 5% than using SVM alone. This work focused on boundary-level localizations rather than showing a specific location of smartphone users. In [39], device-free passive localization (DfPL) by applying SVM and MLP was done. This work focused on identifying whether there are more than one person in a certain bounded location. Authors used wireless sensor networks (WSNs) with DfPL, which causes computational cost problems.

This paper is the extended part of our previous work [26], which focused on the application of LDA for feature reduction, and MLP for classification and regression in an indoor environment. The scalability of positioning in an indoor and outdoor environment was not addressed, and they left as future works. The application of IoT was not also addressed. In [29], the DNN was applied to increase the estimation accuracy and reduce generalization errors on a dynamic indoor environment. This was done using only six APs and fewer datasets in a building. The IoT was not used to enhance positioning performances. The aim of our work is to apply IoT for scalable and accurate positioning in indoor and outdoor environments. To achieve our goal, we use FFNN, LDA, SVM, and DNN iteratively. As far as the authors' knowledge, this work is originally presented for the first time.

3. Working Environments and Experimental Data Collection

For this work, the datasets are collected from the real environment in National Taipei University of Technology (NTUT). The indoor environment's internal structures and physical layout of the outdoor environment are demonstrated in Figure 1. For indoor positioning, we use two buildings: complex building (building-1) and the academic building (building-2) as presented in Figures 1(a) and 1(b), respectively. In building-1, we consider workshops, halls,

and staffs' offices. In building-2, lecture rooms are considered. Additionally, the corridors of each building are considered as working places. For outdoor positioning, we consider the selected green area found in the university, as shown in Figure 1(c). The RSS and basic service set identifier (BSSID) datasets are used as data sources for the proposed positioning approach, since collecting RSS and BSSIDs from APs does not require additional infrastructure and hardware. In both indoor and outdoor working environments, datasets are collected from each reachable APs using smartphones.

For easily managing and collecting larger training datasets, we use $1\,\text{m} \times 1\,\text{m}$ grids in both indoor and outdoor environments. This results in making the DNN easily adapt to the data fluctuations. In [3], the performance of machine-learning techniques in different grids was compared: $1\,\text{m} \times 1\,\text{m}$, $1\,\text{m} \times 2\,\text{m}$, $1\,\text{m} \times 1.5\,\text{m}$, $2\,\text{m} \times 2\,\text{m}$, and $2\,\text{m} \times 2.5\,\text{m}$ grids. The $1\,\text{m} \times 1\,\text{m}$ grids have better performance than others do. The schemes in [40] used $1\,\text{m} \times 1\,\text{m}$ grids.

In this paper, we use similar grid sizes to evaluate the proposed system uniformly in both indoor and outdoor environments at a time. Moreover, it helps to develop a system that serves equally for indoor and outdoor positioning. In the indoor and outdoor environments, we collect data through an experiment from a real-world environment. In [21], authors discussed that the use of numerous datasets at each grid helps to adapt to signal fluctuations easily. Hence, we collect 35 RSS values and 35 BSSIDs from each grid in 5 s intervals, periodically. The BSSIDs are used to identify each AP uniquely. It also helps to identify the missed RSS values in the testing phase. For this work, a total of 21,665 RSS values and 21,665 BSSIDs are collected from 619 grids in the indoor environment. Moreover, we collect 4200 RSS values and 4200 BSSIDs from 120 grids in the outdoor environment.

For this work, all reachable APs from unknown locations are used for data collection purposes to make the system inclusive and to train the machine deeply from various signal values. In complex and hierarchical environments, the AP locations may not be known. However, the datasets reached from each AP may be more important. Additionally, seven APs are used for data collection. During data collection, about 53 RSS values are reachable from indoor environments, and there are more than 94 APs that reached the outdoor environment. The signal that reached the outdoor environment is coming from different buildings around the working location. This implied that considering APs from unknown locations is very important in obtaining basic information.

As a general structure of the collected datasets, the RSS values and BSSIDs are the basic features, and the $x - y$ -coordinates are Wi-Fi users' locations that are recorded during data collection. The scanned datasets are recorded in the form of $[(R_k^1, \ldots \ldots R_k^p), (\text{BID}_k^1 \ldots \ldots \ldots \ldots \ldots \text{BID}_k^p), (X_i^a, Y_j^a)]$, where $(R_k^1 \ldots \ldots R_k^p)$ indicates the RSS values from AP_1 to AP_p at record $k \leq N$, $(\text{BID}_k^1 \ldots \ldots \ldots \ldots \ldots \text{BID}_k^p)$ are the recorded BSSIDs from AP_1 to AP_p, (X_i^a, Y_j^a) are the locations where RSSs and the BSSIDs are scanned, p is the reachable APs, k indicates the number of records, and i and j refers to X- and Y-coordinates of mobile users, respectively. In the experiment, we have seen that p ranges up to 53 and 94 for indoor and outdoor environments, respectively. However, the data collected from an outdoor environment has much signal fluctuation than data collected from an indoor environment. The record k ranges from 1 to 25,865 records. We use similar data structures of RSS and BSSID values for indoor and outdoor positioning scenarios. We use the (x, y) target values to handle the position of smartphone users.

4. Proposed System

In this section, we propose a hybrid of SVM and DNN algorithms as a positioning scheme at indoor and outdoor Wi-Fi-based environments. The discussion in [38] shows that SVM produces robust classification results. Moreover, SVM can be modeled with kernel functions like SVM-RBF kernel to handle nonlinear datasets. DNN is a deep machine-learning technique, which has better learning capability than other shallow-learning approaches [29]. Hence, we propose to combine the two technologies to find accurately the final target of the smartphone users. We have a number of reached APs in an outdoor environment than in an indoor environment. However, we only take the first 43 APs as input features to the LDA, because the signal values after the 43rd APs are more fluctuated in the outdoor environment and their values ranged below -85 dBm. Additionally, RSS values beyond 43 are -100 in an indoor environment. The missed RSS values from the first 43 APs are filled automatically using the FFNN algorithm through iterative regression. Hence, we used only the first 43 reached RSS values as input features to LDA.

In [41], the missed AP values were filled using the average RSS values. Nevertheless, replacing the missed AP values with a similar value is impractical to get accurate positioning in dynamic environments. In [42], the authors used selective APs for localization. This type of approach is very difficult to implement whenever they miss the larger numbers of APs. In our proposed system, the missed RSSs are bursting using the FFNN algorithm through iterative regression. In the FFNN application, the features with nonmissed RSS values are used as input features, and a feature with missed RSS values is taken as the target of the FFNN before LDA is applied in the training process. In this case, the missed records in a feature are filled at a time, since using a larger number of target-features causes to decline the accuracy. We observed that the majority of missed APs are found in the indoor environment than in the outdoor environment. The process proceeds until the empty values are packed appropriately. Once all data are appropriate, we apply LDA for dimensional reductions, since LDA is fast, accurate, and easy for our datasets. FFNN in the testing process is applied by taking the offline data as input features and the online data with missed RSS values as the target features.

The authors in [41] point out that the datasets with high dimension have drawbacks in positioning systems because it requires higher computational time and consumes larger

storage spaces. Moreover, it causes overfitting problems. Through appropriate application of dimensionality reduction techniques, it is possible to project a set of high-dimensional vector samples into a much lower dimensionality while preserving relevant information of the data. This is because the dimensionality reduction techniques are mainly used to reduce the redundant and dependent features by transforming higher dimensional features to lower-dimensional spaces. The authors in [43] proposed LDA to extract the most discriminative features by increasing the distance between classes under the constraint of keeping within-class scatter values. LDA is a fast and less complex approach for dimension reduction, so that it helps to improve computational complexity [41].

There are two main LDA techniques depending on the projected vector preparations: class-dependent and class-independent [41]. In class-dependent, the lower-dimensional space is calculated for each class independently. The number of projected vectors depends on the numbers of classes. This type of approach is complex for a large numbers of classes. However, class-independent LDA operations are computed by using one lower-dimensional space for all classes. This approach is simple and easy in complex and nonlinear datasets. To reduce dimensions of our data vectors, we propose to use a class-independent LDA technique because of its simplicity and ease.

The collected datasets are coded in different classes based on LoS, geographical settlements, working environments, and reference points. For example, we consider a room and a corridor in the same structure and the same LoS as a class. An outdoor environment is also considered as a class. Totally, we formulate the working environments in 10 classes. After the datasets are coded in classes and after bursting the missed RSSs, we apply LDA for feature reduction. In the dimensional reduction processes, we apply LDA to find the refined projected vector, the class mean, the total mean of the datasets, the between-class matrix, and the within-class matrix. Then, any data from a similar environment can be projected with the final lower-dimensional space to find the reduced and simpler vector for further position determination. The LDA is applied as shown in Equations (1), (2), (3), (4), (5), and (6). The datasets collected from each working area are represented as D_{nxm}, where n and m are the numbers of records and features, respectively.

(1) Assign each RSS vectors to the corresponding class C_c:

$$C_c = M_{rxN}, \tag{1}$$

where r is the record size in class C_c, and the class number c is ranged in [1, 10]. In RSS vectors, the record number in each class is always not greater than the total records.

(2) The mean to each class is calculated as shown in Equation (2) to demonstrate the effects of features in independent classes. The computation is done from the assigned data to each class, and then, finally, we obtained a $1 \times M$ matrix, where M is the total classes. Hence, we have a total of 1×10 mean vectors:

$$\mu_c = \frac{1}{n_c} \sum_{Di \pounds Cc}^{n} D_i, \tag{2}$$

where D_i is the original vector, $i \varepsilon c$, and μ_c is the mean value of individual class.

(3) The global mean, μ, is calculated from all datasets:

$$\mu = \frac{1}{n} \sum_{i=1}^{n} D_i, \tag{3}$$

(4) The variances of the between-class matrix are computed using the class mean and the global mean as shown in (4). This is mainly used for lowering dimensions and maximizing variances between classes:

$$S_b = \sum_{c=1}^{10} n_c (\mu_c - \mu)(\mu_c - \mu)^T. \tag{4}$$

(5) Calculate the variances of the within-class matrix, which is conducted by minimizing the difference between the projected mean and the projected samples of each class as shown

$$S_w = \sum_{c=1}^{10} \sum_{i=1}^{n_c} (D_{i,c} - \mu_c)(D_{i,c} - \mu_c)^T, \tag{5}$$

where ith and cth are the sample and the class in matrix $D_{i,c}$, respectively.

(6) Equation (4) and Equation (5) are combined to generate a lower-dimensional space:

$$W = {S_w}^{-1} S_b. \tag{6}$$

After calculating the lower-dimensional vector W, the representative features are selected as shown in Figure 2, where the larger variances are the most representative of the whole datasets. According to [44], the information contents of the nominated features should not be less than 90% of the whole information contents. Our chosen features comprehend the first top five features, which cover more than 98% of the information contents, as shown in Figure 2. This shows that the information content of the original datasets is not affected and its information content remains the same with original datasets. Once obtaining the lower-dimensional projected vector, we can transform any data from similar environments through the developed vector. The transformed vector should be the features that can denote all datasets to apply positioning algorithms.

We use the selected RSS features and five BSSIDs to both indoor and outdoor positioning. The five BSSIDs are selected

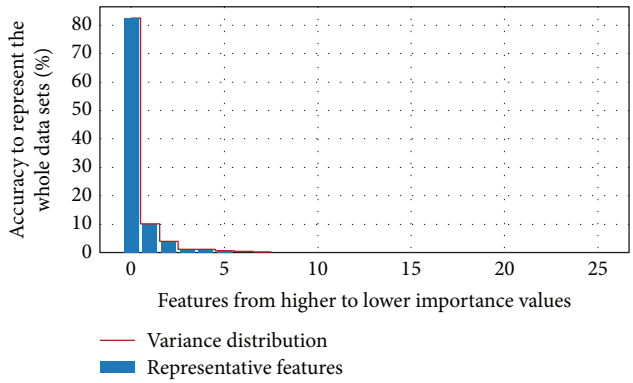

Figure 2: Feature distributions for LDA-based feature selections and the data variances.

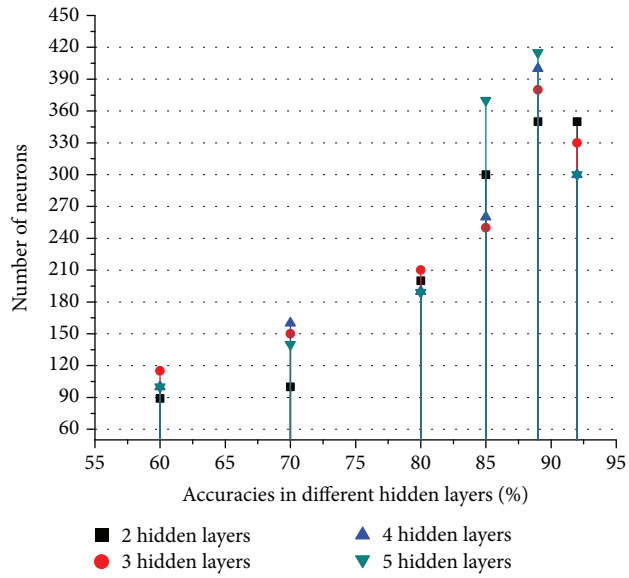

Figure 3: DNN performance with respect to numbers of hidden layers and numbers of neuron.

with the strongest RSS values, since AP-BSSIDs are unique and the signal strength in different locations varies for the APs. This helps to minimize the nonlinearity of RSS distributions. To evaluate the proposed approach, we select 70 locations from the indoor environment, and 8 locations from the outdoor environment. All testing locations are selected randomly from unknown locations. Our deep machine has an $I\_300\_300\_300\_300\_O_n$ structure, where I shows the input vector, and O_n is the corresponding output. The four hidden layers of the network are selected as an appropriate layer to our datasets, as shown in Figure 3. The structure of the DNN is selected by comparing numbers of hidden layers, such as two, three, four, and five hidden layers. Moreover, the numbers of neurons and the corresponding system performances are considered.

As illustrated in Figure 3, the numbers of hidden layers with respect to training accuracies and number of neurons achieve better accuracy at four hidden layers and 300 neurons. In five hidden layers, the accuracy is the same; however,

Table 1: Classifier algorithm performance comparisons.

Classifier algorithms		Average performances	
		Average precision	Average recall
1	KNN	0.92	0.94
2	ANN	0.91	0.96
3	SVM	0.99	0.99

we select four layers to minimize the computational complexity, since as the number of hidden layers is increased, the computational complexities, such as time complexity, will also increase. The observed variations of the local maxima are because of the data nature and environmental variations of the working environments.

Table 1 shows comparison between different classifier algorithms using the reduced RSS datasets having selected BSSIDs. In the localization process, we compare SVM-RBF with KNN and ANN algorithms to select the best classifier. The SVM-RBF has the best performance for larger classes compared with KNN and ANN. The SVM classification performance is nearly 100%, which is the best classifier compared to KNN and ANN. Therefore, we combine SVM-RBF with DNN to provide the (x, y) location with the best positioning performances.

Figure 4 shows the general structure of the proposed approach. Generally, after LDA is applied to reduce features, training and testing phases are operated. The green arrow shows the phase from preprocessing up to model construction for positioning. The blue arrow indicates the testing phase of the constructed model, providing the (x, y) location as a final target. In the training phase, we project the offline datasets to the LDA-based projected vector. Then, SVM-DNN algorithms were applied using the result data from the projected vector of the LDA technology to design an appropriate model. The proposed algorithms are carried out using Python 3.6 programming language with the TensorFlow framework because it is easy for the researchers.

In the testing phase, the online RSS values are used for position estimation from an unknown location. To identify the fail APs, we consider BSSIDs of the APs used in the offline phase to identify which is not available during online positioning. As authors presented in [45], positioning in a WLAN environment may have unexpected AP failure because of power outages, WLAN system maintenance, or temporary shutdown or permanent removal of APs. These cause positioning to be terminated due to scalability problems, which causes positioning services to be terminated for a while. Therefore, we should have a means of delivering a continuous positioning service when certain APs are unable to provide Wi-Fi services. Thus, before positioning, APs are checked by BSSIDs whether there are missed APs or not. If all APs can provide a Wi-Fi signal, localization continues using the proposed model. If there are missed APs, RSSs are filled automatically by regression using FFNN. It is necessary for reliable location estimations in case of unpredicted AP failures or malicious attacks, since it injects faults and compromises the presentation of the positioning system

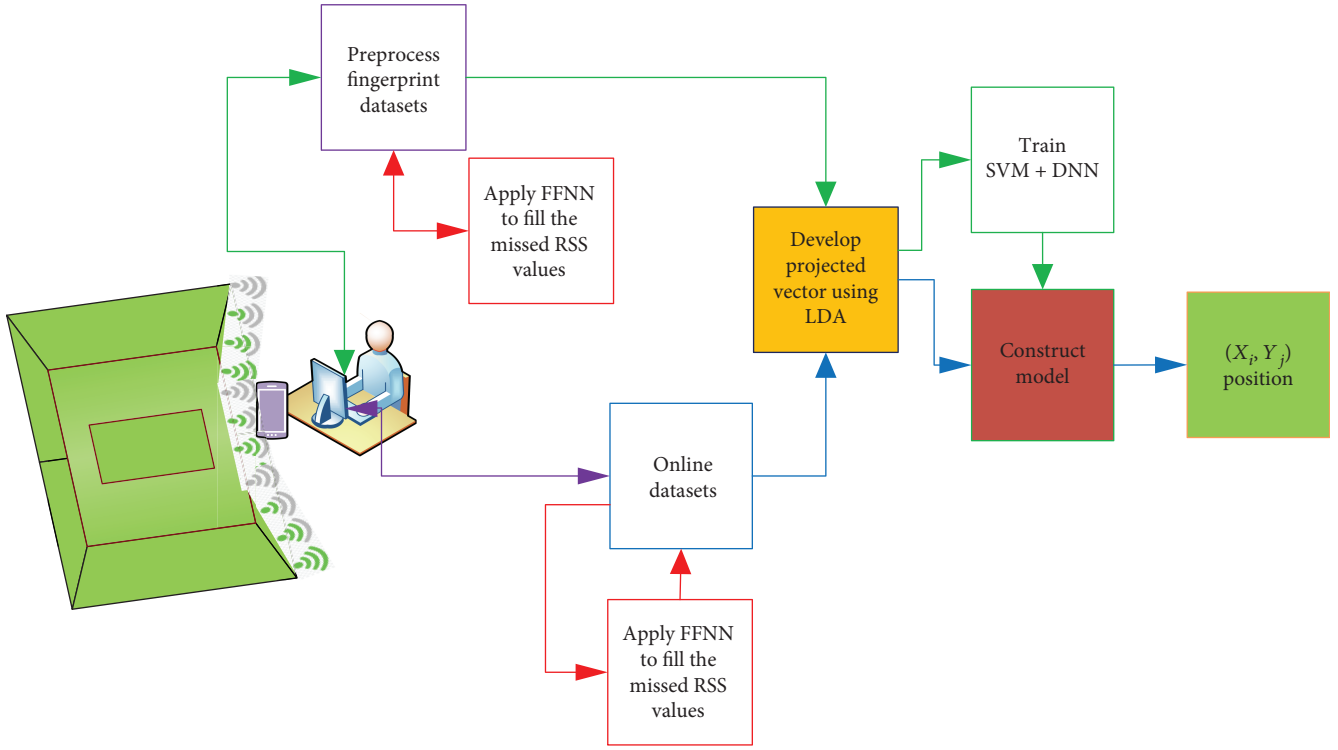

Figure 4: Proposed system structure.

[45]. Therefore, we use FFNN for filling the missed RSS values, since it is very fast and accurate for pattern recognitions [21]. Finally, localization is continuous through a designed model during training. Automatic filling of the missed values makes the proposed approach to provide continuous positioning services. Therefore, whenever the trained APs are unable to give Wi-Fi signal in the online stage, the system updates automatically to provide scalable positioning services. The aim of this work is to provide accurate and fault-tolerant positioning in location-data-requiring areas.

The proposed approach is evaluated mainly in terms of coordinate-based positioning of mobile users. Moreover, we use efficiency of the system performance, RMSEs, and system performance in certain ranges to evaluate the proposed approach. RMSE is computed as shown in

$$\text{RMSEs} = \sqrt{\sum_{i=1}^{k} \frac{(X_i^r - X_i^e)^2}{k}}, \tag{7}$$

where X_i^r is the real distance, X_i^e is the predictable distance at the ith point, and the total number of testing points is represented by k. The distance accuracy in each testing point is calculated in terms of position estimation errors, as in

$$\text{PEE}_i = \sqrt{(X_{ai} - X_{ei})^2 + (Y_{aj} - Y_{ej})^2}, \tag{8}$$

where PEE_i is the error of the proposed system at the ith location, X_{ai} is the actual distance from the X-coordinate, X_{ei} is the ith estimated distance from the X-coordinate, and Y_{aj} is the actual distance and Y_{ej} the estimated distance from the Y-coordinate.

Table 2: Positioning accuracies of the SVM-DNN algorithm in different ranges.

Scenarios	Estimated errors in different ranges (m)				Average Errors (m)
	<0.50 m	<0.75 m	<0.90 m	<0.95 m	
Scenario 1 (%)	57.14%	78.58%	95.71%	100%	0.48
Scenario 2 (%)	54.29%	75.71%	97.14%	100%	0.49
Scenario 3 (%)	51.43%	77.14%	92.86%	98.57%	0.51
Scenario 4 (%)	50%	70%	90%	95.71%	0.53

5. Results and Discussions

In this section, the testing results using a hybrid of SVM and DNN in wireless environments are presented to show the performance of the proposed method. In the positioning processes, the proposed method is evaluated in different scenarios: positioning without any missed APs as scenario 1, missing the one trained AP as scenario 2, missing the two trained APs as scenario 3, and missing the three trained APs as scenario 4. The proposed method is evaluated in terms of accuracy and scalability.

5.1. Indoor Positioning Results and Discussions. In this subsection, the proposed method's positioning performances in four different scenarios are discussed. Table 2 illustrates the indoor positioning performances in scenario 1, scenario 2,

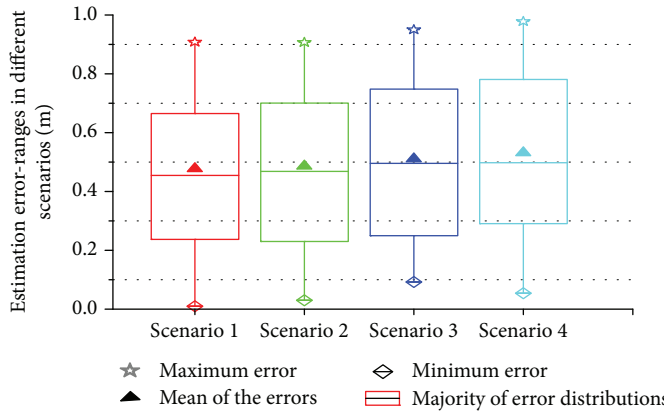

Figure 5: SVM-DNN positioning performance in different scenarios.

scenario 3, and scenario 4 using the SVM-DNN algorithm. A hybrid of the SVM and DNN technologies makes the positioning services continuous even when the trained APs are unable to provide a wireless signal. The performances of the proposed method are 57.14%, 54.29%, 51.43%, and 50% in scenario 1, scenario 2, scenario 3, and scenario 4 for estimation errors less than 0.50 m, respectively. The positioning errors less than 0.90 m covers 95.71%, 97.14%, 92.86%, and 90% for scenario 1, scenario 2, scenario 3, and scenario 4, respectively. All positioning errors are less than 1 m in each scenario. Majority of the errors are also less than 0.50 m in each scenario. The results indicate that indoor positioning is continuous when different trained APs are missed in the testing phase. This means that the integration of IoT and the automatic filling of missed RSS values can reduce performance degradation when APs get some troubles. To evaluate the proposed system performance, the missed APs are selected randomly from the first 43 APs. The performances of the proposed system show motivated results in each scenario. The performance is also nearly the same when one and two trained APs are missed. This indicates that the hybrid of the SVM and DNN algorithms also makes the positioning accuracy carry on robustly. This is because of the SVM kernels and the nonlinear activation function of the DNN to easily operate and understand nonlinear datasets. Additionally, the superior learning capacity of DNN and SVM makes the result to be more accurate. In each scenario, positioning accuracy has estimation errors less than 0.97 m, and the accuracies in similar ranges are nearly similar at each scenario.

The mean error difference between scenario 1 and scenario 4 is only 0.05, which is very small compared to the number of missed APs. The overall performances of the proposed system are accurate and scalable, since the algorithm makes to continuously locate the mobile users when the trained APs are missed.

Figure 5 presents the error distributions of the proposed system in four scenarios. It shows that the proposed system performances in terms of the minimum errors, mean of errors, maximum errors, and estimation error distributions in each scenario. The minimum error, mean of errors, and maximum error are 0.01 m, 0.48 m, and 0.90 m in scenario 1, respectively. In scenario 2, the minimum error is 0.03 m, the mean of errors is 0.48 m, and the maximum error is 0.90 m. Scenario 3 has 0.09 m, 0.51 m, and 0.95 m for the minimum, mean, and maximum errors, respectively. The minimum error, mean of errors, and maximum error in scenario 4 are 0.05 m, 0.53 m, and 0.97 m, respectively. The means of errors in scenario 1 and scenario 2 are similar. The majority of errors ranged from 0.23 m to 0.67 m in scenario 1, and it ranged from 0.22 m to 0.73 m in scenario 2. Hence, the proposed system performs with only a few shiftings in scenario 2 than in scenario 1. In general, the majority of error distributions in each scenario are the same. The automatic filling of the missed values using FFNN inspires positioning performances when APs are unable to give a Wi-Fi signal.

The result also indicates that the mean errors of the proposed algorithm in each scenario have no big differences due to the scalability of the proposed system. The majority of positioning error distributions are less than 0.67 m, 0.73 m, 0.74 m, and 0.79 m for scenario 1, scenario 2, scenario 3, and scenario 4, respectively. This indicates that the proposed system is fault-tolerant and adapts to signal fluctuations. The errors are changed slowly in each scenario, since the ranges of estimated errors have no big differences.

The RMSEs of the proposed system have no big differences in various scenarios, since our hybrid approach could learn deeply the signal fluctuations and can resist AP faults easily. The RMSEs of the proposed method are 0.062, 0.063, 0.068, and 0.069 in meters at scenario 1, scenario 2, scenario 3, and scenario 4, respectively. This indicates that the proposed approach provides scalable and accurate positioning in each scenario.

5.2. Outdoor Positioning Results and Discussions. In this subsection, the proposed system performances in the outdoor environment are presented. We used similar scenarios to indoor positioning. The positioning is done in an open space, where the area is divided into 1 m^2 grids. Table 3 illustrates the positioning performances in different ranges of the outdoor environment. In each scenario, positioning accuracy has estimation errors less than 1.90 m. The maximum errors in scenario 1, scenario 2, and scenario 3 are 1.43 m, 1.53 m,

Table 3: Positioning accuracies of the SVM-DNN algorithm in different ranges.

Accuracy at different scenarios	Error boundaries (m) <0.9 m	<1 m	<1.5 m	Average errors (m)	RMSE
Scenario 1 (%)	62.5%	62.5%	100%	0.89	0.34
Scenario 2 (%)	50%	62.5%	87.5%	0.95	0.37
Scenario 3 (%)	37.5%	50%	87.5%	0.99	0.38
Scenario 4 (%)	50%	50%	75%	1.05	0.42

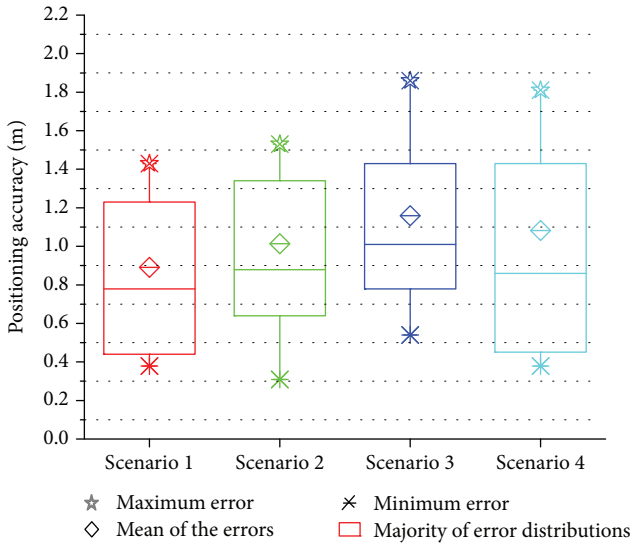

Figure 6: Outdoor positioning accuracies.

1.54 m, and 1.89 m, respectively. The result shows that the average errors have no big differences, since the proposed approach helps the machine to easily learn the signal fluctuations. The RMSEs also show the proposed approach providing motivating results. The observed signal from the outdoor environment is much fluctuated; however, the SVM-DNN learns easily to deliver the motivated results due to its deeper learning capacity. In each scenario, more than 50% of the estimation accuracy has less than 1 m positioning errors, and all testing errors in each scenario are less than 2 m. The mean errors in all scenarios are nearly similar. The RMSEs in different scenarios also give motivating results.

Figure 6 illustrates the positioning performances in terms of minimum error, maximum error, mean of errors, and boundary of positioning errors in each scenario. The majority of estimated errors are distributed in similar ranges, which implies that the proposed approach provides stable positioning services in the highly fluctuated Wi-Fi environments. The minimum errors are 0.38 m, 0.31 m, 0.48 m, and 0.38 m in scenario 1, scenario 2, scenario 3, and scenario 4, respectively. The maximum errors are 1.43 m, 1.53 m, 1.54 m, and 1.89 m in scenario 1, scenario 2, scenario 3, and scenario 4, respectively. The maximum errors did not always occur when more than one AP is missing.

Although there are few estimation variations in different testing points, the RMSE, the average of error values, and the majority of estimation distributions do not show big gaps in different scenarios. The results indicate that the positioning is continuous even when the trained APs are missed. The main reasons behind the accurate performances of the proposed system are an automatic updating of the missed APs through regression and the learning capability of the proposed system. Moreover, the application of LDA for feature reduction and the appended BSSIDs having the five strongest RSS values help the proposed algorithms achieve the best positioning accuracies. The application of LDA also enables to remove noise and other irrelevant information and makes the complex datasets simpler for the operation and improve accuracies. Additionally, collecting numbers of signal values from a 1 m-by-1 m grid helps the proposed system to adapt to the environment easily for accurate positioning.

The multi-kernel of SVM and backpropagation of DNN help to provide accurate positioning, since SVM can transpose larger datasets using its multi-kernels. Furthermore, DNN can easily update itself according to data natures and can control overfitting problems. It has also good positioning performance, since it is more suitable for pattern recognition problems. The SVM can distinguish data that is not linearly separable, and then DNN can easily locate the specific position of smartphone users. DNN is fully connected so that each node in one layer connects with the following nodes with a certain weight $w_{i,j}$, which allows DNN to learn superiorly.

The results in different ranges are motivated to apply the proposed approach for positioning services in various demanding areas. Principally, the integration of SVM and DNN makes positioning more accurate since positioning based on correctly classified values makes the system more robust [26]. DNN is more flexible with respect to accurate positioning in complex environments, and SVM helps in easily classifying hierarchical data distribution due to its multiple kernels. Although the computational time during the training stage is very high because of larger datasets and sets of integrated algorithms, the testing stage needs very small computational time and is relatively straightforward. The average computational time complexity of the proposed method using reduced datasets is 0.20 s. This means the testing time complexity is not affected due to missing the trained APs or other troubles, since the missed APs will be filled through FFNN before positioning. Our previous work [26] showed that LDA could possibly improve the computational time complexity. However, the scalability issue was not addressed.

Generally, the results show that the proposed technique can provide accurate and scalable indoor and outdoor positioning in complex, hierarchical, and dynamic environments. The results also indicate that the errors changed very calmly between consecutive testing points in both indoor and outdoor environments due to the superior robustness of SVM-DNN on uncertain, as well as complex, situations.

6. Conclusions

In this paper, the integrations of FFNN, LDA, SVM, and DNN algorithms are applied for indoor and outdoor

positioning. FFNN is used to develop a scalable system. LDA is applied to reduce the complex dimension of the scanned RSS values to lower features without affecting information contents. We use a hybrid of SVM-DNN to locate the target of smartphone users. We evaluate the proposed method in different scenarios at indoor and outdoor positioning schemes. The proposed approach provides 100% of the estimation accuracy with errors less than 0.97 m and 1.89 m during indoor and outdoor positioning, respectively. Additionally, our method implements with fewer average errors and variances. The error distributions of the majority of the results are similarly ranged in the same boundary, and error changes between consecutive testing points are slow. The computational time complexities are also small in each scenario in both indoor and outdoor positioning schemes. Thus, the integration of IoT gives the state-of-the-art performance on indoor and outdoor positioning in hierarchical, dynamic, and complex environments. The application of DNN for indoor and outdoor localization using an unmanned aerial vehicle (UAV) in urban and suburban areas is our potential future work.

Data Availability

The data used to support the findings of this study are available from the corresponding author upon request.

Conflicts of Interest

The authors declare no conflict of interest.

Acknowledgments

This research is funded by the Ministry of Science and Technology (MoST) in Taiwan (Grant No.: 107-2634-F-009-006).

References

[1] J. Liu, *Survey of Wireless Based Indoor Localization Technologies*, Department of Science & Engineering, Washington University, 2014.

[2] O. Chakroun, M. Hild, and B. Abdulrazak, *Indoor and Outdoor Localization Framework for Pervasive Environments*, Ambient Systems, Networks and Technologies (ANT), 2010.

[3] M. V. Moreno-Cano, M. A. Zamora-Izquierdo, J. Santa, and A. F. Skarmeta, "An indoor localization system based on artificial neural networks and particle filters applied to intelligent buildings," *Neurocomputing*, vol. 122, pp. 116–125, 2013.

[4] D. Macagnano, G. Destino, and G. Abreu, "Indoor positioning: a key enabling technology for IoT applications," in *2014 IEEE World Forum on Internet of Things (WF-IoT)*, pp. 117-118, Seoul, South Korea, 2014.

[5] K. Lin, M. Chen, J. Deng, M. M. Hassan, and G. Fortino, "Enhanced fingerprinting and trajectory prediction for IoT localization in smart buildings," *IEEE Transactions on Automation Science and Engineering*, vol. 13, no. 3, pp. 1294–1307, 2016.

[6] W. H. Kuo, Y. S. Chen, K. T. Cheng, and T. W. Lu, "Signal strength based indoor and outdoor localization scheme in zigbee sensor networks," *IAENG International Journal of Computer Science*, vol. 23, no. 1, pp. 55–64, 2016.

[7] A. Yassin, Y. Nasser, M. Awad et al., "Recent advances in indoor localization: a survey on theoretical approaches and applications," *IEEE Communications Surveys & Tutorials*, vol. 19, no. 2, pp. 1327–1346, 2017.

[8] A. A. Khudhair, S. Q. Jabbar, M. Qasim Sulttan, and D. Wang, "Wireless indoor localization systems and techniques: survey and comparative study," *Indonesian Journal of Electrical Engineering and Computer Science*, vol. 3, no. 2, p. 392, 2016.

[9] Y. K. Cheng, H. J. Chou, and R. Y. Chang, "Machine-learning indoor localization with access point selection and signal strength reconstruction," in *2006 IEEE 83rd Vehicular Technology Conference (VTC Spring)*, pp. 1–5, Nanjing, China, 2016.

[10] A. Paul and T. Sato, "Localization in wireless sensor networks: a survey on algorithms, measurement techniques, applications and challenges," *Journal of Sensor and Actuator Networks*, vol. 6, no. 4, p. 24, 2017.

[11] A. Paul and T. Sato, "Detour path angular information based range-free localization in wireless sensor network," *Journal of Sensor and Actuator Networks*, vol. 2, no. 1, pp. 25–45, 2013.

[12] K. S. Kim, R. Wang, Z. Zhong et al., "Large-scale location-aware services in access: hierarchical building/floor classification and location estimation using Wi-Fi fingerprinting based on deep neural networks," *Fiber and Integrated Optics*, vol. 37, no. 5, pp. 277–289, 2018.

[13] S. Petr, S. Martin, and K. Dominik, "An overview of indoor and outdoor positioning technologies with focus on their precision," *Electrorevue*, vol. 18, no. 6, pp. 183–192, 2016.

[14] T. Halonen, J. Romero, and J. Melero, Eds., *GSM, GPRS, and EDGE Performance: Evolution towards 3G/UMTS*, John Wiley & Sons, 2004.

[15] S. Treuillet and E. Royer, "Outdoor/indoor vision-based localization for blind pedestrian navigation assistance," *International Journal of Image and Graphics*, vol. 10, no. 4, pp. 481–496, 2010.

[16] S. Xia, Y. Liu, G. Yuan, M. Zhu, and Z. Wang, "Indoor fingerprint positioning based on Wi-Fi: an overview," *ISPRS International Journal of Geo-Information*, vol. 6, no. 5, p. 135, 2017.

[17] M. Nowicki and J. Wietrzykowski, "Low-effort place recognition with WiFi fingerprints using deep learning," in *Automation 2017. ICA 2017*, pp. 575–584, Springer, Cham, Switzerland, 2017.

[18] C. S. Chen, "Artificial neural network for location estimation in wireless communication systems," *Sensors*, vol. 12, no. 3, pp. 2798–2817, 2012.

[19] M. Farhat, M. Ibrahim, and I. Nesreen, "Effects of walls and floors in indoor localization using tracking algorithm," *International Journal of Advanced Computer Science and Applications*, vol. 7, no. 3, 2016.

[20] S. Ezpeleta, J. Claver, J. Pérez-Solano, and J. Martí, "Rf-based location using interpolation functions to reduce fingerprint mapping," *Sensors*, vol. 15, no. 10, pp. 27322–27340, 2015.

[21] A. Belay, L. Yen, S. Renu, H. P. Lin, and S. S. Jeng, "Indoor localization at 5GHz using dynamic machine learning approach (DMLA)," in *International Conference on Applied System Innovation (ICASI)*, pp. 1763–1766, Sapporo, Japan, 2017.

[22] L. Yen, C.-H. Yan, S. Renu, A. Belay, H.-P. Lin, and Y.-S. Ye, "A modified WKNN indoor Wi-Fi localization method with

differential coordinates," in *2017 International Conference on Applied System Innovation (ICASI)*, pp. 1822–1824, Sapporo, Japan, 2017.

[23] A. B. Adege, Y. Yayeh, G. Berie, H.-p. Lin, L. Yen, and Y. R. Li, "Indoor localization using K-nearest neighbor and artificial neural network back propagation algorithms," in *2018 27th Wireless and Optical Communication Conference (WOCC)*, pp. 1-2, Hualien, Taiwan, 2018.

[24] Y. Liu and Q. Chen, "Research on integration of indoor and outdoor positioning in professional athletic training," *Proceedings*, vol. 2, no. 6, p. 295, 2018.

[25] L. Reyero and G. Delisle, "A pervasive indoor-outdoor positioning system," *Journal of Networks*, vol. 3, no. 8, 2008.

[26] A. Adege, H.-P. Lin, G. Tarekegn, and S.-S. Jeng, "Applying deep neural network (DNN) for robust indoor localization in multi-building environment," *Applied Sciences*, vol. 8, no. 7, p. 1062, 2018.

[27] I. Goodfellow, Y. Bengio, A. Courville, and Y. Bengio, *Deep Learning*, MIT Press, Cambridge, MA, USA, 1st edition, 2016.

[28] G. Félix, M. Siller, and E. N. Alvarez, "A fingerprinting indoor localization algorithm based deep learning," in *2016 Eighth International Conference on Ubiquitous and Future Networks (ICUFN)*, pp. 1006–1011, Vienna, Austria, 2016.

[29] W. Zhang, K. Liu, W. Zhang, Y. Zhang, and J. Gu, "Deep neural networks for wireless localization in indoor and outdoor environments," *Neurocomputing*, vol. 194, pp. 279–287, 2016.

[30] X. Wang, L. Gao, S. Mao, and S. Pandey, "DeepFi: deep learning for indoor fingerprinting using channel state information," in *2015 IEEE Wireless Communications and Networking Conference (WCNC)*, pp. 1666–1671, New Orleans, LA, USA, 2015.

[31] X. Wang, L. Gao, S. Mao, and S. Pandey, "CSI-based fingerprinting for indoor localization: a deep learning approach," *IEEE Transactions on Vehicular Technology*, vol. 66, no. 1, pp. 763–776, 2017.

[32] K. S. Kim, S. Lee, and K. Huang, "A scalable deep neural network architecture for multi-building and multi-floor indoor localization based on Wi-Fi fingerprinting," *Big Data Analytics*, vol. 3, no. 1, 2018.

[33] A. Moreira, M. J. Nicolau, F. Meneses, and A. Costa, "Wi-Fi fingerprinting in the real world - RTLS@UM at the EvAAL competition," in *2015 International Conference on Indoor Positioning and Indoor Navigation (IPIN)*, pp. 1–10, Banff, AB, Canada, 2015.

[34] D. L. Tapia, J. Bajo, J. F. De Paz, R. S. Alonso, S. Rodríguez, and J. M. Corchado, "Using multi-layer perceptrons to enhance the performance of indoor rtls," in *Proceedings of the Progress in Artificial Intelligence in 15th Portuguese Conference on Artificial Intelligence: EPIA*, pp. 31–39, Lisbon, Portugal, 2011.

[35] U. Ahmad, A. Gavrilov, S. Lee, and Y. K. Lee, "Modular multilayer perceptron for WLAN based localization," in *The 2006 IEEE International Joint Conference on Neural Network Proceedings*, pp. 3465–3471, Vancouver, BC, Canada, 2006.

[36] M. Dakkak, B. Daachi, A. Nakib, and P. Siarry, "Multi-layer perceptron neural network and nearest neighbor approaches for indoor localization," in *2014 IEEE International Conference on Systems, Man, and Cybernetics (SMC)*, pp. 1366–1373, San Diego, CA, USA, 2014.

[37] K. Lingemann, H. Surmann, A. Nuchter, and J. Hertzberg, "Indoor and outdoor localization for fast mobile robots," in *2004 IEEE/RSJ International Conference on Intelligent Robots and Systems (IROS) (IEEE Cat. No.04CH37566)*, pp. 2185–2190, Sendai, Japan, 2004.

[38] Y. Tifani, B. Lee, and E. Jeong, "A patient's indoor positioning algorithm using artificial neural network and SVM," *Journal of Theoretical & Applied Information Technology*, vol. 95, no. 16, 2017.

[39] G. Deak, K. Curran, J. Condell, D. Deak, and P. Kiedrowski, "Support vector machine and probability neural networks in a device-free passive localization (DFPL) scenario," *Image Processing & Communications*, vol. 17, no. 4, pp. 9–16, 2012.

[40] H. Mehmood, N. K. Tripathi, and T. Tipdecho, "Indoor positioning system using artificial neural network," *Journal of Computer Science*, vol. 6, no. 10, pp. 1219–1225, 2010.

[41] P. Lopez-de-Teruel, O. Canovas, and F. J. Garcia, "Using dimensionality reduction techniques for refining passive indoor positioning systems based on radio fingerprinting," *Sensors*, vol. 17, no. 4, 2017.

[42] S. Jeon, J. P. Jeong, Y. J. Suh, C. Yu, and D. Han, "Selective AP probing for indoor positioning in a large and AP-dense environment," *Journal of Network and Computer Applications*, vol. 99, pp. 47–57, 2017.

[43] Z. A. Deng, Y. Xu, and L. Chen, "Localized local fisher discriminant analysis for indoor positioning in wireless local area network," in *2013 IEEE Wireless Communications and Networking Conference (WCNC)*, pp. 4795–4799, Shanghai, China, 2013.

[44] E. Alpaydin, *Introduction to Machine Learning*, The MIT Press, Cambridge, Massachusetts, London, England, 2nd edition, 2014.

[45] C. Laoudias, M. P. Michaelides, and C. G. Panayiotou, "Fault detection and mitigation in WLAN RSS fingerprint-based positioning," *Journal of Location Based Services*, vol. 6, no. 2, pp. 101–116, 2012.

Hindawi
Journal of Sensors
Volume 2018, Article ID 7102069, 9 pages
https://doi.org/10.1155/2018/7102069

Research Article

Scalable Deposition of Nanomaterial-Based Temperature Sensors for Transparent and Pervasive Electronics

Andreas Albrecht[1], **Almudena Rivadeneyra**[1], **Marco Bobinger**[1], **Jacopo Bonaccini Calia**[1], **Florin C. Loghin**[1], **Jose F. Salmeron**[1], **Markus Becherer**[1], **Paolo Lugli**[2] and **Aniello Falco**[2]

[1]*Institute for Nanoelectronics, Technical University of Munich, Munich, Germany*
[2]*Faculty of Science and Technology, Free University of Bolzano, 39100 Bolzano-Bozen, Italy*

Correspondence should be addressed to Almudena Rivadeneyra; arivadeneyra@ugr.es

Received 11 April 2018; Revised 8 August 2018; Accepted 16 August 2018; Published 31 October 2018

Academic Editor: Sang Sub Kim

This work presents a comparative analysis of materials for planar semitransparent thermocouples fabricated by spray deposition on a flexible substrate. Three different materials are employed to build such devices, analyzing also the effect of the spray order in their final performance. The highest Seebeck coefficient (50.4 μV/K) is found for a junction made of carbon nanotubes (CNTs) on top of silver nanowires (AgNWs) whereas its efficiency in terms of power is the lowest because of the higher sheet resistance of the CNTs. In this case, the best combination for energy-harvesting purposes would be poly (3,4-ethylenedioxythiophene) polystyrene sulfonate (PEDOT:PSS) and AgNWs, with a power factor of 219 fW/K^2. These results prove the feasibility of developing large-scale and cost-effective thermocouples that could be used for sensing or energy-harvesting applications.

1. Introduction

Thermoelectric (TE) phenomena have been investigated and employed extensively for more than a century, as they relate two fundamental quantities: electricity and thermal transmission. Among the many TE effects which have been studied and exploited, the two which received a broader attention are the Peltier and Seebeck effects, respectively. These two can be seen as counterparts, since the former explains a temperature gradient due to electrical current flow through dissimilar materials while Seebeck is mainly the potential difference due to a temperature gradient [1].

The latter can be employed for the realization of "thermocouples," ideally defined as the series of two lines of different materials, which generate voltages with opposite signs upon the application of a thermal gradient. By applying a temperature gradient between the junction of the two materials and their extremities, it is possible to measure a potential difference between the single ends, which will be the sum of the voltages generated by each "leg" [2]. A first order mathematical expression of the Seebeck effect for each line is the following:

$$\Delta V = \alpha_S \Delta T, \tag{1}$$

with α_S being the material-dependent Seebeck coefficient sometimes also referred to as simple "S."

Since (1) shows a linear dependency between temperature change and resulting voltage, this effect is a well-suited indicator for temperature measurement or energy-harvesting applications. For many material combinations, this relationship is linear, leading to an easy-to-read temperature sensor. In addition to this, a steep curve is preferred, as it represents a thermocouple more sensitive to temperature changes and allows a higher possible resolution. Remarkably, the insurgence of a voltage difference can also be employed to drive an electric load or to charge up an energy accumulator. The usage of TCs for thermal energy-harvesting applications has been driven by materials with very high thermoelectric power, such as bismuth

telluride (Bi_2Te_3) [3]. The ability to convert thermal energy in electricity can be effectively summarized by the dimensionless figure of merit (FoM) ZT, defined as

$$ZT = \alpha_S^2 \sigma \frac{T}{K}, \quad (2)$$

where σ is the electrical conductivity and K is the thermal conductivity [4].

Together with α_S, these transport parameters are intertwined and are affected by other intrinsic properties of the material, such as carrier concentration and band structure [4]. The FoM also gives clear indications of how more efficient thermocouples can be obtained by either maximizing α_S and σ or minimizing K.

Nevertheless, these strictly thermoelectrical parameters alone do not suffice to define next generation thermocouples. In fact, the research in the field of the Internet of Things and wearable electronics has been leaning towards the realization of flexible or conformal devices [5], seamlessly integrated in the environment [6], objects [7], or even the human body [8]. Furthermore, conventional thermocouples are built of different metals, metal alloys, or doped semiconductors, which present high ZT values as well as high environmental impact. The deposition of pure metals and inorganic semiconductors is extremely energy intensive [9] and difficult to recycle. One approach towards the substitution of such materials is the realization of novel devices, based on polymers or nanostructured materials. Albeit, at the current state, nanomaterials present lower FoM; they still have a wide margin of improvement, and they possess a number of uncommon qualities, which are not to be found in conventional thermoelectric materials. Nanomaterials are potentially low cost [10], can be obtained through nontoxic production processes [9], can be semitransparent [11], and can be easily processed into various shapes [12, 13] on arbitrary substrates [14, 15].

For instance, it is possible to increase the ZT values of insulating or semiconducting polymers, through the simple addition of one-dimensional fiber structures, such as carbon nanotubes (CNTs) or conducting nanowires. A composite of polymer and fiber would preserve the low thermal conductivity of a polymer, while it would present an enhanced conductivity, due to the low electrical resistivity of the fiber structure, after reaching a percolation threshold [16]. An interesting example for this class of solutions is the work of Yu et al., in which they demonstrated a great increase of the FoM through adding CNTs into polymer [17].

In a similar direction, the employment of conductive nanomaterials (e.g., silver nanowires (AgNWs) [18], poly (3,4-ethylenedioxythiophene) polystyrene sulfonate (PEDOT:PSS) [19], and CNTs [20]) can improve the performance of the TCs because of very low heat capacity accompanied by Seebeck coefficients of circa 40 μV/°C [21, 22]. As previously stated, the interest in this class of materials is also due to their potential (semi)transparency. Nanotubes, nanowires, and polymers have been previously employed in many applications, which require a semitransparent conductive layer, such as organic photodiodes [23, 24], solar cells [25], organic light-emitting diodes [26], and transparent heaters [27] as well as power-harvesting applications [28–30].

In this work, we exploit all the remarkable properties of solution processable nanomaterials such as scalability and roll-to-roll (R2R) processability at ambient conditions to fabricate novel kinds of semitransparent thermocouples by means of spray deposition. Because of the inherit flexibility of this deposition technique, the novel devices we propose can be integrated straightforwardly and seamlessly onto any transparent surface, enabling the fabrication of semitransparent differential temperature sensors for smart homes and integrated cars or even for the smart lenses of the future.

2. Materials and Methods

2.1. Materials. For the fabrication of the TC, we tested different combinations of materials, in particular, a custom-made solution of PEDOT:PSS (Clevios PH1000) with 1 g of polymer diluted in 4 g of deionized (DI) water, 10 mg of Dynol 604 (Sigma-Aldrich), and 250 mg of Ethylene glycol (EG), which is employed to increase their conductivity [31]. Before adding PEDOT:PSS, the material was filtered with a pore-size filter of 0.45 μm. The solution was always sonicated for 30 s to disperse agglomerates before spray deposition. For AgNWs, we diluted 1 g of AgNW (ECD0X3from Ras Materials) with 14 g isopropyl alcohol and 5 g deionized (DI) water. The mixture thus produced, the solution was always shaken before using it.

The CNTs that we have used are commercially available from Sigma-Aldrich (Product number: 773735). The CNT ink consists of DI water, 90% semiconducting single-walled CNTs (SWCNTs), and sodium dodecyl sulfate (SDS, Sigma-Aldrich), which acts as dispersing agent. The base solution was made by dissolving 1 wt % SDS in DI water. 0.03 wt % of CNTs were added to the solution and treated with a horn sonicator (Branson Sonifier S-450D) for 25 min at a power of 50%. The solution was then centrifuged at 15 krpm for 90 min and the top 80% of the supernatant separated, to be used as the CNT ink [32].

2.2. Fabrication Process. To manufacture the TCs, the inks were sprayed through a shadow mask onto a 75 μm thick Kapton HN foil with an area of $50 \times 50\,mm^2$. We selected the polyimide film because of its high thermal stability to avoid influences of the substrate or its destruction during the measurement. In accordance with the process parameters that we previously tailored for the deposition of AgNWs and CNTs [27, 33], the materials were sprayed to conductive films using a fully automated spray robot PVA350 from Werner Wirth (Germany) equipped with a 781S General Purpose spray valve from Nordson (USA) [18]. Every layer was deposited via mesh-like motion, as shown in Figure 1. The nozzle movement had a speed of 250 mm/s, and the nozzle-to-sample distance was set to 50 mm; the mesh line distance was set to 3 mm. All samples were sprayed with a material pressure of 0.02 MPa and an atomizing pressure of 0.05 MPa. The orifice opening of the nozzle can be manually decreased with a valve (nozzle orifice opening value). The maximum diameter of the nozzle orifice is 0.3 mm. The

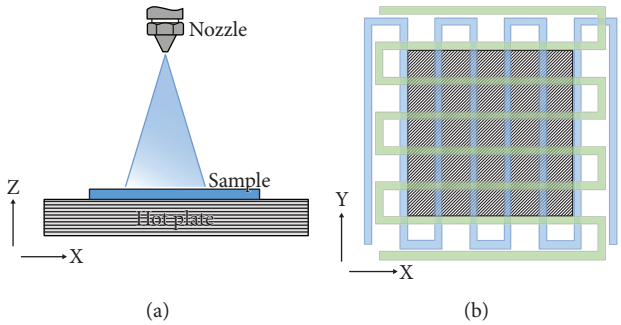

Figure 1: (a) Schematic of the spray setup. (b) Schematic of the trajectory of the gun over the sample while spraying: one deposited layer consists of spraying the sample in line form on x- and on y-direction. The gun remains at the same distance of the sample during the whole process.

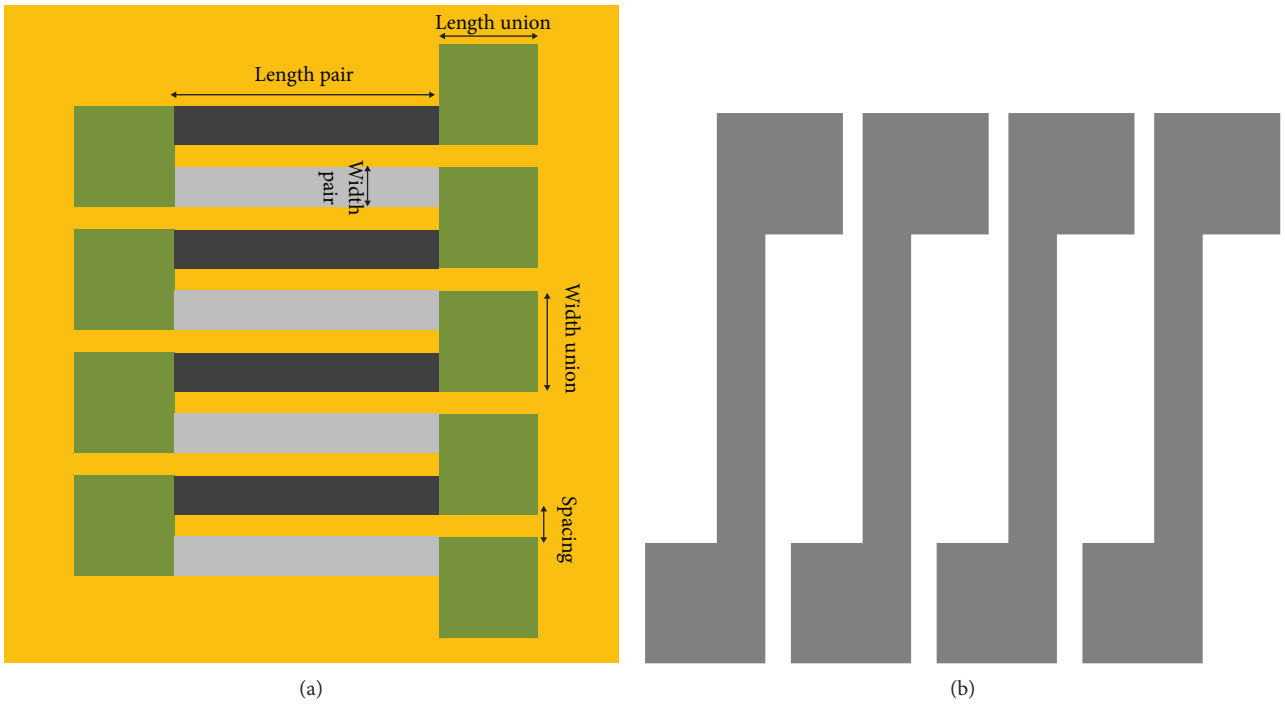

Figure 2: (a) Dimensions of one TC device containing four TC. The TC legs are all identical, 2.5 mm width and 27.5 mm length. The different colors in the drawing are indicating the different materials: in dark grey the material sprayed first, in light grey the material sprayed seconds, in green the contacts, which were made by the overlapping of both sprayed materials, and in yellowish color the substrate. (b) Layout of the laser-cut mask needed to spray the four TC structures. Two such masks are needed to produce one TC. The first mask is oriented as in the picture. The second mask is the same, rotated by 180°, to be placed superimposing the mask ends in alternate manner. This creates the pattern shown in (a).

spraying nozzle was changed when spraying with CNT or AgNW/PEDOT:PSS, with its appropriate gun number, which is written manually on its metal frame. The temperature of the hot plate was also varied when spraying the different materials. In particular, the temperature was set to 65°C for AgNWs, 90°C for PEDOT:PSS, and 80°C for SWCNTs. The spray deposition of a solution implies to be in a wet spraying regime.

To speed up the drying of the wet droplets arriving at the substrate, the substrates were left lying on the hot plate. This approach allows the formation of dry layers with good thickness control over time, enhancing at the same time reproducibility [32].

Four TCs are fabricated in series (see Figure 2(a)), fixing the substrate and the shadow mask (see Figure 2(b)) via small magnets (diameter of 1 mm) on the hot plate of the spray machine. Ten layers of each material were spray deposited, each having its own mask.

2.3. Characterization. The transmittance spectra were measured from 350 nm to 800 nm using the light from a 300 W Xenon arc lamp from Newport Oriel chopped at 210 Hz, which passes through an Oriel Cornerstone 260 ¼ monochromator and illuminates a calibrated photodiode with a transconductance amplifier connected to an Oriel Merlin digital lock-in amplifier.

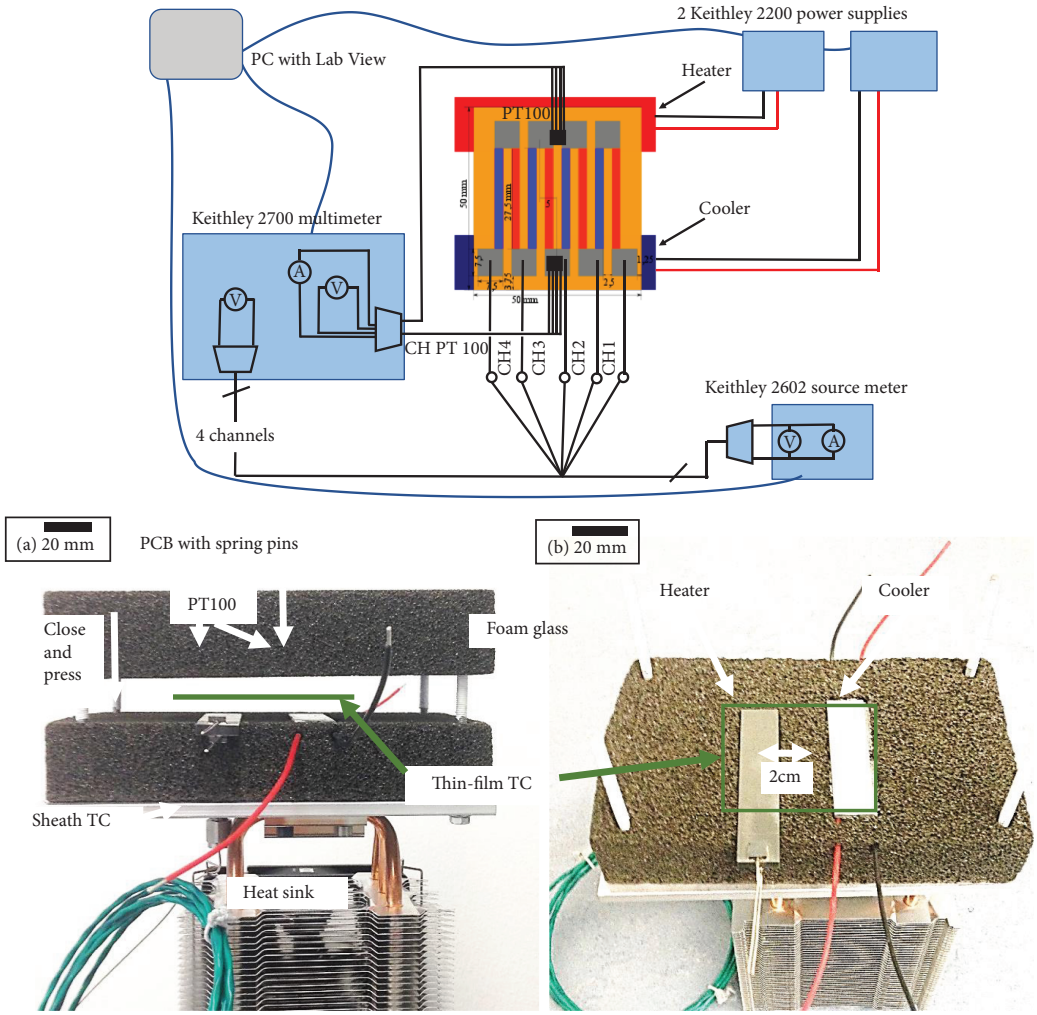

Figure 3: Custom-made setup for the thermoelectrical characterization of the device schematic on the top part, real picture on the bottom. The position of the TC under test is marked in green from (a) side view with lifted top cover and (b) top view without top cover. Reprocessed from original files published in [35].

To quantify the performance of a transparent conducting material, the ratio between the transmission at 550 nm (T^{10}) and the sheet resistance of the film (R_s) is taken. The formula in (3) gives a FoM on conductive films [34].

$$\text{FoM} = \frac{T^{10}}{R_S}. \tag{3}$$

Sheet resistance was measured at room temperature using a four-point probe head from Jandel connected to a Keysight B2901A source measuring unit.

In order to determine the exact thickness of the film, a tactile profilometer measurement is performed with the Bruker's DektakXT device.

A field-emission scanning electron microscope (FESEM) is used for the surface imaging. Therefore, it scans over the surface of the sample with an electron beam exposed to voltages between 1 kV and 30 kV.

Infrared images were recorded using a high-resolution calibrated thermal imaging camera (Testo 890, 640 × 480 pixels), which employs bolometric detectors and has a spectral sensitivity window of 7.5–14 μm. The emissivity of the thin films was determined by adjusting the temperature measured by the camera to match the temperature on the heated side, which was measured employing a PT100 thermoresistance.

A custom-built setup was designed to characterize the flexible transparent TCs. The setup consists of a flat ceramic heater and a Peltier cooler embedded into a low-heat-conductive isolating foam glass. The setup is illustrated in Figure 3. The TCs are placed on top of the heater and cooler and pressed down by the top foam glass and a weight. The temperatures at the surface of the TCs are measured by thermoresistors (PT100 from Heraeus M422) mounted at the hot and cold side. Two single-channel programmable power supplies (Keithley 2200) control the heater and cooler. The voltages generated by the TCs are measured by a Keithley 2700 multimeter at an input impedance of 1 MΩ. For all measurements, the temperature was ramped from 27°C to 107°C, corresponding to a maximum temperature difference of 80°C. The setup is automated by LabView 2016.

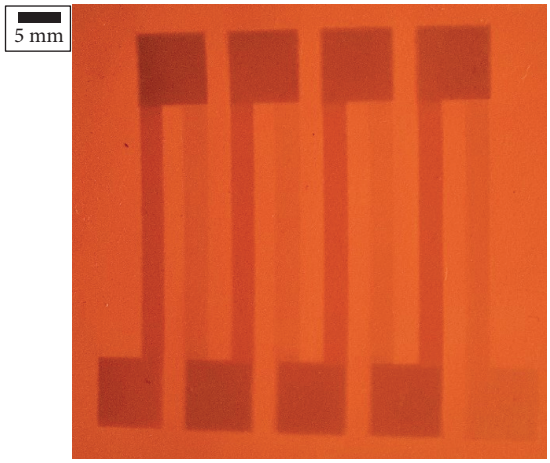

Figure 4: Picture of thermocouples made of PEDOT:PSS (dark grey) sprayed on top of AgNW (light grey). AgNWs form a milky-white or silver layer and the blue/grey PEDOT:PSS layer overlaps at the contact regions. The hot area is on the right side and the cold area is on the left side similar to the schematic.

Infrared (IR) images for the thermocouple setup with the heater at a temperature of 300°C are included in the supporting information in Figure S1. Due to the excellent thermal insulation of the foam glass, the generated heat is confined to the heater area. This confinement gives rise to an increase in the temperature gradient and, hence, also an increase in the Seebeck coefficients.

3. Results and Discussion

3.1. Physical Characterization. Figure 4 presents a photograph of a manufactured series of four thermocouples made with PEDOT:PSS sprayed on top of AgNWs. The blueish color of PEDOT:PSS appears dark whereas the AgNW is less pronounced. The definition of the patterns is reproducible, and the error in the alignment is almost negligible (less than 1 mm in the worst case) in comparison with the junction area.

Thickness was measured against a reference level, the glass substrate itself, obtained by scratching with a thin scalpel a straight line on the film and using the scratch bottom as reference value for the zero-height value. The average thicknesses of the sprayed layers for all nanomaterials were below 300 nm, corresponding to very little material usage. Thickness measurements are not well suited for nanowire and nanotube networks as they possess a low density and only peaks are visible. Scanning electron microscopy (SEM) is more suitable to evaluate the uniformity of the spray deposition. SEM was used to image different parts of the sample and verify the complete coverage of the sample. Figure 5 shows illustrative images for each material, emphasising the different sizes of the nanostructures: AgNWs are up to tens of micron long and very stiff; CNTs are shorter than one micron, with a flexible and easy to adapt shape, while PEDOT:PSS constitutes a uniform soft layer.

3.2. Optical Characterization. The transmittance over the visible spectrum (350 nm to 750 nm) are shown in Figure 6(a). Here, we see similar transmittance values for CNT and AgNWs, which become more transparent for longer wavelengths. PEDOT:PSS shows the lowest transmittance, and it is characterized by a strong absorption in the red part of the spectrum. As per previous protocols defined in literature, the transmittance value in the maximum sensitivity of the human eye in the green range (550 nm) of the spectrum is considered as reference transmittance, indicating transmittance values of 87%, 90%, and 78% for AgNWs, CNTs, and PEDOT:PSS, respectively. Figure 6(b) illustrates the decrease in the transmittance with the increase in the number of spray-deposited layers. As the purpose of this work is to achieve semitransparent thermocouples, we have to look for a trade-off between sheet resistance and transmittance for each material. Both transmittance and sheet resistance vary according to the thickness. The thicker the layers are, the lower the sheet-resistance result and the lower the transmittances obtained. Therefore, in order to not lose transmittance, the number of layer used to fabricate the thermocouples was set to 10.

3.3. Electrical Characterization. The resistivity of AgNW, PEDOT:PSS, and CNT deposited film is presented in Table 1. Due to the very high resistivity of CNT compared to the other two films, the resistivity of a full TC is determined by the CNT, when this is part of it.

The measured sheet resistance of 10-layer single material thin films is also included in Table 1, showing how this parameter for PEDOT:PSS is two orders of magnitude lower than CNTs and one higher than AgNWs. Combining these numerical value, it is easy to estimate the FoM, equal to 45, 0.56, and 0.003 for AgNWs, PEDOT:PSS, and CNTs, respectively.

3.4. Thermoelectric Characterization. The measurement of the open-circuit voltage (Figure 7) gave a clearly linear relationship ($R^2 > 0.995$) to temperature difference between hot and cold junction, for the temperature range used in the tests. As such, the Seebeck coefficient has been estimated as the slope of the curve, neglecting any second-order effect. The transparent TCs presented Seebeck coefficients of $50.4 \pm 5.68\,\mu$V/K, $26.9 \pm 2.87\,\mu$V/K, and $14.8 \pm 0.83\,\mu$V/K for AgNWs-CNTs, CNTs-PEDOT, and AgNWs-PEDOT, respectively. These results are in line with previous literature for nontransparent nanomaterial-based thermocouples and, hence, represent a significant advancement towards the obtainment of transparent electronics. Nevertheless, not only the value is different among different material couples but also the same material couple, when sprayed in a different order results in different thermovoltages. This is particularly true for TC, in which one of the two materials is CNTs. For instance, when AgNWs are sprayed on top of CNTs, the Seebeck coefficient of the TC exhibits a drop of nearly 30%, with respect to the reverse spraying order. An opposite to this phenomenon can be appreciated for the combination PEDOT:PSS and CNTs, in which the TCs with a CNT bottom layer outperform the dual

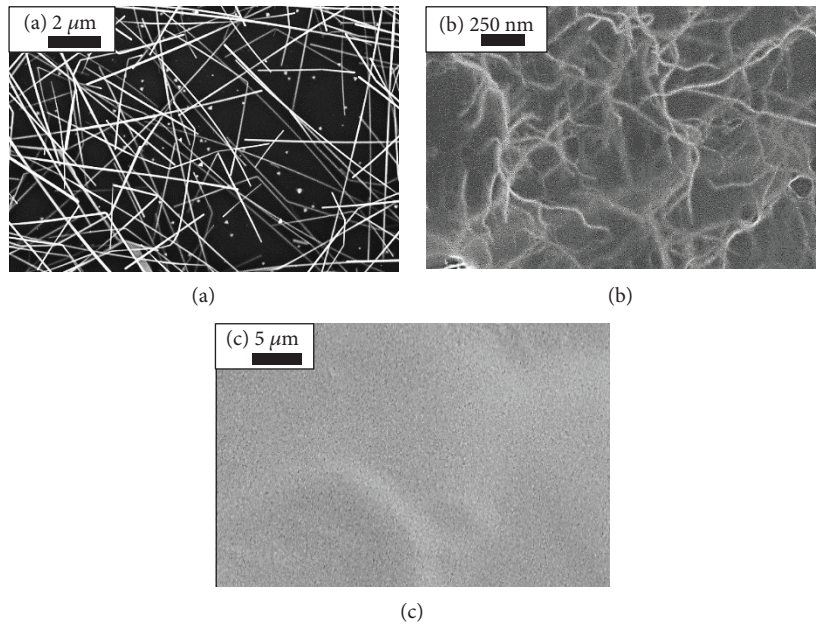

Figure 5: FESEM pictures of (a) AgNWs, (b) CNTs, and (c) PEDOT:PSS spray-deposited films.

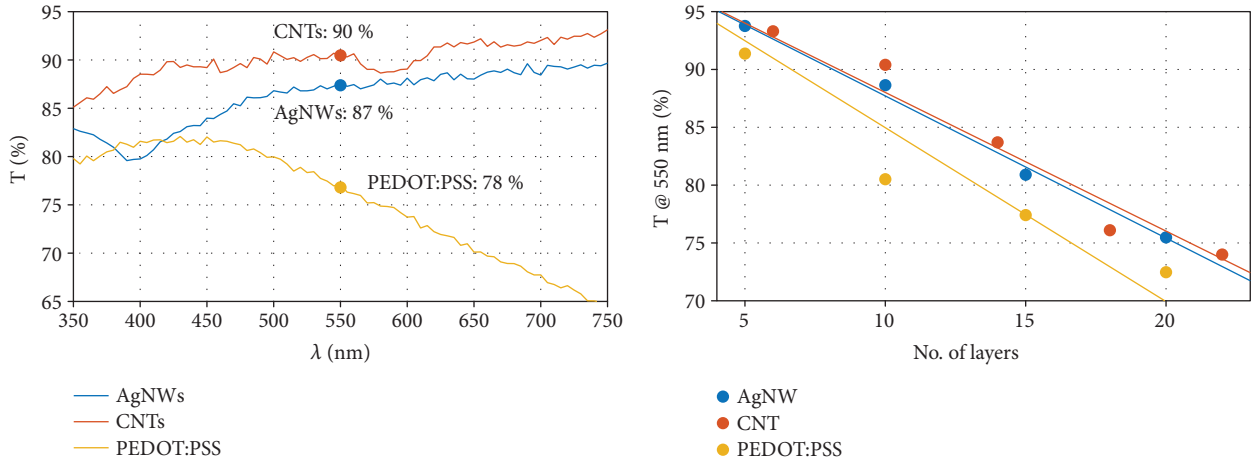

Figure 6: Transmittance of reference films for the materials used. CNT and AgNW have similar transparency. PEDOT transparency decreases at increasing wavelengths.

Table 1: Electrical and optical properties of single material thin-film.

Material	T (%) at 550 nm	R_S [Ω/sq.]	FoM (%)
AgNW	85	52	45
PEDOT:PSS	76	100	0.650
CNT	89	$3.4 \cdot 10^4$	0.003

combination. The reasons behind the two behaviours are most likely related to a better electrochemical interface in the most performing combination, due to the sequence of process steps. In the former case, i.e., CNTs on AgNWs, the appropriate interface is guaranteed by the ductility and conformability of the CNTs, which can well entangle the AgNWs. Vice versa, the stiff AgNWs would not be able to conform to the rough surface of the CNTs, leading to poor electrical contact. In the latter case, i.e., PEDOT:PSS on CNTs, the motivation can be found in the solubility of PEDOT:PSS in water. After the deposition of CNTs on top of the polymeric layer, they need to be placed in a water bath to remove the dispersing matrix. By doing so, the CNTs become conductive, while part of the PEDOT:PSS is delaminated because of the contact with water. Finally, in the case of PEDOT:PSS and AgNW thermocouples, there is no difference in the deposition order, although this TC combination presents the lowest V_{OC} (about 15.5 μV/K).

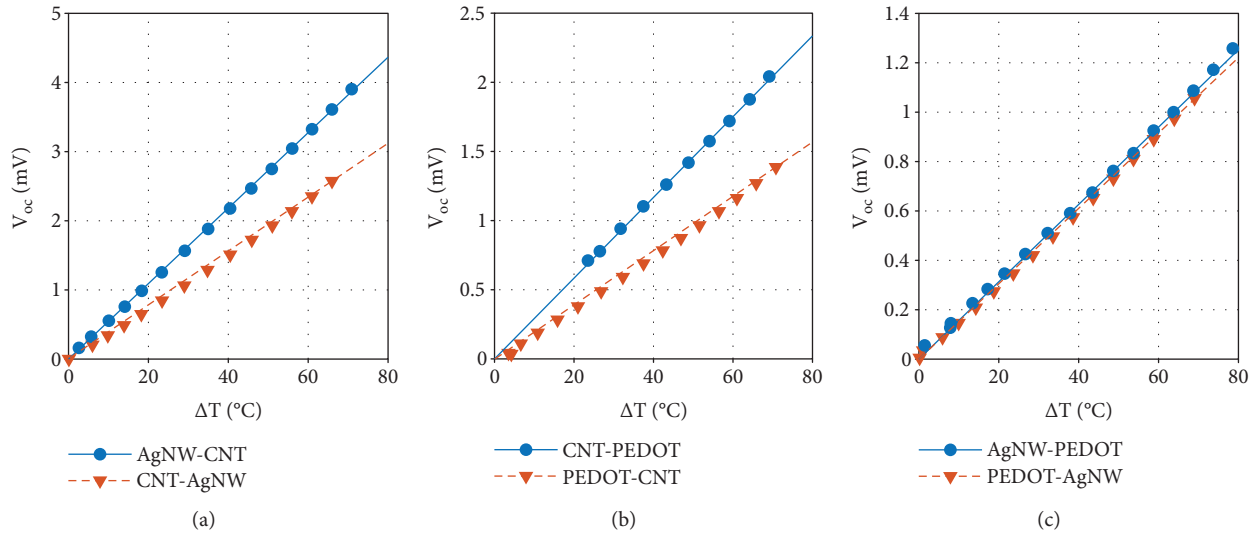

Figure 7: Linearity of open-circuit voltage over the temperature difference for thermocouple pairs made with (a) AgNW-CNTs, (b) CNTs-PEDOT:PSS, and (c) AgNW-PEDOT:PSS. The order of mentioning in the legend indicates the spraying order with the second material sprayed after the first one.

Table 2: Series Seebeck coefficient of the four legs of the TCs in μV/K for the three material combinations and the two spraying orders and the mean value of the individual junctions ($\bar{S}_i$). The material mentioned first was sprayed first. The resistance and the resulting power over the four thermocouples are also displayed.

Type	AgNW-CNT	CNT-AgNW	CNT-PEDOT:PSS	PEDOT:PSS-CNT	AgNW-PEDOT:PSS	PEDOT:PSS-AgNW
$\bar{S}_i$ (μV/K)	50.4 ± 5.68	37.5 ± 1.40	26.9 ± 2.87	13.8 ± 5.51	14.8 ± 0.83	14.3 ± 0.64
S_{series} (μV/K)	201.7	149.9	107.4	55.1	58.9	57.2
R_{series} (kΩ)	92.2	90.2	179	222	5.38	3.73
PF_{series} (fW/K^2)	110	62.3	16.1	3.42	161	219

Table 2 presents the average voltage $\bar{S}_i$. The spraying order is indicated in each column, mentioning first the material deposited as bottom layer. We also analyzed the potential of these thermocouples as energy harvesters. For this purpose, we measured resistance values of the series of four thermocouples (also included in Table 2). PEDOT:PSS in combination with AgNWs shows lower resistance. Actually, the higher values obtained by the other TCs are associated to the high sheet-resistance value of the sprayed CNTs. The power factor was estimated as the square of the half of the Seebeck coefficient divided by the resistance (4). These values are included in Table 2. Errors have been calculated as the standard deviation.

$$PF_{series} = \frac{(S_{series}/2)^2}{R_{series}} = \frac{1}{4}\frac{S_{series}^2}{R_{series}}. \quad (4)$$

It can be seen that the lower output power values are found in those thermocouples with CNTs. This very low values are caused by the high resistance of CNT layers (sheet resistance in the order of tens of kΩ/sq). In contrast with this, the higher output power is achieved by the AgNWs-PEDOT:PSS combination where the sheet resistance is in all cases below 100 Ω/sq.

Table 3 summarizes the Seebeck coefficients obtained in other planar thermocouples reported in literature. As the combination of materials is similar, the Seebeck coefficients do not vary significantly; they are, however, manufactured with high-throughput, large area methods. Albeit remarkable, this result, by itself, does not allow the employability of these printed TCs as energy harvesters because of the high leg-resistance.

In order to enhance the performance of the CNT-based thermocouples as thermal harvesters, a drastic reduction of the sheet resistance would be necessary. To achieve this, it would be needed to spray more layers with the consequential loss of transparency [36] or by using a third material to improve the junction [37].

4. Conclusions

We have demonstrated the feasibility of producing spray-deposited, large-scale, and semitransparent thermocouples on flexible substrates. These thermocouples show Seebeck coefficients of up to 54 μV/K and a very linear response, being a perfect candidate for autonomous temperature sensing. The best combination in terms of Seebeck coefficient was found for the junction made of AgNWs and CNTs,

Table 3: Comparison among planar thermocouples.

Reference	Thermocouple type	Seebeck coefficient (μV/K)	Temperature range (K)
Yu et al. [17]	Doped multiwalled CNT (MWCNT) bundles with metal contact [17]	22	110–300
Penza et al. [22]	CNT bundles with Cr-Al electrodes	40.7	293–343
Miao et al. [38]	Isolated MWCNTs with Pt-electrodes	~35	260–420
This work	AgNWs-SWCNTs	50.4	293–273
	SWCNTs-PEDOT:PSS	26.9	
	AgNWs-PEDOT:PSS	14.8	

depositing them in the mentioned order. The achievement of such semitransparent devices, easy to integrate into other systems with means of conventional solution-processing methods, is a first step towards transparent electronic devices, seamlessly integrated into windows or windshields. Finally, although further work is still necessary to overcome the current limitations, such as the high resistance, which hinders the use as energy harvesters, the methods we describe in this work, coupled with a choice of materials more tailored to the applications, can be generalised and employed for the realization of thermally sensitive electronics, where transparency, cost effectiveness, and ease of process are required.

Data Availability

The corresponding author is available to provide the interested reader with the raw data of the measurements for all the performed experiments.

Conflicts of Interest

The authors declare that they have no conflicts of interest.

Acknowledgments

This work was partially funded by the TUM Graduate School and ASK Industries Italy, through the project VASM.

Supplementary Materials

Figure S1: composition of two thermal images to compensate the two distinctly different thermal emission coefficients of foam glass (0.9) and aluminum (0.08) on the heater (top, bright) and cooler (bottom, dark). The value for the aluminum plates was experimentally evaluated and found to match the predicted range (0.08–0.09). The transition of the emission coefficients at the 12 edges of the aluminum plates was neglected. In reality, a smooth transition between the about 225°C hot heater, the about 25°C warm foam glass, and the about 5°C cold heater has to be assumed. *(Supplementary Materials)*

References

[1] A. Dey, O. P. Bajpai, A. K. Sikder, S. Chattopadhyay, and M. A. S. Khan, "Recent advances in CNT/graphene based thermoelectric polymer nanocomposite: a proficient move towards waste energy harvesting," *Renewable and Sustainable Energy Reviews*, vol. 53, pp. 653–671, 2016.

[2] S. Wang and D. D. L. Chung, "Carbon fiber polymer-matrix composite interfaces as thermocouple junctions," *Composite Interfaces*, vol. 6, no. 6, pp. 519–529, 1998.

[3] O. Yamashita, S. Tomiyoshi, and K. Makita, "Bismuth telluride compounds with high thermoelectric figures of merit," *Journal of Applied Physics*, vol. 93, no. 1, pp. 368–374, 2003.

[4] M. H. Elsheikh, D. A. Shnawah, M. F. M. Sabri et al., "A review on thermoelectric renewable energy: principle parameters that affect their performance," *Renewable and Sustainable Energy Reviews*, vol. 30, pp. 337–355, 2014.

[5] W. Honda, S. Harada, T. Arie, S. Akita, and K. Takei, "Wearable, human-interactive, health-monitoring, wireless devices fabricated by macroscale printing techniques," *Advanced Functional Materials*, vol. 24, no. 22, pp. 3299–3304, 2014.

[6] S. Kim, A. Traille, H. Lee et al., "Inkjet-printed sensors on paper substrate for agricultural applications," in *2013 European Microwave Conference*, pp. 866–869, Nuremberg, Germany, October 2013.

[7] C. Perera, C. H. Liu, and S. Jayawardena, "The emerging internet of things marketplace from an industrial perspective: a survey," *IEEE Transactions on Emerging Topics in Computing*, vol. 3, no. 4, pp. 585–598, 2015.

[8] V. Sanchez-Romaguera, M. A. Ziai, D. Oyeka et al., "Towards inkjet-printed low cost passive UHF RFID skin mounted tattoo paper tags based on silver nanoparticle inks," *Journal of Materials Chemistry C*, vol. 1, no. 39, pp. 6395–6402, 2013.

[9] M. Irimia-Vladu, ""Green" electronics: biodegradable and biocompatible materials and devices for sustainable future," *Chemical Society Reviews*, vol. 43, no. 2, pp. 588–610, 2014.

[10] J. Gong, S. B. Darling, and F. You, "Perovskite photovoltaics: life-cycle assessment of energy and environmental impacts," *Energy & Environmental Science*, vol. 8, no. 7, pp. 1953–1968, 2015.

[11] T. Mustonen, K. Kordás, S. Saukko et al., "Inkjet printing of transparent and conductive patterns of single-walled carbon nanotubes and PEDOT-PSS composites," *Physica Status Solidi (b)*, vol. 244, no. 11, pp. 4336–4340, 2007.

[12] A. Sandström, A. Asadpoordarvish, J. Enevold, and L. Edman, "Spraying light: ambient-air fabrication of large-area emissive devices on complex-shaped surfaces," *Advanced Materials*, vol. 26, no. 29, pp. 4975–4980, 2014.

[13] A. Abdellah, B. Fabel, P. Lugli, and G. Scarpa, "Spray deposition of organic semiconducting thin-films: towards the fabrication of arbitrary shaped organic electronic devices," *Organic Electronics*, vol. 11, no. 6, pp. 1031–1038, 2010.

[14] A. Falco, M. Petrelli, E. Bezzeccheri, A. Abdelhalim, and P. Lugli, "Towards 3D-printed organic electronics: planarization and spray-deposition of functional layers onto 3D-printed objects," *Organic Electronics*, vol. 39, pp. 340–347, 2016.

[15] M. Binda, D. Natali, A. Iacchetti, and M. Sampietro, "Integration of an organic photodetector onto a plastic optical fiber by means of spray coating technique," *Advanced Materials*, vol. 25, no. 31, pp. 4335–4339, 2013.

[16] C. Meng, C. Liu, and S. Fan, "A promising approach to enhanced thermoelectric properties using carbon nanotube networks," *Advanced Materials*, vol. 22, no. 4, pp. 535–539, 2010.

[17] C. Yu, Y. S. Kim, D. Kim, and J. C. Grunlan, "Thermoelectric behavior of segregated-network polymer nanocomposites," *Nano Letters*, vol. 8, no. 12, pp. 4428–4432, 2008.

[18] M. Bobinger, D. Angeli, S. Colasanti, P. La Torraca, L. Larcher, and P. Lugli, "Infrared, transient thermal, and electrical properties of silver nanowire thin films for transparent heaters and energy-efficient coatings," *Physica Status Solidi (a)*, vol. 214, no. 1, 2017.

[19] W. Hong, Y. Xu, G. Lu, C. Li, and G. Shi, "Transparent graphene/PEDOT–PSS composite films as counter electrodes of dye-sensitized solar cells," *Electrochemistry Communications*, vol. 10, no. 10, pp. 1555–1558, 2008.

[20] Z. Wu, Z. Chen, X. Du et al., "Transparent, conductive carbon nanotube films," *Science*, vol. 305, no. 5688, pp. 1273–1276, 2004.

[21] O. Bubnova, Z. U. Khan, A. Malti et al., "Optimization of the thermoelectric figure of merit in the conducting polymer poly (3, 4-ethylenedioxythiophene)," *Nature Materials*, vol. 10, no. 6, pp. 429–433, 2011.

[22] M. Penza, R. Rossi, M. Alvisi et al., "Thermoelectric properties of carbon nanotubes layers," in *Sensors and Microsystems*, pp. 73–79, Springer, 2011.

[23] A. Falco, L. Cinà, G. Scarpa, P. Lugli, and A. Abdellah, "Fully-sprayed and flexible organic photodiodes with transparent carbon nanotube electrodes," *ACS Applied Materials & Interfaces*, vol. 6, no. 13, pp. 10593–10601, 2014.

[24] M. Schmidt, A. Falco, M. Loch, P. Lugli, and G. Scarpa, "Spray coated indium-tin-oxide-free organic photodiodes with PEDOT: PSS anodes," *AIP Advances*, vol. 4, no. 10, article 107132, 2014.

[25] J. Krantz, T. Stubhan, M. Richter et al., "Spray-coated silver nanowires as top electrode layer in semitransparent P3HT: PCBM-based organic solar cell devices," *Advanced Functional Materials*, vol. 23, no. 13, pp. 1711–1717, 2013.

[26] K. Zilberberg, F. Gasse, R. Pagui et al., "Highly robust indium-free transparent conductive electrodes based on composites of silver nanowires and conductive metal oxides," *Advanced Functional Materials*, vol. 24, no. 12, pp. 1671–1678, 2014.

[27] M. Bobinger, V. Dergianlis, A. Albrecht et al., "Solution processing of silver nanowires for transparent heaters and flexible electronics," in *2017 13th Conference on Ph.D. Research in Microelectronics and Electronics (PRIME)*, pp. 9–12, Giardini Naxos, Italy, June 2017.

[28] J. H. Lee, K. Y. Lee, M. K. Gupta et al., "Highly stretchable piezoelectric-pyroelectric hybrid nanogenerator," *Advanced Materials*, vol. 26, no. 5, pp. 765–769, 2014.

[29] T. Park, J. Na, B. Kim, Y. Kim, H. Shin, and E. Kim, "Photothermally activated pyroelectric polymer films for harvesting of solar heat with a hybrid energy cell structure," *ACS Nano*, vol. 9, no. 12, pp. 11830–11839, 2015.

[30] J. J. Lee, D. Yoo, C. Park, H. H. Choi, and J. H. Kim, "All organic-based solar cell and thermoelectric generator hybrid device system using highly conductive PEDOT: PSS film as organic thermoelectric generator," *Solar Energy*, vol. 134, pp. 479–483, 2016.

[31] W. Cao, J. Li, H. Chen, and J. Xue, "Transparent electrodes for organic optoelectronic devices: a review," *Journal of Photonics for Energy*, vol. 4, no. 1, article 040990, 2014.

[32] A. Abdellah, A. Abdelhalim, F. Loghin et al., "Flexible carbon nanotube based gas sensors fabricated by large-scale spray deposition," *IEEE Sensors Journal*, vol. 13, no. 10, pp. 4014–4021, 2013.

[33] F. Loghin, S. Colasanti, A. Weise et al., "Scalable spray deposition process for highly uniform and reproducible CNT-TFTs," *Flexible and Printed Electronics*, vol. 1, no. 4, article 045002, 2016.

[34] G. Haacke, "New figure of merit for transparent conductors," *Journal of Applied Physics*, vol. 47, no. 9, pp. 4086–4089, 1976.

[35] A. Falco, P. Lugli, F.-C. Loghin, and A. Rivadeneyra, "Design, simulation and fabrication strategies for printed out-of-plane thermoelectric devices," in *2017 IEEE Sensors*, pp. 1–3, Glasgow, UK, November 2017.

[36] A. Falco, J. Salmerón, F. Loghin, A. Abdelhalim, P. Lugli, and A. Rivadeneyra, "Optimization of process parameters for inkjet printing of CNT random networks on flexible substrates," in *2016 IEEE 16th International Conference on Nanotechnology (IEEE-NANO)*, pp. 487–490, Sendai, Japan, August 2016.

[37] A. Dey, A. Maity, M. A. S. Khan, A. K. Sikder, and S. Chattopadhyay, "PVAc/PEDOT: PSS/graphene–iron oxide nanocomposite (GINC): an efficient thermoelectric material," *RSC Advances*, vol. 6, no. 27, pp. 22453–22460, 2016.

[38] T. Miao, S. Shi, S. Yan et al., "Integrative characterization of the thermoelectric performance of an individual multiwalled carbon nanotube," *Journal of Applied Physics*, vol. 120, no. 12, article 124302, 2016.

Hindawi
Journal of Sensors
Volume 2018, Article ID 6576841, 17 pages
https://doi.org/10.1155/2018/6576841

Research Article

VANSec: Attack-Resistant VANET Security Algorithm in Terms of Trust Computation Error and Normalized Routing Overhead

Sheeraz Ahmed,[1,2] **Mujeeb Ur Rehman**,[2] **Atif Ishtiaq**,[1] **Sarmadullah Khan**,[3] **Armughan Ali**,[4] **and Shabana Begum**[5]

[1]*Iqra National University, Peshawar, Pakistan*
[2]*Career Dynamics Research Centre, Peshawar, Pakistan*
[3]*School of Computer Science and Informatics, De Montfort University, Leicester LE1 9BH, UK*
[4]*COMSATS Institute of Information Technology, Attock, Pakistan*
[5]*Islamia College University, Peshawar, Pakistan*

Correspondence should be addressed to Sheeraz Ahmed; sheerazahmed306@gmail.com

Received 23 February 2018; Revised 15 May 2018; Accepted 4 June 2018; Published 16 July 2018

Academic Editor: Almudena Rivadeneyra

VANET is an application and subclass of MANETs, a quickly maturing, promising, and emerging technology these days. VANETs establish communication among vehicles (V2V) and roadside infrastructure (V2I). As vehicles move with high speed, hence environment and topology change with time. There is no optimum routing protocol which ensures full-pledge on-time delivery of data to destination nodes, and an absolutely optimum scheme design for flawless packet exchange is still a challenging task. In VANETs, accurate and on-time delivery of fundamental safety alert messages (FSAMs) is highly important to withstand against maliciously inserted security threats affectively. In this paper, we have presented a new security-aware routing technique called VANSec. The presented scheme is more immune and resistive against different kinds of attacks and thwarts malicious node penetration attempts to the entire network. It is basically based on trust management approach. The aim of the scheme is to identify malicious data and false nodes. The simulation results of VANSec are compared with already existing techniques called trust and LT in terms of trust computation error (TCE), end-to-end delay (EED), average link duration (ALD), and normalized routing overhead (NRO). In terms of TCE, VANSec is 11.6% and 7.3% efficient than LT and trust, respectively, while from EED comparison we found VANSec to be 57.6% more efficient than trust and 5.2% more efficient than LT. Similarly, in terms of ALD, VANSec provides 29.7% and 7.8% more stable link duration than trust and LT do, respectively, and in terms of NRO, VANSec protocol has 27.5% and 14% lesser load than that of trust and LT, respectively.

1. Introduction

Communication remains a main focus of interest in human beings. Hence, in results of continuous struggle, it became possible to replace one communication medium by other fastest communication means for sending and receiving information. Computer networks are a bunch of networked computing hardware devices interchanging data to the communicating networked devices through a data link. The link between nodes is fixed, that is, wired or with wireless media. The Internet is a prominent computer network. Wireless technology does not provide full security of information because the medium is open. To ensure security, encryption/decryption techniques are used to identify the authorized users. Table 1 shows different types of wireless networks.

The wireless sensor network (WSN) is a self-organizing, infrastructureless network. WSN is an example of wireless networks using IEEE 802.15.4 protocol designed for low-rate WPANs and also for sensor networks. WSN consists of numerous small sensors with low cost, low battery power, and limited computational capabilities and low communication bandwidth. These sensor nodes are used to collect information as well as integrate and transmit data in a wireless fashion and handover it to the base station (BS) via a gateway node [1]. WSN is comprised of power components, radio transceiver, and computing and sensing devices. Sensors are

Table 1: Different types of wireless networks.

Type	Applications	Range	Standards
Personal area network (PAN)	Cable replacement for peripherals	Within reach of a person	Bluetooth, ZigBee, NFC IEEE 802.15
Local area network (LAN)	Wireless extension of wired network	Within a building or campus	IEEE 802.11 (Wi-Fi)
Metropolitan area network (MAN)	Wireless internetwork connectivity	Within a city	IEEE 802.16 (WiMAX)
Wide area network (WAN)	Wireless network access	Worldwide	Cellular (UMTS, LTE, etc.)

hundreds and thousands in number, communicating with each other through radio communication over an industrial, scientific, and medical (ISM) radio band.

To obtain information on location and positioning, local positioning algorithms and the global positioning system (GPS) can be employed [2]. The IEEE 802.11p standard known as wireless access in vehicular environments (WAVE) is a specially developed version to adapt vehicular ad hoc network (VANET) requirements and support intelligent transport systems (ITS). IEEE 802.11p is one of the fresh sanctioned amendments to the IEEE 802.11 standard to add wireless access in vehicular environments (WAVE). In this sense, IEEE 802.11p is denoted as WAVE.

Information and communication technology (ICT) plays a vital role in making the cities smarter in the future through intervehicle communication (IVC), using an infrastructure of Car4ICT using IEEE 802.11p based on dedicated short-range communication (DSRC) protocol [3]. Car4ICT infrastructure is a future technology which will facilitate users by easily accessing different applications like routing, uploading, and downloading data. It also provides data processing and storage facilities for the users. Such services are complex and require detailed knowledge to constitute it in big cities [3]. IEEE 802.11 is an accumulation of physical layer (PHY) specifications and media access control (MAC) for implementing WLAN in the 2.4, 3.6, 5, and 60 GHz frequency bands, maintained by the IEEE 802 LAN Standards Committee in 1997.

A mobile ad hoc network (MANET) is a network which has many autonomous mobile nodes which are free to move in any direction, also continuously modifying their locations in a self-configurable manner. It is an infrastructureless network; these nodes have the capacity to connect with Wi-Fi or any cellular infrastructure. VANET is an application of MANETs. VANET is a wireless ad hoc network, in which moving vehicles behave like mobile nodes and allow them to connect with each other via DSRC, and a protocol proposed for WAVEs is IEEE 802.11p for IVC. VANETs enable infrastructure-to-vehicle (I2V), or vehicle-to-infrastructure (V2I), and vehicle-to-vehicle (V2V) communication system [4, 5].

V2I communication is a wireless exchange of safety messages and access to the Internet between vehicles and roadway side units. A major concern of VANETs is to avoid vehicle collisions and get updates about road condition, weather information, traffic jam situation, and so on. In V2V infrastructure, when vehicles come in the communication range, it results in an automatic connection and establishes an ad hoc network. This enables sharing of position, speed, and direction data; again, DSRC connects with the global positioning system (GPS) resulting in a V2V communication system which provides a 360° view of vehicles within the communication range.

VANETs utilize movable vehicles and establish a wireless link among vehicles with features such as rapid changing topology, high computational ability, predictable mobility, and variable network density. VANET architecture consists of three parts: (i) an on-board unit (OBU) which is built in the vehicles or vehicles itself, (ii) an application unit (AU) person set in the car, that is, driver, and (iii) a roadside unit (RSU) installed on highways which constitutes the VANET system and provides a basis for an intelligent transportation system (ITS) [4, 5]. The researchers successfully advent a network with the collaboration of WSNs and VANETs named as vehicular sensor networks (VASNETs). Vehicles are mobile nodes in VASNET, and an important application for vehicular networks is cooperative collision warning (CCW) message disseminations, which uses V2V communication and hence achieves safety [6]. The basic VANET structure is shown in Figure 1.

VANET is an application of mobile ad hoc networks (MANETs) which differs from MANETs in a few ways like the following. (i) Power is a constraint in MANETs, but in the case of VANETs, power is not due to tremendous installed battery. (ii) Moving pattern: in VANETs, nodes move coherently, while in MANETs node moments are random. (iii) Mobility: the mobility ratio in VANETs is bigger than in MANETs [6]. VANETs have three main architectural categories, which are as follows. (i) Pure ad hoc mode: in this mode, only V2V communication exists and no other infrastructure takes part. (ii) Pure cellular or WLAN mode: in this mode, vehicles can easily access information from cellular towers and access points (APs). (iii) Hybrid mode: this mode can use and access data from cellular/WLANs as well as from pure ad hoc mode depending upon the information capacity and route congestions [4, 5].

VANETs have different characteristics, summarized as follows:

(i) *High mobility*: in VANETs, vehicles move at high velocity which causes the contraction of the mesh network. So, in such case, vehicle position identification is difficult and it also leads to poor security provision to node privacy.

(ii) *Rapidly changing network topology*: in VANETs, vehicles move randomly with high speed, so evidently

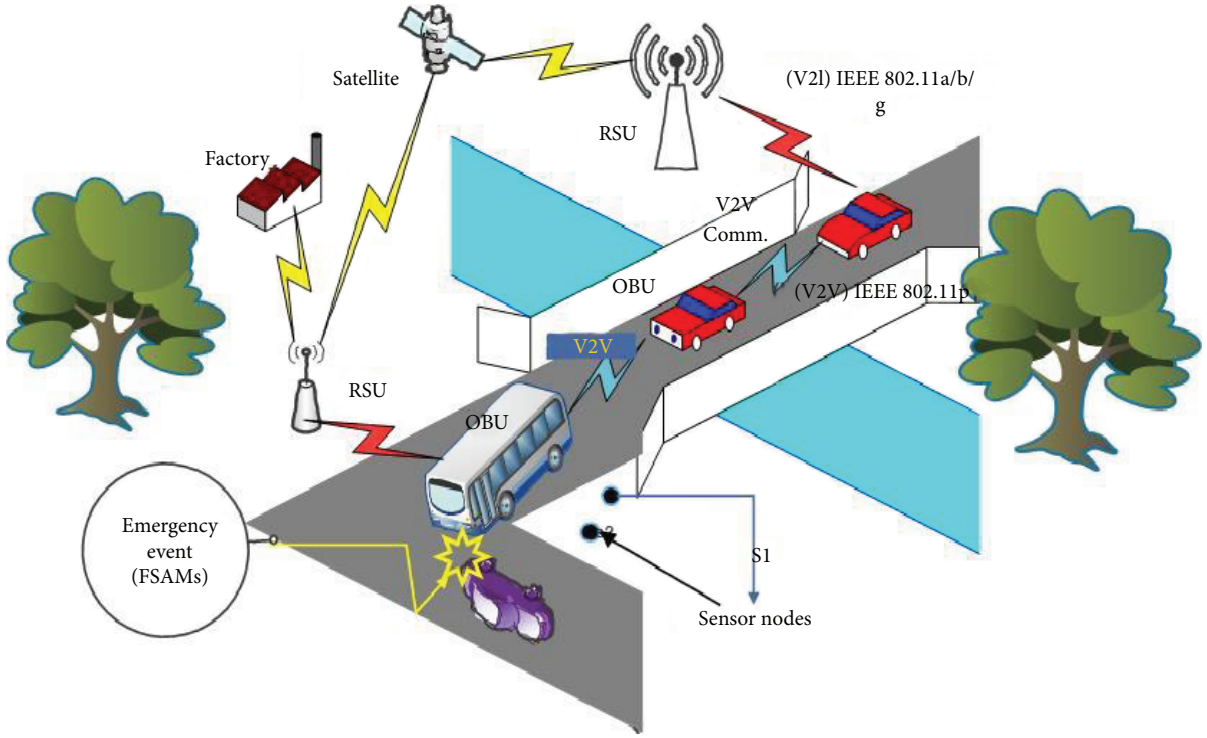

Figure 1: Basic VANET structure.

the position of vehicles will change most oftenly. The topology is dynamic and irregular. It encourages attacks in the network and makes it difficult to sort out misbehavior/attacks in the network [7].

(iii) *Availability of the transmission medium*: VANET size in the geographical point of view is boundless. VANET infrastructure can be designed for a city, cities, or as a whole for a country. The wireless medium is a universally available transmission medium, which is a big reward in IVC.

(iv) *Frequent exchange of information*: the VANET network is ad hoc in nature. In VANETS, nodes gather information from the neighbor vehicular nodes and also from RSUs. So, in this way, nodes exchange their information.

(v) *Attenuations*: DSRC is a digital transmission band facing problems in transmission frequencies; these are reflection, diffraction, and dispersion, various kinds of fading phenomena, and Doppler effect losses. Due to multipath padding propagation, delays occur [7].

(vi) *Time critical*: in VANETs, time period management is absolutely needed; it should be ensured that information reaches to the exact accurate node in the specified time, to enable the node for decision and execute action accordingly.

(vii) *Limited bandwidth*: VANETs use the DSRC band with a limited bandwidth of 27 MHz; the theoretical data rate is 27 Mbps.

(viii) *Energy storage and computing*: VANET is rich in energy, computing capability, and storage.

(ix) *Limited transmission power*: in a WAVE scenario, the transmission power is up to 1000 m and ensures data reachability to nodes. In congestion or accident situation, transmission power can be maximizes [7].

Security of VANETs is an important factor which protects information related to the driver and vehicle from unauthorized access and ensures privacy of the driver and vehicle. In VANET scenario, nodes are highly dynamic; in such networks, information security is a very tough job.

1.1. Security Requirements in VANETs. To ensure information security, different security goals should be fulfilled; the most common security requirements are confidentiality, data integrity, and availability. In addition, other security requirements are authentication, data check, and nonrepudiation [8]. So, collectively in VANETs, six security goals should be fulfilled. Keeping information hidden from unauthorized access is called *confidentiality*, protecting information from unauthorized changes is called *integrity*, and accessibility to the required information by an authorized user is called *availability* [7]. The process which belongs to the verification of information generated by the sanctioned user is called *authentication*. The transmitted message is confirmed and checked by the receiving node/vehicle; whether the received data is correct or having some false information is called *data check*. *Nonrepudiation* is the process in which the sender of a message cannot disown himself from the communication at

the end of the communication session [8]. Data correlation can also be considered a security requirement which easily finds out bogus data, by correlation to finger out the similarity between the data received and the data transmitted. Making secure the position of vehicle and BS is also a concern with VANET security [7]. Entities that are involved in VANET security are drivers, OBUs, RSUs, and attackers. The driver is a key part of the VANET system taking decision in emergency situations providing safety to the vehicle and comfort to passengers.

Vehicle OBU may be a normal automated system or may be an attacker impersonating himself as a normal node, and similarly RSUs can be normal or may be a malicious node and can disrupt the normal network activities for the attacker's own benefits. Attackers can launch different kinds of techniques to interrupt normal network functions; attackers can be internal or external, and they have only one motive to benefit themselves [7]. Attackers can be of two types; they may be rational and irrational and can do active or passive attacks. Active attacks are detectable while passive attacks are not. The third party should be a trusted or semitrusted authority, or it may be a manufacturer of the vehicles which is also a key entity of the VANET system [8].

1.2. Possible Attacks that Are Vulnerable to VANET Security

(i) Attacks on availability: in such attacks, the attacker shuts down the entire network and the node has no access to the information.

(ii) Attacks on authentication: identification of vehicles is mandatory to rectify the genuine sender and receiver, confirm identity first to kick out intruders, and reduce the chance of information loss.

(iii) Attacks on confidentiality: the information should be confidential between the authorized users and kept hidden or encrypted from the intruders to avoid traffic analysis or snooping attacks.

(iv) Attacks on integrity: the intruder should change the data by deletion, insertion, and modification of data according to his requirements and benefits. Data integrity keeps away repudiation and replaying attacks.

(v) Attacks on nonrepudiation: the ability to confirm that the sender and receiver of the message are authentic users and at the end they cannot refuse to acknowledge [7, 9].

(vi) Another attack known as denial of service (DOS) or distributed denial of service (DDOS): it hijacks the network totally, slows down the entire process and interrupts the services of network. The intruders send many fake or bogus requests, reply to the network, and impersonate themselves as a normal vehicle OBU or RSU, and the network seems busy or out of reach, not responding to the genuine vehicles [10].

(vii) Identity revealing: disclosing details of the individual vehicle can put security at danger. Later character revealing must be avoided.

The various other types of attacks are like broadcast tampering, Sybil attacks, message suppression attacks, alteration attack, and wormhole attack [11]. Lots of research work are done on ITS, and nodes are equipped with communication technology. Messages are exchanged between nodes containing information regarding their current location and its surroundings. Different techniques are used in the VANET system to enhance its security. To reduce the accident ratios and ensure safe transportation, different approaches are used to identify the causes of traffic accidents in ITS.

National Databank Wegverkeer (NDW) is a database containing real-time data about the traffic network of the Netherlands. When a crash occurs, the factor can be easily found out from NDW. Another technique is event data recorder (EDR), a device built in the vehicle which collects violent information regarding the vehicle's speed, heading, and engine accelerator. The main aim of EDR is to get information about the event when the crash is faced by the vehicle system, that is, EDR provides postaccident information and causes of the accident can be easily investigated. EDR can also collect other kinds of data if appropriate sensor nodes are used [12].

IEEE 802.11p is a standard protocol for WAVE. In VANETs, vehicles are equipped with DSRC to broadcast messages to neighbor nodes. Neighbor nodes/vehicles are also equipped with DSRC or stationary stations located at the roadside. These messages contain information, like safety warnings and traffic information. IEEE 802.11p determines a set of two types of messages: cooperative awareness message (CAM) and decentralized environmental notification message (DENM) used in ITS [12]. CAM is broadcast and replicated again and again to all nodes in the neighborhood. CAM shows positioning and other basic status-related information of the communicating entities in the ITS system [12]. DENM is the second message presented by 802.11p. The message is also broadcasted to other ITS stations when a particular incident occurs to inform other vehicles. Wrong way driving, accident, and roadwork are the examples of such incidents.

On detection of hazardous events by the ITS station, it starts broadcasting without any delay a DENM message to other ITS stations in the region (a specific geographical area) which can be affected by the event. The message is continuously broadcasting repeatedly, till the event is over. When the specified event is over, a special DENM message is circulated to inform all nodes about the disappearance of the event [12].

An autonomous traffic management scheme which enables the vehicular network, to exchange data between vehicles, should be about the change of route in case of congestion, traffic jam condition, or any other emergency situation. The network is called VANET-based autonomous management (VAM) scheme.

In the presence of traffic light, VAM establishes coordination between vehicles and the light controller to overcome congestion [13].

To keep information security in VANETs, different approaches are used. Public key cryptography (PKC) is an asymmetric key algorithm, in which a key used for encryption of a message is not used for the decryption of that message. Encryption and decryption are done with two separate keys. In such algorithms, each node has a pair of cryptographic keys: one is public encryption key (PEK) and the other is private decryption key (PDK). The pair of cryptographic keys is generated by the real time application (RTA) technique periodically. Public keys are reached to each and every RSU in its operation area via a secure medium/channel.

Traditional wired networks are protected by several lines of defense such as firewalls and gateways. Security attacks on such networks may come from any direction and target all nodes. VANETs are susceptible to intruders ranging from passive eavesdropping to active spamming, tampering, and interfering due to the absence of basic infrastructure and centralized administration. The main challenge facing VANETs is user privacy. Whenever vehicular nodes attempt to access some services from roadside infrastructure nodes, they want to maintain the necessary privacy without being tracked down for whoever they are, wherever they are, and whatever they are doing. It is considered as one of the important security requirements that should be paid more attention for secure VANET schemes, especially in a privacy-vital environment [14].

2. Literature Review

ITS and VANETs have been under research for many years. But with the advancement in generation of communication technology, there is a need to refine the information exchange process and come up with better security and more fulfilling solutions against threats that meet the demands of the day. With the world moving steadily towards WAVE, there is a need to refigure the entire ITS system security and ensure that the VANET security process does not prove to be a bottleneck in the advancement of the ITS technology. We shall have a look at some of the earlier works done in the field of VANET security in order to eliminate or reduce the frequency of attacks in VANETs by malicious nodes.

In paper [15], researchers proposed a novel authentication mechanism for secure message transmission in a VANET scenario. The author has shown that an already existing technique of message authentication was based on a combined signature technique, in which the forwarding node used a combined signature algorithm via RSU and results in a huge transmission overhead message. Due to a combined signature scheme, RSU sometimes transmits fake authenticated messages toward nodes. To avoid such issues, the authors proposed an aggregate message authentication code technique which verifies the integrity and authenticity of messages and thinned communication overhead.

Pseudo-RSUs were installed in the neighborhood of RSU to stop false information dissemination, to ensure exchange of rectified authenticated messages. The authors proposed a technique based on results obtained from simulations and security parameters which reduced considerably the communication overhead and enhanced the validity of disseminated information, which validated the authors' suggested technique. In [16], the authors fabricated a technique which has studied security aspects of V2V communication utilizing a radiofrequency (RF) transceiver. The main part of the VANET environment is position-based information of the vehicular node. The use of an RF transceiver improved the trust on received data about the vehicle's location. The suggested model of authors followed the rule of "Trust on what you observed, confirm what you listen." The basic motive of the scheme was to find a vehicular communication system best suited in minimum cost and more effective in data distribution, as well as to ensure passengers' safety, security, and comfortability.

The RF transceivers verify reported data in the network and approve the position of the neighbor's vehicles and that of the malicious vehicle too and hence ensured the security of the network. The authors suggested a scheme which enhanced VANET security through precluding malicious entities from penetration into the network, hence reducing the chances of putting invalid data about the position information of vehicles.

In paper [17], researchers designed a novel technique of detection, named greedy detection for VANETs (GDVANs); it was for the purpose of reducing greedy behavior frequency in VANETs. VANETs' basic motive was to assure road passengers' safety and enhance transportation quality. Multiple attacks were launched in VANETs; among them, one was denial of service (DOS) attack, which interrupted authorized clients from available information.

The authors proposed a technique incorporating two phases: suspicious phase and decision phase. The suspicious phase followed the concept of linear mathematical regression, where a fuzzy logic decision scheme was followed by a decision phase. The advantage of the designed scheme was that the network nodes had the capacity of execution and no change was required in the standard IEEE 802.11p protocols at any stage. Moreover, the technique had the ability of greedy behavior-type threat detection and found a potentially compromised node list, utilizing three newly defined metrics. The authors justified and validated their proposed scheme from results obtained from experiments or simulation.

In [18], the authors demonstrated that VANETs basically had the opportunity of safe wireless communications with threat avoidance capability, but still, security threats in VANETs are a disputing task, like access control, integrity of data, confidentiality, nonrepudiation, availability, and data privacy. The paper suggested a model which was about VANETs protecting against threats, labeled as an attack-resistant trust (ART) management algorithm. ART had not only detection capability of malicious data and node but also the ability to deal with malicious attacks. In VANETs, ART judged the trustworthiness of both data and mobile nodes. Especially, assessment of data trust was done on the basis of sensed and collected data from various vehicles; judgment of node trust was done in two ways, that is, functional trust and recommendation trust, which reveal how probably a node could accomplish its functionality and how trustworthy the recommendations from a node for other nodes would be,

respectively. The authors validated their proposed scheme ART, via experimental data they analyzed. Moreover, the scheme ART had broad applications in VANET background, to enhance traffic experimentation in terms of secure mobility, with reinforced reliance. Agarwal et al. [19] developed a theory to assure security inside educational institutions, medical institution/health care centers, residential places, and so on, through conversion of stodgy vehicles into connected vehicles to prevent careless driving. In the designed model, entry and exit points (gates) were defined. Authors suggested wireless hardware-type "GPS" arrangement to supervise moving vehicles, velocity, and region of entry. At the entryway, orthodox vehicles obtain a device from guards on duty and return the device back upon exiting to authorized guards on duty.

When the devices were activated, a communication mean/path is set up among security depots and drivers inside the specified region to avoid rule violation. For vehicles inside that particular region which have a speed threshold, on crossing the threshold value warning messages were disseminated between the vehicle operator and the system. In the depot, receiving unit holds previous record of each individual drive separately; in terms of any misconduct penalizing action taken versus the handed driver. The scheme proposed by authors was judged on trial bases and, over race, was cut down up to sixty percent securing residential human areas; these characteristics validated the scheme efficacy.

In [20], researchers had considered VANET a complicated network, in which all vehicular node moments were in random manner. In VANETs, the node position changes, so data dissemination was a problem; also, creation of new links took place each time for data packet transmission. So, in such scenario, an attack could wind up all communications running among vehicular nodes. According to authors' conclusion, the Sybil attack was one among other different attacks in VANETs, due to which packet loss occurred. In this paper, the authors discuss impacts of Sybil attempts on VANET communication protocols. Further, researchers examined and scrutinized the verity of VANET routing hierarchies and found the AODV routing scheme to be more efficient in terms of attacks launched in VANET fencing. In the existence of attack in VANETs, the AODV algorithm used simulator QualNet 5, whose output results were satisfactory, but more advancement in routing hierarchy was still required.

Researchers in [21] exhibited that VANET security was the most research-adopted area due to its quality of providing better protection to drivers, vehicles, and so on. Vehicles in VANETs move with maximum acceleration, and also network topology dynamically changes which makes it hard to wipe out false invalid nodes totally and ensure dispersion of data among nodes safely. Hence, in the authors' view, information privacy and security in VANETs were the most vital research-inquired tasks.

In the paper, the authors exemplified different security threats to VANETs and pointed out possible remedy algorithms to mitigate those attacks. The authors had categorized those defensive mechanisms and analyzed them on a dissimilar performance point of view. Eventually, research workers found different research subjects based upon VANET security threats and incited scientists to work on these topics and discover an efficient method to resolve threats and attacks in VANETs.

Research work in [22] presented a detection problem of DOS attacks happening in VANETs. The authors' primary contribution was to conceptualize a new security model based on a game pattern for DOS attacks in VANETs. Secondly, researchers expressed two conditions about game theory, strategic-type game, and extensive-type game. Thirdly, authors had studied DOS attacks on the basis of practical suppositions, utilizing the actual mobility models based on an actual map. Finally, authors analyzed their designed model and validated it through a simulation process. Moreover, authors stated about their contribution in research that no such type of game-related model was designed earlier. Researchers concluded their research work analysis that they will solve DOS attack problems arising in VANETs.

In [23], researchers showed that with the growth of security techniques in VANETs, threats also grow relatively. Authors proposed a trust-based management algorithm called threshold adaptive control technique; the technique was mainly used to detect malicious and selfish nodes, and they fixed themselves inside the network intelligently. Authors showed that previous detection techniques failed up to some extent in detecting these intelligent malicious nodes. Authors have designed an adaptive detection threshold technique, which motivates the attackers to act well, and finally, the designed technique catches the malicious behavior and hence was able to detect the malicious nodes immediately.

From their simulation results, authors concluded that their designed technique had best detection ratio more than 80% even in high ratio of attackers present inside the network. Also it handovers high data packets among nodes even when VANETs are dense.

In [24], the authors proposed a trust-based framework for communication in VANETs that is capable of accommodating traffic from different applications. Their scheme assigned a trust value to each road segment and one to each neighborhood, instead of each car. It scaled up easily and was completely distributed. Experimental results demonstrated that their framework outperformed other well-known routing protocols since it routed the messages via trusted vehicles.

In [25], authors showed that only authentication of nodes was not enough for secure data transmission in the VANET network, because sometimes even authentic nodes disseminated fake information and on/off attacks lead network application to threats of various attacks. To avoid such threats and attacks, authors proposed a technique called logistic trust mechanism, which has the ability to detect and identify malicious false messages and nodes. According to authors, to detect an attack, the first correct event should be identified as data depends on the events. The proposed scheme identifies the correct event first through information collected from trusted sources and also from the receiver observation itself. On the basis of this information, in logistic

trust algorithm, the behavior of the nodes was identified through the receiver's own observation which was complemented by the opinions of other nodes. Authors proposed a scheme which had 99% accuracy in detection of malicious nodes and messages, which shows the efficacy of their proposed technique.

VANET security-oriented schemes are summarized in Table 2 given below with various parameters addressed in schemes, area of applications, techniques utilized, and deficiencies or research gaps present in these schemes.

3. Objectives of Research

In our research work, we proved our proposals with the assistance of a mathematical model and a flow chart. Our mathematical model and designed flow charts evidently validated our research. In our research work, we evaluate the performance of our design scheme VANSEC to trust [24] and logistic trust (LT) [25] schemes with respect to vehicle density using a MATLAB simulator to model all the driving environment and networking details of VANETs.

In the last phase of our research, we conducted a relative comparison. We compared our suggested VANSEC protocol with existing VANET algorithms, and comparative investigations are made and presented. The parameters we choose for our research work are TCE, EED, ALD, and NRO. In our presented scheme, the latency and TCE are dragged to minimal values and show enhanced efficacy with respect to other algorithms in terms of compared parameters.

The main objectives of our research work are as follows:

(i) To propose a protocol that can work efficiently, ensuring improvement in VANET security, and which should be scalable for the network in the future

(ii) Ensure data confidentiality, data integrity, and data availability for the clients in a VANET scenario

(iii) Propose an efficient technique to make the intruders' attempts thwart against data modification through data an insertion or deletion process

(iv) Adopting/applying different security mechanisms/protocols through which the VANET system becomes much secure as well as provides better performance in terms of delay, higher PDR, small packet loss ratio, and efficient utilization of energy resources

4. Research Methodology

The process we implemented includes three vehicles and RSUs communicating with each other via IEEE 802.11p and IEEE 802.11 a/b/g. The scenario we put in our design is a hidden node for some other nodes moving towards each other. V3 and V1 are unaware of each other, because vehicle V3 is out of range to vehicle V1, that is, V1 and V3 are not in range of each other. Both vehicles are hidden from each other. Vehicle V2 is in range of V3 as well as of V1 via DSRC. However, there is also an RSU in access of all the vehicles.

In a narrow road scenario, V3 broadcasts an alert about its speed and position to inform nearby vehicles through DSRC and sends an alert towards the RSU. Vehicle V2 received the alert and propagated the alert to its nearby vehicles as shown in Figure 2.

On reception of alert by V1 from V2 and also from RSU, V1 goes for registration or authentication verification process, to make sure that the message was issued from an authentic source or from a malicious node. From Figure 2, there is communication among vehicles which is called ad hoc mode, while with the addition of an infrastructure it is switched into infrastructure mode. The VANET security model is confined and explained with the help of a flow chart shown in Figure 3.

In the initialization process, vehicles and RSU register themselves to a registration server. The registration server verifies its authentication from a verification server to avoid penetration of malicious node and make the system secure at the primary level. There are three vehicles (V1, V2, and V3) and an RSU participating in the session; V1 receives a FSAM from V3 through V2. V1 inquired the same alert message FSAMs from RSU to confirm whether the received FSAM from V3 is correct. The decision-making block will check the similarity index. If the alert FSAMs received from both entities are the same, then it will inform the driver about the validity of node V3 also informing *ConVai* (confirm validity) message exchange about the validity of node V3 correctness, where *ConVai* exchange confirms the confidentiality of FSAMs to avoid snooping and traffic analysis. Integrity of FSAMs is checked to handle modification, masquerading, repudiation, and replay of attempts of false nodes. Also, it ensures on-time availability of FSAMs for requesting vehicles. After meeting the minimum acceptable threshold value of *ConVai* exchange, node 3 and other nodes meet the same criteria and are declared valid. These valid nodes are enlisted in the list of correct true nodes and allowed for communication or broadcasting FSAMs in the network.

If received FSAMs from RSU and V3 do not match and decision is blocked, then it is switched into another block for further verification about V3. This helps to look over node V3 position availability or unidentified position. If the position is identified, then FSAM is forwarded to the next block, to check FSAM confidentiality and for further investigation about FSAMs which is confirmed by *ConVai* exchange. After position validity and FSAM correctness, node V3 validity is endorsed and allowed for broadcasting FSAMs in the network. If node V3 position is invalid, then FSAM is discarded; again if the position of the node is valid but FSAM does not hold confidentiality check properly, FSAM is pumped into the discard bin.

Sensor nodes are also dispersed on highways which also gather data about events; Cluster Head (CH) forwards FSAMs towards *ConVai* exchange which are filtered here. If the received FSAMs from CH and RSUs are same notifying V3, then V3 and other nodes are assumed valid and are allowed for broadcasting. In case of any dissimilarity among the received FSAMs from different entities, they are pushed towards the discard bin which is shown in the flowchart diagram. All of these FSMs received from different sources alerts

Table 2: Summery of related work on VANET security.

Scheme	Technique	Area of applications	Parameters addressed	Deficiencies
Secure message delivery and authentication [15]	Aggregate message authentication code (MAC)	VANET security	Reduced communication overhead, improved authenticity	Packet loss End-to-end delay
Believe what you see, verify what you hear [16]	Detection and correction of error	VANET security	False position information detection, quick and fast data dissemination	Safety warnings, electronic toll collection, blind curve problem, etc.
Greedy detection for VANETs (GDVANs) [17]	Linear regression, mathematical concept, and fuzzy logic	VANET security	Prevention of DOS attack, no modification in IEEE 802.11p, greedy behavior detection	Duration between two successive transmission, transmission time, connection attempts made by node
Attack-resistant trust (ART) management [18]	Two separate metrics: data trust and node trust	VANET security	Ensure trustworthiness of data and node, cost effective in terms of comm. overhead	Misbehavior detection and trust management
GPS-based wireless hardware system [19]	Conversion of conventional vehicles into connected vehicles	VANET security	Limited speed threshold, effective in terms of safety, avoids accident	Cloud computing, advanced features needed to make the system smart and more realistic
AODV [20]	Routing protocol	VANET security	Sybil attack in VANETs	AODV with features of anti-Sybil attack
Various security threats and possible defensive mechanisms [21]	Threat investigation	VANET security	False info. dissemination, black hole attack, impersonation, man in the middle attacks, etc.	Security check when changing RSU by vehicles, secure private data like e-mail, IP address changed to pseudonym, etc.
Game theory model [22]	Reaction game mechanism	VANET security	DOS attack reaction problem	Costly and complex
Detection of intelligent malicious behavior [23]	Adaptive detection threshold	VANET security	High detection ratio, high packet delivery ratio, etc.	Investigates other adversaries, mobile certification authority
Trust [24]	Trust value assignment	VANET security	Routed the messages via trusted vehicles	Misbehavior detection and trust management
Logistic trust (LT) [25]	Authenticated node, correct event detection	VANET security	90% accurate with 2% error possibility in information	No specified attacks, that is, ballot stuffing and bad mouth attack.

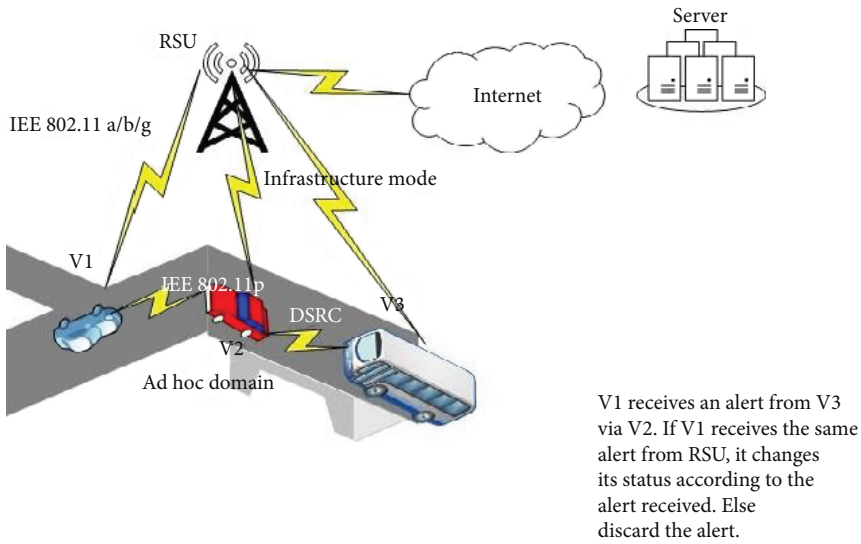

Figure 2: Vehicle-to-vehicle communication.

are forwarded to *ConVai* exchange for judgment, to check whether these alerts satisfy the *ConVai* exchange minimum accepted threshold value.

If it holds, it enhances V3's trustiness. If the received FSAMs satisfies the *ConVai* exchange minimum acceptable threshold value, then the exchange notifies and informs the driver, neighbor RSU, and CH if anything about FSAM's validity ensures V3 trustiness and accuracy. However, if the *ConVai* exchange threshold value does not meet the required criteria (certain mathematical value), then it alerts all RSU, CH, and vehicular nodes participating in the current communication session that the given FSAMs broadcast by V3 are invalid.

The alert is also forwarded to drivers to make them sure about the malicious node penetration. All these node CH and vehicles held for next FSAMs alert the message, and fake formulated FSAMs are moved toward the discard block. This reduces the level of V3 trustiness and enables other nodes to be aware about the falsehood of received FSAMs from V3 and ensures to remember the bad experience for a long time. Moreover, vehicle V3 is forbidden to pump any alert in the network because the system declares it invalid and a fake node. However, if node V3 is declared a true one, the experience of validity is also remembered for long time and enhances V3 trustiness in the entire network. It is a brief description of our flowchart shown in Figure 3 which made our efforts of the VANSEC model for VANET security useful. In the future much, work is also possible in the area of VANET security in routing protocols and thwarting different attack launches by attackers for their own benefits.

4.1. Algorithm of VANSEC Communication Model. The algorithm below exhibits that input nodes will broadcast or issue an alert message received by output nodes and act according to the received alert messages if found authentically verified through *ConVai* exchange.

5. Mathematical Modelling of VANSec Protocol

As mentioned earlier, the VANET system is a threat from various attacks. Here, we will study them mathematically and understand how they work. In the VANSec security model on reception of any consequences from the source node, the destination nodes have different ways of confirmation about the validity of received FSAMs. Two verification techniques are listed below.

In the first technique, the receiver node checks the status of the sender/source node and verifies the status of the received FSAM's validity. Secondly, the receiver goes through a comparison phase where the receiver relates and compares the results collected from the source node and neighbor nodes of the source; if both have the same opinion about the received FSAMs, then the sender is considered a valid/true node. Our designed VANSec model comprises multiple events, so the occurrence of incorrect events should also be possible. The result reported from a source needs to be confirmed before exchanging information in the network. About the event accuracy, the VANSec model collects enough evidence to list the event valid/invalid and correct false information to avoid nodes from misguidance.

Our work provides a basis for all kinds of trust models, and we also used this idea in our proposed model. The accuracy of any occurred phenomenon is recorded and based on the observation of participating nodes (from event occurrence to the reported event). So a valid node forwards a valid event towards the receiving node, and with the passage of time, more nodes are also aware about the event to occur. However, the trustiness of the discussed technique may face failure when a valid node in the VANSec model furbishes invalid/fake information. To avoid fake information dissemination, a mass metric procedure (MMP) is used to confirm actual true or valid report and contradicting report. Mass is used to measure the weight of an object. For example, you are measuring the mass of your body when you step on to a

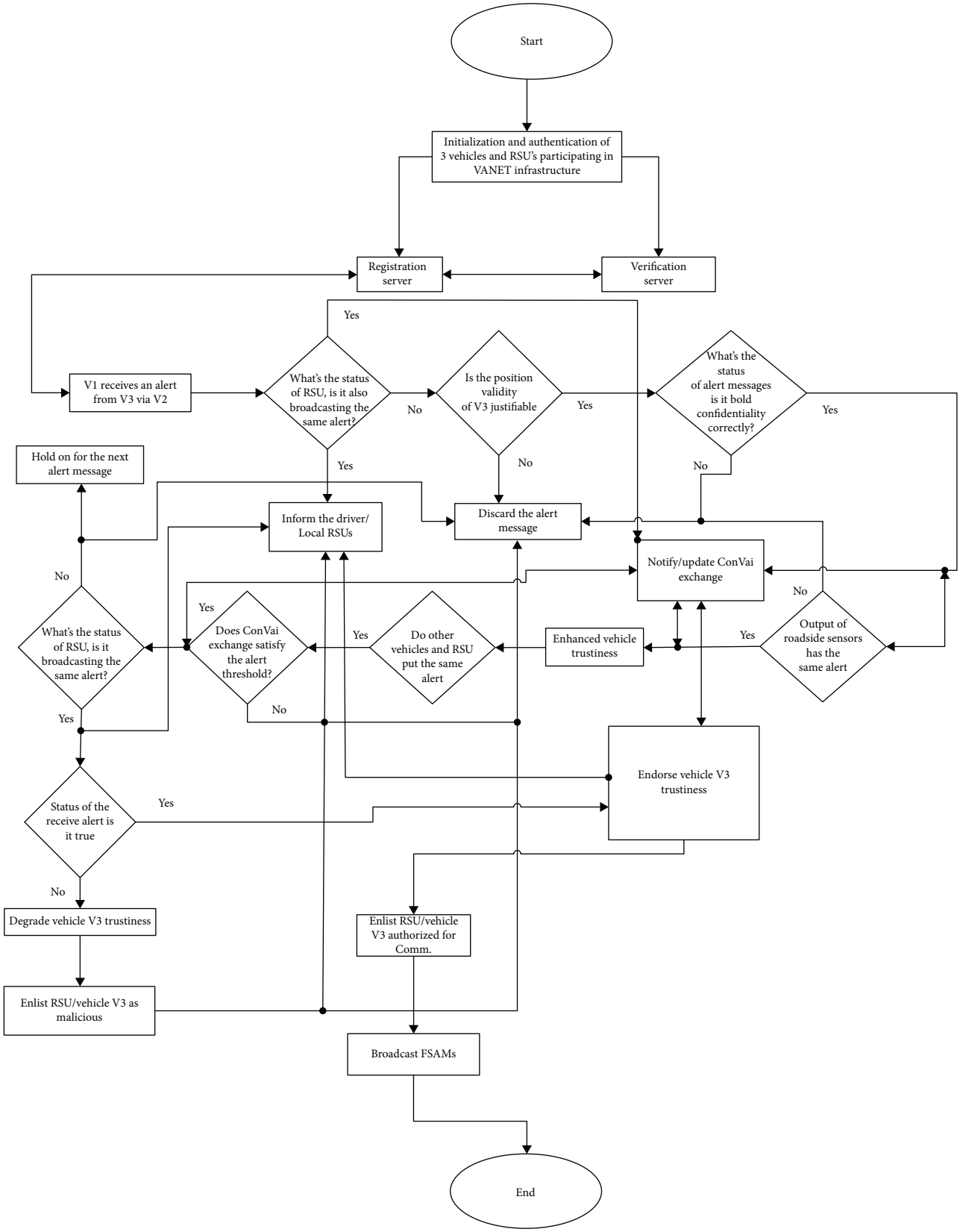

Figure 3: Flow chart of VANSEC security model.

Input: V1, V2, V3, RSUs.
Output: Only authorized node (vehicle/RSU) Broadcast information.
1: Nodes participating in communication session are {V1, V2, V3, and RSU}
2: V3 ← broadcasts an alert ← {V1 not in range while V2 and RSU receive the broadcast}
3: V1 in range of V2 ← Receives broadcast from V2
4: V1 ← receives an alert from RSU and Local sensors
5: V1 compares ← Alert {V2, RSU and Sensors}
6: V1← Verifies authenticity {V2, V3 and RSU}
7: **If** vehicle/RSU not registered
8: **then**
9: Mismatch
10: Notify ← *ConVai* exchanged and verification Server {Discard the alert message}
11: Also Notify ← V3 Trustiness degraded {V3 are black listed}
12: **else**
13: Match ← Registered and Authentic {V3, V2, RSU}
14: Update ← *ConVai* exchange {Satisfied basic security goals}
15: Enlist ← Endorse V3/RSU trustiness
16: Allow ← V3 V2 and RSU
17: Broadcast ← Alert if any
18: **end if**

Algorithm 1

scale. As we want to assign weights in affirming reports and contradicting reports, hence we have utilized this parameter. These weights are used to make a decision on relaying the messages if the equation is true. MMP is used in the decision-making process to allow the sender for communication or stop it. In (1), M_v is the valid mass metric whereas $M\neg_v$ represents contradiction.

$$\frac{M_v}{M_v + (M\neg_v)} < 1 - \xi. \tag{1}$$

The system took the source and event reporter's own confidence in the report received and then followed the received report for further action. Further, neighbor validity is also updated after looking over the results of the taken decision. If (1) becomes true, then the node is allowed for communication. However, this approach is unsafe in live safety applications, where dissemination of invalid activity may be disastrous. So, it is important to understand the nature of the reporter node well before making any decision. In trust-based approaches, the node-computed trust is a function of their own observations and opinion of neighbor nodes.

Our scheme VANSec is more immune and resistive against different kinds of attacks and thwarts malicious node penetration attempts to the entire network. It is basically based on trust management approach. The aim of the scheme is to identify malicious data and false nodes. In the designed scheme, at the beginning the node has information about the network behavior and nature. It investigates event accuracy from information received or from its own analysis. In the VANSec model, when a node undergoes unusual changes, it forwards these changes to surrounding nodes through a broadcast message and alerts nodes to switch into a safe mode. It is also possible that malicious nodes misguide other nodes through falsified FSAMs and drive the network for its benefits.

In the VANSec model, any node that receives FSAMs goes into a verification phase to understand the nature of information received before taking any decision. Therefore, a process is required to judge the correctness of received information, while the destination node holds a series of consequences achieved from received information and sender to verify the message's validity. Before any judgment about the accuracy of received information from the sender, a trust/confidence value for that sender's authenticity is established. The confidence value for the Sth sender at time interval n can be written as $C_S(n)$ where, for the message correctness about a consequence verification, the mass metric is used shown in (1), where $C_S(n)$ comes true if it follows (2).

$$0 \leq Cs(n) \leq 1. \tag{2}$$

The node has two containers: information containing a consequence is marked as P-container and is also represented by a binary digit 1, and a bin with no consequence is marked with NP-container in which also a binary digit 0 is lap to the NP-container. Average confidence values are computed from these containers utilizing sender confidence. Suppose P-container has S sender and NP-container has Q sender, the average confidence of each container at time interval n is given as

$$C_1(n) = \sum_{i=1}^{S} \frac{C_i}{S},$$
$$C_o(n) = \sum_{J=1}^{Q} \frac{C_j}{Q}, \tag{3}$$

where $C_1(n)$ is the average confidence of an event and $C_0(n)$ is the average confidence of no consequence. The normalized confidence of the node from each pot is called the mass metric of the given container which is shown in (4), where $m_i(n)$ is the mass metric of the ith node for bin 1 and $m_j(n)$ for the jth node for pot 0.

$$m_i(n) = \frac{c_i(n)}{C_1(n)}, \quad m_j(n) = \frac{c_j(n)}{C_o(n)}. \tag{4}$$

When a node confirms a consequence in its previous report and later it cannot deny from its previously submitted report; similarly if the node denies a consequence, then one cannot confirm the same event; hence, masquerading is not allowed then. The mass metric confidence for each pot is computed to judge whether the consequence is true based on information received. The average mass metric confidence for these pots is given below:

$$C^1{}_{\text{avg}}(n) = \sum \frac{m_i(n) * c_i(n)}{S}, \quad C^0{}_{\text{avg}}(n) = \sum \frac{m_j(n) * c_j(n)}{Q}. \tag{5}$$

In the decision-making process in VANSEC, the node utilizes the average mass metric confidence value to determine whether the consequence occurred or not. Hence, authentic source notifies an accurate consequence which does not threaten the decision. From (5), it is clear that $C^1{}_{\text{avg}}(n) - C^0{}_{\text{avg}}(n) > 0$ $Q > 0$, while $C^1{}_{\text{avg}}(n) > (n) >$ min ac cepted M_t when $Q = 0$ where $0 < C_{\text{avg}}(.) < 1$ and $0 <$ min ac cepted $M_t < 1$ which are the decision-making rules.

Any observation violating from the true consequence is considered malicious or eccentric; otherwise, it will be a genuine analysis. Our VANSEC model collects evaluator/judge and neighbor responses and also enlists misbehavior activity for a long time.

5.1. Evaluator/Judge Response. Evaluator/judge response is the response of a specific evaluator with a given sending source. Evaluator response is expressed in terms of eccentric ratio (ER), which evaluates whether the sender is malicious or honest. ER is defined as follows and is represented by $\Omega_n(s)$ where s is the sender/generator of packets in time interval n. $f_n(s)$ is the incorrect packet and $w_n(s)$ is the total number of packets generated by the source.

$$\text{ER} = \frac{\text{Modified or incorrect packets}}{\text{Total packets generated by source}} \Rightarrow \Omega_n(s) = \frac{f_n(s)}{W_n(s)}. \tag{6}$$

If the ER is analyzed and it crosses a particular threshold, say "Ψ," then a flag raises up indicating the source as a malicious entity and activity related to that node which is marked as untrue or false. If the ER value remains below the threshold "Ψ," then it fails in detection of malicious nodes. ER is also a decision-making ratio. To identify the node's true nature, an average ER is used.

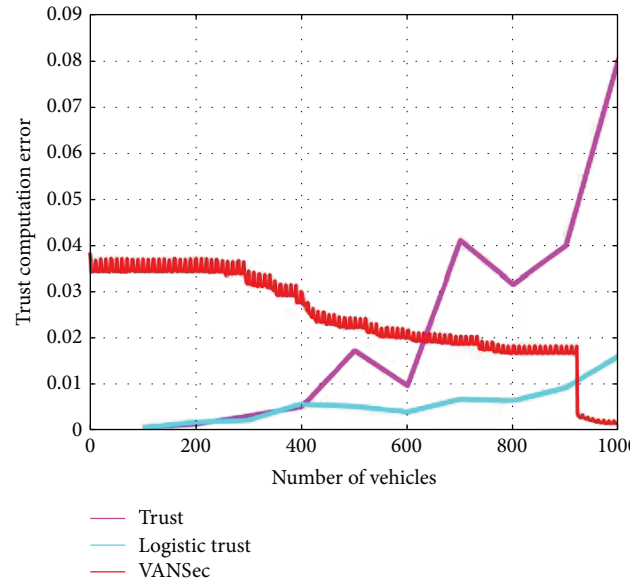

Figure 4: Trust computation error versus number of vehicles.

$$\overline{\Omega n(s)} = \frac{1}{n}\sum_{i=1}^{n} \frac{f_i(s)}{W_i(s)}. \tag{7}$$

Any node willing to establish a communication session with the source computes the ER first, so in the future the node easily broadcasts a list of trusted honest nodes and malicious nodes to its neighbor nodes. On reception of the list, the destination node updates its list of honest and malicious entries. Let us suppose that x is the node recognition entity, then λ_x is the number of malicious values received about x where H_x is the honest count. The receiving node establishes two parameters τ_x and π_x expressed with a relation given in (8). To estimate value for node x, these parameters are used.

$$\tau_x = H_x + 1, \pi_x = \lambda_x + 1. \tag{8}$$

The reputation tally for node x is

$$\text{Best tally}_X = \frac{\tau_x}{\tau_{x+\pi_x}}, \tag{9a}$$

$$\text{Worst tally}_X = \frac{\pi_x}{\tau_{x+\pi_x}}. \tag{9b}$$

From (9a) and (9b) Best Tally for x can be computed as

$$\text{Best tally}_X = 1 - \text{worst tally}_X. \tag{10}$$

5.2. Neighbor Response. Neighbor response is a response faced by neighbor nodes of a particular sender. It is an expectation obtained from neighbor nodes of a given sender in terms of binary values (0, 1). When the response of the neighbor node is binary digit 0, it means that the specific sender is malicious, while if it is one, then it points an honest node, where $Z_n(s)$ is the total number of received zeros and $O_n(s)$

Table 3: Trust computation error per 200 vehicles.

Protocol	200	400	600	800	1000	Average	% improvement
VANSec	0.03453	0.0280	0.0210	0.0166	0.00194	0.02041	4.463
Trust	0.001757	0.00719	0.0270	0.0718	0.0894	0.03942	7.30
L. trust	0.001757	0.00445	0.00546	0.00890	0.0119	0.0054	1.00

is the total number of received ones. Then, the neighbor response $N_n(s)$ is calculated as

$$N_n(s) = \frac{Z_n(s)+1}{Z_n(s)+O_n(s)+2}. \tag{11}$$

If there is no advice received about the sender and neighbor nodes, then the neighbor response $N_n(s)$ will assume a value of 0.5. Our proposed VANSec model uses characteristic confidence (CC) to filter out incorrect advices. CC uses the idea of resemblance and coherency or uniformity of advices for specific neighbors, where resemblance $R_n(L)$ is calculated between evaluator (J) and sender (L) of the data. Resemblance is calculated using the Jaccard similarity (JS) tally or score [26].

$$R_n(L) = \frac{1}{s}\sum_{g=1}^{s}\frac{A_L \cap A_{yg}}{A_L \cup A_{yg}} \tag{12}$$

Let A_L be the L sender's advice where evaluator J has its own analysis. Other advices from geographically closed nodes $y_1 \ldots y_d$ are $A_{y1} \ldots A_{yd}$ used to compare and calculate JS tally. In order to analyze the behavior of L, a time average of resemblance tally (score) is computed which is

$$\text{Res}(n)[J,L] = \epsilon * R_n(L) + (1-\epsilon) * R_{n-1}(L). \tag{13}$$

The CC in the VANSEC model also takes uniformity of advices for the current source. Suppose $I_n(L)$ is the advice value for sender L at time slot n, then $I_{n-1}(L)$ will be adviced at time $n-1$ for that sender. So the total value of advice or recommendation from L at time n will be $\|\text{AL}\|$.

Hence, uniformity will be expressed through (14):

$$\beta_n(L) = \sum_{i}^{A_L}\frac{I_n(L) \oplus I_{n-1}(L)^{\circ}}{\|A_L\|}. \tag{14}$$

To establish characteristic confidence for the VANSEC model, the time average of uniformity/coherency is used which is calculated below:

$$\overline{\beta}_n(J,L) = \varphi * \beta_n(L) + (1-\varphi)\beta_{n-1}(L). \tag{15}$$

Equation (15) shows average uniformity calculated among the evaluator (J) and source. Now combining both resemblance and uniformity to establish a CC for the VANSec model,

$$CC_n(J,L) = \theta_1 * R_{\text{es}(n)}[J,L] - \theta_2 * \overline{\beta}_n(J,L) +_3 * R_{\text{es}(n-1)}[J,L]. \tag{16}$$

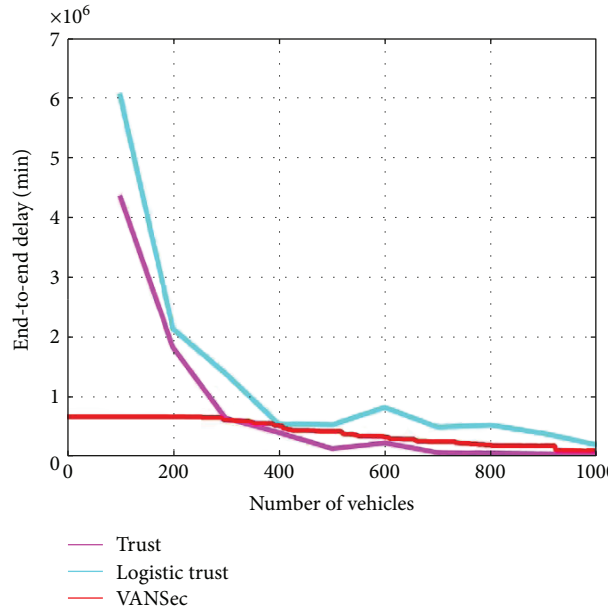

Figure 5: End-to-end delay (minutes) versus number of vehicles.

So from (16), we can easily calculate CC for a specific node and judge the nature of advice or recommendation reliability. In the VANSec model, if the value of CC falls below a particular threshold, say Υ, then the advice value for that specific node is filtered to be utilized in complete confidence trust estimation. After filtering out false untrue advices, the neighbor L and evaluator J responses along with the fanion (flag) $P_n(s)$ are collected in the VANSec model

$$t_n(J,L) = \frac{1}{1+e^{L.\vec{C}.C_o}}, \tag{17}$$

where $L = [\Omega_n(s), C_S(n), P_n(s), t_{n-1}(J,S)]$, $\vec{c}$ is the mass metric associated with each of the abovementioned parameters, and C_o is the bias and is chosen on the basis of initial confidence trust of the nodes. If initial trust assigned to a node is 0.3, then C_o will be approximately -0.85. Once the value of $\vec{c}$ is found, then a new confidence value should be computed and updated using (17). If the new calculated confidence trust value falls below threshold Δ, then the node is considered malicious, and fanion $P_n(s)$ is raised; similarly, if the confidence/trust is above threshold Δ_L, then the node is marked as a true one and $P_n(s)$ goes down.

Table 4: End-to-end delay (minutes) per 200 vehicles.

Protocol	200 v	400 v	600 v	800 v	1000 v	Average	% improvement
VANSEC	0.67	0.55	0.39	0.29	0.17	0.414	1.00
Trust	2.8	0.31	0.09	0.031	0.031	0.6524	1.576
L. trust	2.34	0.75	0.52	0.473	0.274	0.8714	2.104

The performance rate will be identified in terms of valid optimistic rate (VOR), invalid optimistic rate (IOR), and consequence detection probability (CDP). VOR is the probability of identifying an invalid/false node as invalid or untrue, while IOR is the probability of pointing an honest node as a malicious node. CDP is the probability of identifying the true result.

VOR is mathematically shown in the following equation:

$$\text{VOR} = \frac{P(\text{I/I})}{P(\text{I/I}) + P(\text{H/I})}. \tag{18}$$

where $P(I/I)$ is the probability of identifying a node as an intruder such that the given node is also intruding or malicious, while $P(H/I)$ identifies an intruder or false malicious node as a true or valid node. Similarly, IOR can be calculated via using the following relation.

$$\text{IOR} = \frac{P(I/H)}{P(\text{H/H}) + P(\text{I/H})}. \tag{19}$$

6. Simulation, Results, and Discussion

We compared our scheme to the present and tested schemes in terms of different performance metrics like TCE, EED, ALD, and NRO. To verify our VANSEC scheme to be efficient than the existing techniques, a comparison is done using simulation.

6.1. Trust Computation Error. Trust computation error (TCE) is the mean square error between the predicted/calculated and known/observed or actual trust value assessment of the vehicles. TCE can also be found through tracking the root mean square (RMS) of the calculated trust computed for all nodes. Figure 4 shows the execution of VANSec technique which is most favorable and has optimal performance than the trust scheme with logistic trust (LT). Keeping in view Table 3, VANSEC has consistency among the values of TCE with an increase of 200 vehicles in each step, while in case of trust and logistic trust techniques there is no such consistency among the values of TCE with 200 vehicles per step increase recorded.

Moreover, the TCE contributes to an interpretation that trust estimation in VANSec is more active, precise, and authentic, while in case of trust and logistic trust techniques, TCE values are not so active to properly handle altered data by misbehavior node data size, which may be a possibly malicious vehicle forwarding fake information to the destination vehicle. From Table 3, our proposed methodology of VANSec shows that our scheme is 11.6% and 7.3% more efficient in terms of TCE than the LT and trust schemes are, respectively, while the trust scheme is 4.3% more efficient in terms of TCE than LT. The enhancement in the performance of VANSec is due to the fact that our model calculates trust for all nodes randomly and identifies malicious node from their negative feedback. VANSec performed well in the presence of a huge number of false or malicious node concentrations. The reason for the good performance in a malicious environment is the feature of feedback metric credibility in the VANSec algorithm.

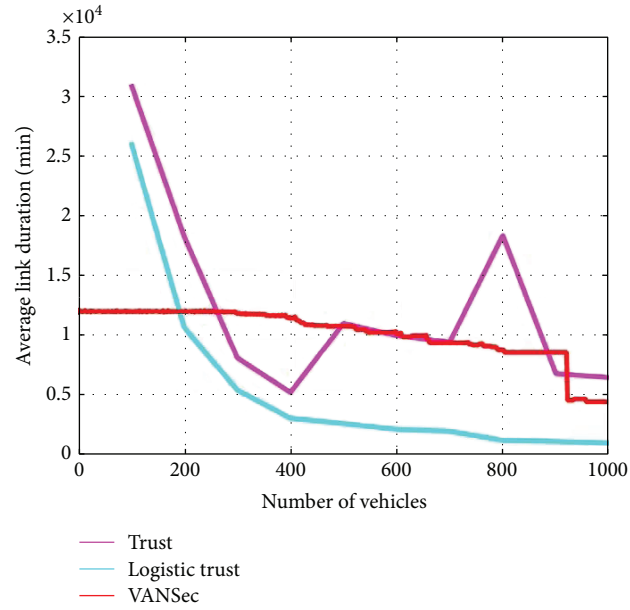

Figure 6: Average link duration (minutes) versus number of vehicles.

6.2. End-to-End Delay. The time taken by FSAMs to travel in a VANETs/VANSec model from the source vehicle to the destination vehicle is called end-to-end delay. Due to high mobility scenarios in VANSec, on-time delivery of FSAMs may be delayed. To prevent latency in packet delivery, delay-tolerant networks (DTNs) are favored to be used, in order to minimize end-to-end delay in VANETs. Figure 5 depicts that the performance of the VANSec algorithm is better than trust and logistic trust techniques. Figure 5 and Table 4 show close consistency along with an increase of 200 vehicles in each step. The table values for VANSec with the increase in number of vehicles also depict a consistent reduction in packet end-to-end latency.

Such coherent gradual reduction in end-to-end delay declares VANSec more logical than trust and logistic trust approaches. It is clearly depicted from the table that there is

Table 5: Average link duration (minutes) per 200 vehicles.

Protocol	200 v	400 v	600 v	800 v	1000 v	Average	% improvement
VANSEC	1.20	1.139	1.008	0.8775	0.4438	0.9337	2.594
Trust	1.06	0.3062	0.2139	0.1217	0.0978	0.3599	1.00
L. trust	1.824	0.5221	0.9957	1.833	0.6466	1.1642	3.234

no such consistency in the values of EED which are recorded with the increase in number of vehicles. From Table 4, it is concluded that average EED delay in the case of VANSec technique is approximately 0%. The trust and LT schemes face 57.6% and 5.2% longer delay, respectively, than the VANSec algorithm does, whereas the trust scheme has 52.4% more EED than the LT scheme does.

So, from these simulation results, the VANSec algorithm has enormous performance rather than trust and LT techniques. VANSec's outperformance than the rest of the two algorithms is due to the fact that our scheme considerably needed less information about the network behavior and route discovery process, which remarkably reduced the network overhead and suggested best for dynamic and ascendable networks.

6.3. Average Link Duration. Average link duration is the communication link lifespan estimation established among source and destination vehicles to exchange FSAMs. In VANETs, a path choice is an important parameter for good performance and better data rate. But in VANETs, link duration depends on various parameters like transmission range of the vehicle, intervehicle distance, vehicle density, and vehicle velocity which made link duration stability a challenging job. We used average link duration because link duration depends on the verity of parameters.

Figure 6 depicts our scheme VANSec to be more stable and reliable. Also, Table 5 reveals that our proposed scheme has stable link duration. For each step, there is a uniform increase in number of vehicles of 200 vehicles per step. From Table 5, we concluded that our designed VANSec technique provides 29.7% and 7.8% more reliable and stable ALD than trust and LT techniques, respectively. However, LT ALD is 21.9% more than the trust algorithm. So, an increase in the number of vehicle VANSec preserves link stability and very little gradual change noticed in the average link values. It means that ALD in the VANSec scheme is more reliable and stable.

However, the remaining schemes trust and LT undergo sudden change in ALD with increase in vehicle density and small consistency which are observed in ALD values. So comparison results show that our proposed VANSec scheme has better efficiency in terms of average like duration, and very little packets are lost. Such ambiguity in our VANSec protocol's better efficiency is that our algorithm chooses and prefers more stable and reliable routes/links among nodes for data transmission which has high link stability timing interval.

6.4. Normalizing Routing Overhead. Normalized routing overhead is a ratio of transmitted routing packets divided by the number of data packets delivered at the destination node. Figure 7 depicts an overhead returned by VANSec, trust, and logistic trust. Effects of overhead of these schemes are shown with the increase in vehicle density, respectively, depicted in Figure 7 and Table 6.

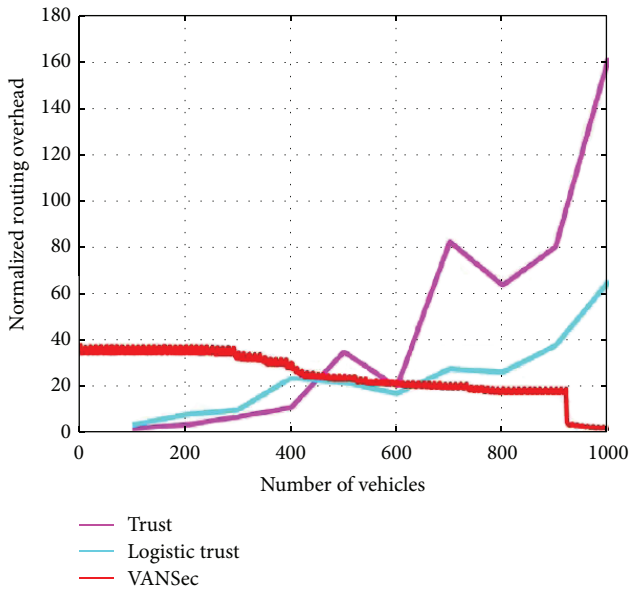

Figure 7: Normalized routing overhead versus vehicle density.

In Figure 7, the vehicle's density is adjusted at 1000 vehicles. We notice that our algorithm VANSEC has significant reduction in load with an increase in number of vehicles. In the VANSec scheme, overhead/load gradually reduces with the increase in vehicle density, while in other two algorithms, overhead enormously increases with increase in number of vehicles.

From Figure 7 and Table 6, it is concluded that overhead recorded in VANSec is nearly 0%, while trust and LT schemes in comparison with VANSec face 27.5% and 14% more NRO overhead, respectively; also, trust has 13.5% more load or NRO than LT does. So, in conclusion, VANSec is 27.5% and 14% more efficient than trust and LT protocols, respectively.

The particular improvement in our scheme is due to the fact that our designed scheme considerably reduces route request (RReq) query to conceive routes and choose the most stable and reliable route for transmission of data packets. This results in minimal route failure and considerably small number of control messages; that is, overhead is required to detect a route for information exchange. Table 6 shows a gradual reduction in NRO values with 200 increase in vehicle

Table 6: Normalized routing overhead per 200 vehicles.

Protocol	200 v	400 v	600 v	800 v	1000 v	Average	% improvement
VANSec	34.53	28.01	21.07	16.63	1.94	20.5	1.00
Trust	1.781	14.39	54.07	143.6	178.8	78.53	3.83
L. trust	7.028	17.8	21.85	35.61	47.7	26.1	1.28

density per step, while trust and LT procedures favor sudden change in NRO with 200 increase in vehicle density per step. From this analysis, our scheme outperforms the rest of the two schemes.

7. Conclusion

VANET is a subclass and an application of MANETs. Early VANET networks were a car-to-car (C2C) communication network basically designed for data exchange among vehicles. Later on, the feature of vehicles to roadside infrastructure were also added to the VANET network to make the system more efficient for data exchange to ensure safety of vehicles and humans and avoid unpleasant situations. VANET is a building key block of the ITS framework also known as intelligent transportation networks (ITNs). VANET is basically a design for the disseminations of cooperative awareness messages (CAMs) in the network for long distances among the vehicles and RSUs in range. For V2V communication, the IEEE 1609 WAVE protocol stack was designed on IEEE 802.11p WLAN standard utilizing a frequency band of 5.9 GHz for DSRC. Researchers proposed the verity of routing schemes aiming at enhancing the performance of vehicle information interchange among source and destination vehicles in the VANET system by taking into account various performance parameters. From comparison of different routing algorithms, we demonstrated that if a scheme is better in one response, it faces certain challenges in another response.

To avoid hazardous circumstances, FSAMs or any other emergency messages required priority based on time dissemination among vehicular nodes and roadside infrastructure and assurance of its flawless delivery at a receiving node is a most critical task. In case of such critical situation link failure occurs, the packets of FSAMs may face delay and once can face the worst tragic situation in sense of loss of precious lives and property.

In our research work, we have studied a variety of routing techniques including but one an analysis of designed technique VANSec, with already existing techniques trust and logistic trust in terms of different performance metrics like TCE, ALD, EED, and NRO with respect to an increase in vehicle density. VANSec is compared with trust and LT schemes because the modelling done in our scheme and the parameters considered closely match with the environment catered in those schemes along with the same parameters taken. In terms of performance metric TCE, VANSec is 11.6% and 7.3% efficient than LT and Trust are, respectively, while the trust scheme is 4.3% efficient than LT. From the EED comparison, we found VANSec to be 57.6% more efficient than trust and 5.2% than LT; also, trust schemes faced 52.4% more delay than LT did. Similarly, in terms of ALD, VANSec provides 29.7% and 7.8% more stable link duration than trust and LT did; however, LT is 21.9% more efficient ALD than trust. In terms of NRO, our proposed VANSec protocol has 27.5% and 14% lesser load than trust and LT, while trust has approximately 13% more NRO than LT. From these observations, we concluded that performance of our designed scheme in terms of these parameters is more valuable and authentic than the trust and LT algorithms. Our research shows that the VANSec scheme has better stability period, less latency, and improved data rate over trust and LT schemes.

Data Availability

No such data exists for our research; results are simulation based.

Disclosure

This work is an extension of our already published paper in conference "ARV2V: Attack Resistant Vehicle to Vehicle Algorithm for Trust Computation Error in VANETs."

Conflicts of Interest

The authors declare that they have no conflicts of interest.

References

[1] D. Puccinelli and M. Haenggi, "Wireless sensor networks: applications and challenges of ubiquitous sensing," *IEEE Circuits and Systems Magazine*, vol. 5, no. 3, pp. 19–31, 2005.

[2] M. A. Matin and M. M. Islam, "Overview of wireless sensor network," in *Wireless Sensor Networks - Technology and Protocols*, IntechOpen, 2012.

[3] O. Altintas, F. Dressler, F. Hagenauer, M. Matsumoto, M. Sepulcre, and C. Sommery, "Making cars a main ICT resource in smart cities," in *2015 IEEE Conference on Computer Communications Workshops (INFOCOM WKSHPS)*, pp. 582–587, Hong Kong, 2015, IEEE.

[4] D. Patel, M. Faisal, P. Batavia, S. Makhija, and M. Mani, "Overview of routing protocols in VANET," *International Journal of Computer Applications*, vol. 136, no. 9, pp. 4–7, 2016.

[5] V. Duduku, V. Ali Chekima, F. Wong, and J. A. Dargham, "A survey on routing protocols in vehicular ad hoc networks," *International Journal of Innovative Research in Computer and Communication Engineering*, vol. 3, no. 12, 2015.

[6] M. J. Piran, G. Rama Murthy, G. Praveen Babu, and E. Ahvar, "Total GPS-free localization protocol for vehicular ad hoc and sensor networks (VASNET)," in *2011 Third International*

Conference on Computational Intelligence, Modelling & Simulation, pp. 388–393, Langkawi, Malaysia, 2011, IEEE.

[7] M. N. Rajkumar, M. Nithya, and P. HemaLatha, "Overview of VANETs with its features and security attacks," *International Research Journal of Engineering and Technology*, vol. 3, no. 1, 2016.

[8] A. Luckshetty, S. Dontal, S. Tangade, and S. S. Manvi, "A survey: comparative study of applications, attacks, security and privacy in VANETs," in *2016 International Conference on Communication and Signal Processing (ICCSP)*, pp. 1594–1598, Melmaruvathur, India, 2016, IEEE.

[9] R. Barskar and M. Chawla, "Vehicular ad hoc networks and its applications in diversified fields," *International Journal of Computer Applications*, vol. 123, no. 10, pp. 7–11, 2015.

[10] A. Jain and D. Sharma, "Approaches to reduce the impact of DOS and DDOS attacks in VANET," *International Journal of Computer Science*, vol. 4, no. 4, 2016.

[11] A. Suman and C. Kumar, "A behavioral study of Sybil attack on vehicular network," in *2016 3rd International Conference on Recent Advances in Information Technology (RAIT)*, pp. 56–60, Dhanbad, India, 2016, IEEE.

[12] R. Boon, *Post-Accident Analysis of Digital Sources for Traffic Accidents*, University of Twente, Enschede, Netherlands, 2014.

[13] S. Gupte and M. Younis, "Vehicular networking for intelligent and autonomous traffic management," in *2012 IEEE International Conference on Communications (ICC)*, pp. 5306–5310, Ottawa, ON, Canada, 2012, IEEE.

[14] C.-T. Li, M.-S. Hwang, and Y.-P. Chu, "A secure and efficient communication scheme with authenticated key establishment and privacy preserving for vehicular ad hoc networks," *Computer Communications*, vol. 31, no. 12, pp. 2803–2814, 2008.

[15] H. Liu, Y. Chen, H. Tian, T. Wang, and Y. Cai, "A novel secure message delivery and authentication method for vehicular ad hoc networks," in *2016 First IEEE International Conference on Computer Communication and the Internet (ICCCI)*, pp. 135–139, Wuhan, China, 2016, IEEE.

[16] P. Wararkar and S. S. Dorle, "Transportation security through inter vehicular ad-hoc networks (VANETs) handovers using RF trans receiver," in *2016 IEEE Students' Conference on Electrical, Electronics and Computer Science (SCEECS)*, pp. 1–6, Bhopal, India, 2016, IEEE.

[17] M. N. Mejri and J. Ben-Othman, "GDVAN: a new greedy behavior attack detection algorithm for VANETs," *IEEE Transactions on Mobile Computing*, vol. 16, no. 3, pp. 759–771, 2017.

[18] W. Li and H. Song, "ART: an attack-resistant trust management scheme for securing vehicular ad hoc networks," *IEEE Transactions on Intelligent Transportation Systems*, vol. 17, no. 4, pp. 960–969, 2016.

[19] Y. Agarwal, K. Jain, and O. Karabasoglu, "Turning conventional vehicles in secured areas into connected vehicles for safety applications," in *2016 IEEE Information Technology, Networking, Electronic and Automation Control Conference*, pp. 538–542, Chongqing, China, 2016, IEEE.

[20] Mujeeb Ur Rehman, Sheeraz Ahmed, Sarmad Ullah Khan, Shabana Begum, and Atif Ishtiaq, "ARV2V: Attack resistant vehicle to vehicle algorithm, performance in term of end-to-end delay and trust computation error in VANETs," in *2018 International Conference on Computing, Mathematics and Engineering Technologies (iCoMET)*, pp. 1–6, Sukkur, Pakistan, 2018, IEEE.

[21] A. S. Al Hasan, M. Shohrab Hossain, and M. Atiquzzaman, "Security threats in vehicular ad hoc networks," in *2016 International Conference on Advances in Computing, Communications and Informatics (ICACCI)*, pp. 404–411, Jaipur, India, 2016, IEEE.

[22] M. N. Mejri, N. Achir, and M. Hamdi, "A new security games based reaction algorithm against DOS attacks in VANETs," in *2016 13th IEEE Annual Consumer Communications & Networking Conference (CCNC)*, pp. 837–840, Las Vegas, NV, USA, 2016, IEEE.

[23] C. A. Kerrache, A. Lakas, and N. Lagraa, "Detection of intelligent malicious and selfish nodes in VANET using threshold adaptive control," in *2016 5th International Conference on Electronic Devices, Systems and Applications (ICEDSA)*, pp. 1–4, Ras Al Khaimah, UAE, 2016, IEEE.

[24] K. Rostamzadeh, H. Nicanfar, S. Gopalakrishnan, and V. C. M. Leung, "A context-aware trust-based communication framework for VNets," in *2014 IEEE Wireless Communications and Networking Conference (WCNC)*, pp. 3296–3301, Istanbul, Turkey, 2014.

[25] S. Ahmed and K. Tepe, "Misbehaviour detection in vehicular networks using logistic trust," in *2016 IEEE Wireless Communications and Networking Conference*, pp. 1–6, Doha, Qatar, 2016, IEEE.

[26] S. Ahmed and K. Tepe, "Evaluating trust models for improved event learning in VANETs," in *2017 IEEE 30th Canadian Conference on Electrical and Computer Engineering (CCECE)*, pp. 1–4, Windsor, ON, Canada, 2017, IEEE.

Hindawi
Journal of Sensors
Volume 2018, Article ID 6924094, 7 pages
https://doi.org/10.1155/2018/6924094

Research Article

Useful Piezoelectric Sensor to Detect False Liquor in Samples with Different Degrees of Adulteration

Luis Armando Carvajal Ahumada,[1,2] **Andrés Felipe Sandoval Cruz**,[1] **Mario Alejandro García Fox**,[1] **and Oscar Leonardo Herrera Sandoval**[1]

[1]*Facultad de Ingeniería y Ciencias Básicas, Universidad Central, Bogotá 110311, Colombia*
[2]*Servicio Nacional de Aprendizaje (SENA), TecnoParque nodo Bogotá, Bogotá, Colombia*

Correspondence should be addressed to Luis Armando Carvajal Ahumada; lcarvajala1@ucentral.edu.co

Received 12 March 2018; Revised 10 May 2018; Accepted 15 May 2018; Published 9 July 2018

Academic Editor: Alfonso Salinas-Castillo

The main objective of this article is to demonstrate by experimental measurements the capability of the quartz crystal resonator (QCR) to characterize samples of liquor at different concentrations of adulteration with methanol, classify them according to their viscosity, and identify how to use this capability as a potential detection of fake liquor. According to the literature, the fake liquor is a common problem detected in several countries across the globe. The current strategy to detect the fake liquor is based on a piezoelectric biosensor that permits the classification of the samples according to its viscosity. The viscosity is a useful variable to determinate the degree of adulteration in the liquor samples because the viscosity value between ethanol (straight liquor) and methanol (most common fake liquor) is very different.

1. Introduction

The adulterated alcohol or "fake alcohol" is a common problem detected in some countries. For instance, in the UK, the illegal alcohol is distilled and sent without a license, and its sale costs the UK around £1.2 billion per year [1]. In Greece, the improvised production of beverages named "meth" exists, done in illegal laboratories in an empirical way. The production commonly includes illegal alcohol with high concentration of methyl alcohol [2]. In India, there is a similar situation related to the illicit liquor. In these cases, one dangerous adulterant is industrial methylated spirit, which causes mass poisoning of consumers [3]. Moreover, in Czech Republic, the Czech food safety authority informed the public of persons suffering from methanol poisoning after having consumed "on tap" spirits. The product was unlabeled and supplied "in bulk" in plastic barrels [4].

In particular, the Colombian case is not an exception. Studies performed by Colombian entities such as Externado University and the National Association of Industrialists (ANDI) reveal that the adulteration and falsification of locals have reached at 21% of the total offer. Javeriana University in another study concluded that one of each four bottles of liquors sold in Colombia has been falsified or adulterated. Moreover, Antioquia University from Colombia performed a study in which they observed that close to 50% of the liqueurs which are marketed in the Department of Antioquia, Colombia, are illegal, adulterated, or contraband [5].

In most cases, the commercial liquor is adulterated using methanol [1, 3–5], due to its low cost, and some physical characteristics are similar to those of the ethanol. Methanol (CH3OH) is an alcohol that is aliphatic, liquid, colorless, and volatile to room temperature. By itself, it is harmless, but its metabolites are extremely toxic. The methanol in industrial products, laboratories, and household products is commonly used. However, there is also a clandestine use like substituting of ethanol in alcoholic drinks. Although the intoxication may occur through the respiratory system or transdermally, in most cases, the exposition to methanol is through the oral way [6].

According to the "Report of the event notification for acute poisoning by chemical substances up to the epidemiological period XI" in 2010, out of a total of 23,844 reported intoxications, there were a total of 282 cases of methanol intoxication and 10 deaths, with a percentage of 1.18% and an incidence of 0.62 per one hundred thousand inhabitants. During 2011, 351 cases of methanol intoxication and 7 deaths were reported. Moreover, there is a high notification of consumption in the age ranging between 10 and 24 years [7]. A report of FND (National Federation of Departments) reveals that, of the percentage of illegal liquor (24%), the 70% correspond to adulterated drinks [4].

Although some cases of intoxication by methanol are due to suicide attempts, many times, the intoxication is caused by adulterated alcohol, which generally is distributed in bottles with labels very similar to those of the original drink but with methanol mixed to the original liquor. Therefore, the adulterated drink is not detectable to naked eye [2].

The symptoms, depending on the affected system, when ingesting adulterated alcohol are [8]

(i) nausea, vomiting, abdominal pain, and later-case affections in the pancreas (gastrointestinal system),

(ii) associated manifestations of neurologic type, which in cases of lack of treatment or late detection end in a coma state (central nervous system),

(iii) decreased visual acuity until irreversible blindness due to atrophy of the optic nerve, indicating ocular involvement and representing an advanced development of the intoxication.

According to the descriptive study of methanol intoxications reported in SIVIGILA 2010-2011 in Colombia [9], when the methanol is absorbed, it undergoes oxidation processes in the organ receptor which is the liver. The enzyme responsible for this transformation is the alcohol dehydrogenase, which oxidizes it to formaldehyde, and this in turn is oxidized to formic acid (responsible for blindness) by the aldehyde dehydrogenase. The treatment generally used to treat adulterated alcohol intoxication is based on the use of ethyl alcohol to prevent the formation of toxic methanol metabolites [9].

In accordance with the problematic presentation, several techniques have been developed with the aim of detecting the adulterated liquor. The more typical laboratory techniques are the nuclear magnetic resonance spectroscopy with multivariate analysis [4] and near-infrared spectrometry (NIR) [10]. However, these techniques do not have possibilities to be used outside of the laboratory.

In Colombia, different strategies have been generated to detect the illegal liquor, divided into contraband and fake liquor cases; several years ago, for the detection of adulterated liquor, the monitoring and control program of alcoholic beverages was implemented, led by the ANDI (National Association of Industrialists) and the Ministry of Health and Social Protection with the participation of the national police, making presence in factories, warehouses, and liquor stores. For factories and warehouses, there are four visits per year, and for liquor stores, there are three visits. In these visits, the authorities make sure for sanitary conditions of the places and take random samples of a suspect batch of liquor, where these samples cannot be less than 1 liter or a bottle generally 750 cc. The first step in this process is to check the security seals and the label, the second step is to look for suspended solids inside the bottle, and the last step is to carry the sample to the corresponding authority lab and make physiochemical tests [5].

In this work, the use of a sensor based on a quartz crystal resonator in order to identify adulterated liquor in a simple and low cost-way is proposed. This sensor is capable of operating as a microviscometer knowing the density of the liquid to be analyzed [11–15]. Samples at different "levels of adulteration" have been used to get results that confirm the difference between an original alcoholic drink and adulterated one with methanol in different concentrations.

2. Theory

The piezoelectric sensors are considered highly efficient sensing systems not only because of their low manufacturing cost but also because of their high accuracy, biofunctionalization capacity, sensitivity, and reliability in measuring the deposited sample, either gaseous or liquid media [11].

In particular, the quartz crystal resonator (QCR) is a piezoelectric transducer sensitive to the deposition of rigid mass or liquids in contact with its surface (active electrode). The QCR is composed of two electrodes that are stimulated with AC voltage, and in consequence, the crystal vibrates. The crystal has a natural frequency of resonance that depends on its geometry and thickness; as a result, when the crystal is stimulated with a signal whose frequency is close to its natural resonance, the vibration increases. This phenomenon is visible by analyzing the behavior of the admittance or impedance of the crystal in the frequency domain [11, 16, 17].

When the mass or liquid sample is deposited on the crystal surface, its resonance frequency changes in accordance with two equations: Sauerbrey for mass deposition (1) and Kanazawa for fluid deposition (2).

$$\Delta f = -\frac{2 f_0^{\,2}}{A\sqrt{\rho_q G_q}}\Delta m, \tag{1}$$

$$\Delta f = -\sqrt{n} f_0^{\,3/2}\sqrt{\frac{\rho_L \eta_L}{\pi \rho_q G_q}}, \tag{2}$$

where ρ_q and G_q are the specific density and the shear modulus of quartz, respectively; f_0 is the fundamental resonance frequency of the quartz, related to its thickness, and Δm is the thin film of mass deposited; A is the piezoelectrically active crystal area; ρ_L and η_L are the density and viscosity of the fluid, respectively; and n is the overtone number [11].

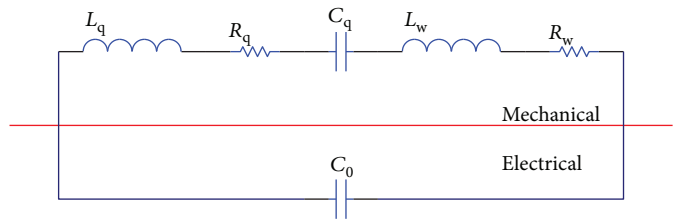

Figure 1: Basic electrical model (BVD) for QCM with liquid sample deposited.

In addition to Sauerbrey and Kanazawa equations, the quartz crystal behavior can be modeled as an electrical resonator circuit [11, 16, 17].

The electric model (BVD), shown in Figure 1, explains this phenomenon as an addition of impedance depending on the type of sample. For liquids in contact with the crystal, the equivalent impedance is an inductance and a resistance which are in series.

The value of this impedance is related to the characteristics of the samples according to the following equations:

$$
\begin{aligned}
C_q &= \frac{8{e_{26}}^2 A}{(N\pi)^2 \overline{C_{66}} h_q},\\
L_q &= \frac{1}{{\omega_s}^2 C_q},\\
R_q &= \frac{\eta_q}{\overline{C_{66}} C_q},\\
L_w &= \frac{\omega_s L_q}{N\pi}\left(\frac{2\rho_L \eta_L}{\omega_s \overline{C_{66}} \rho_q}\right),\\
R_w &= \frac{\omega_s L_q}{N\pi}\left(\frac{2\omega_s \rho_L \eta_L}{\overline{C_{66}}\, \rho_q}\right),\\
C_0 &= \frac{\varepsilon_{22} A_e}{h_q},
\end{aligned}
\tag{3}
$$

where $\overline{C_{66}}$ is the piezoelectrically stiffened elastic constant for loss-less quartz ($2947 \times 1010\,\mathrm{N/m^2}$), e_{26} is the piezoelectric stress constant for quartz ($953 \times 103\,\mathrm{A{\cdot}s/m^2}$), ε_{22} is the quartz permittivity ($3.982 \times 10^{-11}\,\mathrm{A^2{\cdot}s^4/kg{\cdot}m^{-3}}$), A is the active electrode area ($\mathrm{m^2}$), h_q is the quartz crystal thickness (m), η_q is the effective viscosity of quartz ($3.5 \times 10^{-4}\,\mathrm{kg/m{\cdot}s}$), and ω_s is the series resonance frequency ($2\pi F_s$). For the liquid, ρ_L and η_L are the density of the liquid sample ($\mathrm{kg/m^3}$) and the viscosity of the liquid sample (kg/m·s), respectively [17].

Figure 2 shows the conductance behavior (Geq) for the unperturbed crystal (kept in air) and the crystal in contact with liquid. The maximum value of conductance takes place in the frequency of resonance.

According to theoretical models, when the crystal electrode is in contact with liquid samples, the conductance curve changes, moving to the left in the axis of frequency, increasing its bandwidth and decreasing its conductance magnitude (Figure 2).

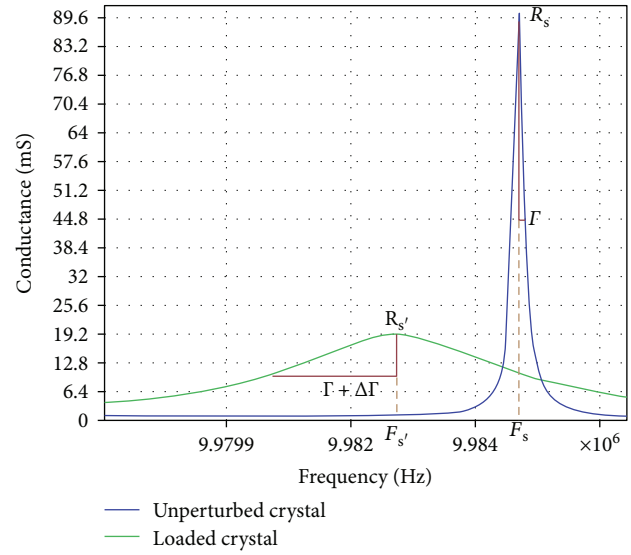

Figure 2: Conductance behavior for a QCM with and without the sample [12].

The values of ΔF and $\Delta\Gamma$ represent the changes in the behavior of the crystal due to the properties of the sample, and these are obtained using

$$
\begin{aligned}
\Delta F &= F_{s'} - F_s,\\
\Delta\Gamma &= \Gamma' - \Gamma,\\
\Delta R_s &= \frac{R_{s'}}{R_s}.
\end{aligned}
\tag{4}
$$

3. Materials and Methods

3.1. Samples. The experiments were done with seven adulterated samples and three references; the commercial liquor (Ron) was purchased in a local market. It has 35% *v*/*v* of alcohol concentration and was used as one of the three references for the quartz crystal resonator (QCR) system. The other two references were ethanol (99.8% *w*/*w*, Merck) and methanol (99.8% *w*/*w*, Merck). The commercial liquor was adulterated in the Central University laboratory, but its alcohol concentration was kept, by addition of deionized water and methanol in levels of 10%, 25%, 35%, 50%, 55%, 65%, and 75% *v*/*v* to the pure commercial liquor (Figure 3).

Only 50 μL of volume of the sample was deposited in a uniform layer on the surface of the electrode of quartz crystal

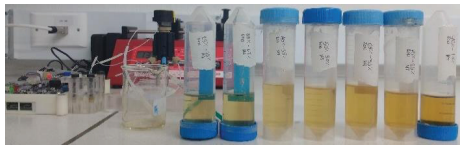

Figure 3: Samples at different concentrations elaborated in the Central University chemical lab.

to be analyzed. The deposition has been achieved using a microfluidic system.

3.2. Crystals and the Holder Cell. The 10 MHz quartz crystals were purchased from International Crystal Manufacturing. According to the manufacturer, the crystal diameter is 13.66 mm, the electrode diameter is 5.1 mm, and the crystal thickness is 167 μm.

The holder cell has been designed and built in the mechanical laboratories at Central University in Bogotá, Colombia.

Figures 4(a)–4(c) show the crystal plate and the fluidic cells designed for depositing the fluid sample over the crystal electrode using a pressure pump. This technique permits the obtainment of measures related to the behavior of the crystal and the deposition of the samples with a constant flux without the need to manipulate the crystal. In this way, the reference measure is conserved. The sealing system is based on magnets, and the magnets permit a very reliable sealing and an easy way to open and close the cell.

3.3. QCR System. The development of the QCR system has been based on Nakamoto and Kobayashi's proposal [18]. In particular, the proposed circuit gets the voltage and current signal in the crystal for several frequencies in a configurable bandwidth close to the crystal resonance frequency (f_s) indicated by the manufacturer (10 MHz in the current study). The current system is connected to a laptop using a software interface designed in Labview in order to control the sensor and to acquire and to visualize the signals.

All systems have been developed by the coworker team, and all technical details for the measurement system and methods to obtain the changes in the admittance curve (f_s and Γ) are described in [11, 12].

Figure 5(a) shows the current QCR prototype system. In future work, the prototype will be miniaturized with the aim of increasing the portability of the system, so the user can analyze the sample in any place.

Figures 5(a) and 5(b) show the microfluidic system that was used on the experiments. The system consists of two syringe pumps: the first pump injects the buffer liquid on the fluidic system and the second pump injects the sample on the fluidic system. The sample has to pass through a loop where it is stored and waits for the valve activation; when that happens, the sample can pass through the crystal.

3.4. Viscosity of the Reference. For this work, the reference viscosity values have been obtained using the viscometer Fungilab Smart (Figure 6) and the spindle LCP because the samples have low viscosity range.

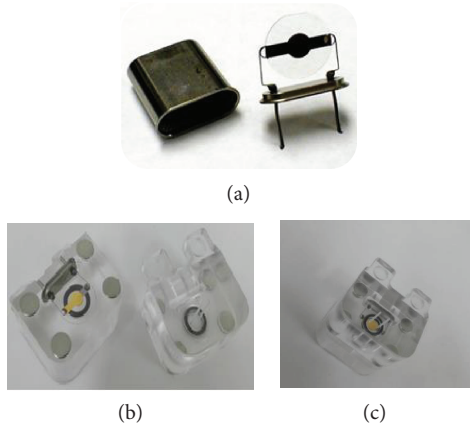

(a)

(b) (c)

Figure 4: (a) Crystals used in experimental tests, (b) holder developed (fluidic cells in parts), and (c) holder developed (fluidic cells assembled).

3.5. Measurement Protocol. The measurement protocol is as follows: to configure the frequency sweep using the system interface (frequency range, sweep step, and number of cycles) and to calculate the series resonance frequency (F_0) and the half-band half-width (Γ_0) using the developed code in Labview for each cycle. These measures are taken ten times for the bare crystal. The final values are the averages of the ten measures. To put the sample for analysis on the electrode surface of the quartz crystal (50 μL of volume), the microfluidic system has been used. The frequency range in the user interface needs to be adjusted in order to obtain the admittance values of the quartz crystal in contact with the liquid sample. Due to the sample effect, the curves are shifted in the frequency axis. For the results obtained in this work, the measures with the sample (F_s, $F_{r'}$, Γ_s, and $R_{s'}$) are taken 100 times (ca. 3 minutes) and the final values are the averages of the measures. To obtain $\Delta F_s = F_s - F_0$ and $\Delta\Gamma = \Gamma_s - \Gamma_0$. The density values were obtained using an analytical balance. The mass of each solution was found from 1 mL of its volume.

3.6. Cleaning Protocol. Before each experiment, the sensor crystal was cleaned in 96% acetone and 99.5% isopropyl alcohol for 5 min each; then, it is rinsed with Milli-Q water and dried in air.

4. Results and Discussion

According to the measurement process described in Materials and Methods, the results obtained are the following:

Figure 7 shows the behavior of ΔF_s and $\Delta\Gamma$ for each sample of adulterated alcohol. According to these results, the best variable to differentiate between grades of adulteration in the alcohol sample (percentage of methanol) is $\Delta\Gamma$ due to its more sensitivity (the curve slope is higher).

Table 1 shows the results for different tests done in an independent way. One hundred measures for each test have been done. The values have been averaged. In all cases, the value ($\Delta\Gamma$) decreases when the methanol quantity increases. In other words, the slopes for each test are similar to the

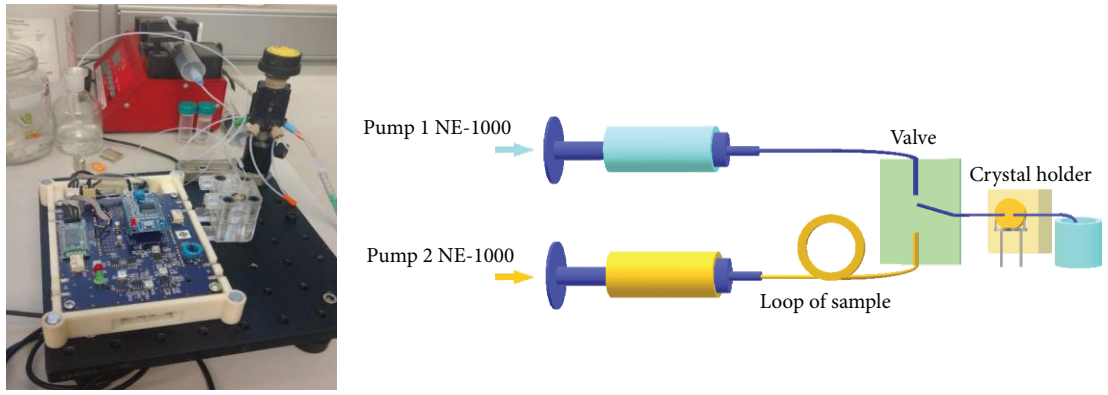

Figure 5: (a) QCR measurement system with the microfluidic system and holder cell and (b) schematic of the microfluidic system.

Figure 6: Viscometer for the reference (Fungilab Smart).

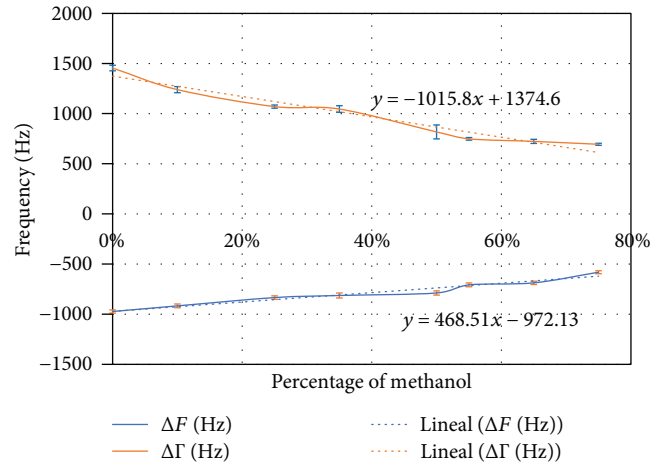

Figure 7: Changes in frequency for F_s and Γ variables for each sample.

trend (negative slope), which indicates that the results are coherent and reproducible and they have a good level of precision. According to these results, SD is less than 10% in all cases.

Figure 8 shows the resultant curve based on the average of the tests. Error bars are calculated using the standard deviation of data tests for each mixture. According to this figure, the prototype proposed can be used to determinate the degree of adulteration of each sample in a wide range. The reason for this capability is that the piezoelectric sensors (QCR) have high sensibility for viscosity changes. In particular, the adulteration process adds methanol to the liquor mixture generating a decrease in the viscosity of the liquor in relation to a legal liquor (negative slope in Figure 9). This decrease in the viscosity value (Figure 9, gray line) is related to the resonance of the quartz crystal; in this way, reading the frequency of resonance of the quartz crystal is possible, associating the change of this frequency with the change of the viscosity of the mixture.

According to Figure 9, the values obtained for all samples using the QCR sensor have been compared with those using the commercial equipment "viscometer Fungilab Smart" available in the material laboratory at Central University. Figure 9 permits the observation of the similar behavior between the results obtained with a commercial viscometer and the values obtained in the tests using the QCR sensor. The viscosity values have been found using (2) with the data shown in Figure 9. The density values were obtained using an analytical balance. The mass of each solution was determined from 1 mL of its volume.

In Figure 10, the red circle zone indicates that the QCR response is better than that of the viscometer because the Fungilab measures are very close in this range (25%–50% of adulterated mixture).

In accordance with the previous results, the prototype generates a very close response in comparison with the commercial equipment. In consequence, the data obtained are reliable. As an additional attribute, the quantity of the sample

Table 1: Results of ΔΓ for four independent tests (average ± SD). Each test contains one hundred measures.

Methanol (%)	Test 1 ΔΓ (Hz)		Test 2 ΔΓ (Hz)		Test 3 ΔΓ (Hz)		Test 4 ΔΓ (Hz)	
	Average	SD	Average	SD	Average	SD	Average	SD
0%	1374.6	27.87	1462.3	31.71	1364.6	29.51	1260.9	26.56
10%	1273.0	30.60	1368.7	33.95	1284.8	20.82	1187.3	18.06
25%	1120.7	15.72	1228.3	32.55	1165.1	104.91	1076.9	15.96
35%	1019.1	33.00	1134.8	24.98	1085.3	54.89	1003.3	34.06
50%	866.7	69.61	994.4	40.35	965.7	19.91	892.9	21.23
55%	815.9	12.94	947.6	21.22	925.8	15.86	856.1	19.26
65%	714.3	20.50	854.0	18.65	846.0	46.25	782.4	16.47
75%	612.8	10.10	760.4	14.45	766.2	21.06	708.8	41.42

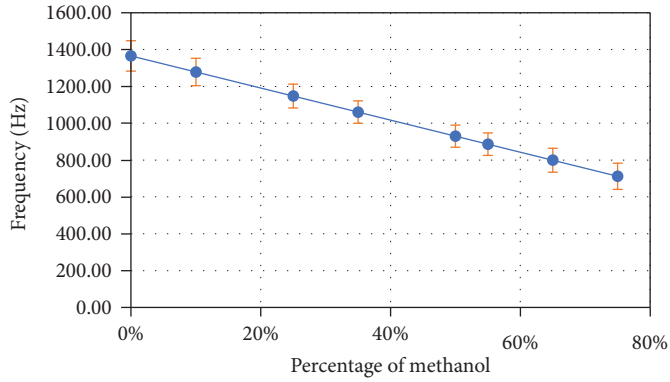

Figure 8: Average values of bandwidth shift for different independent tests.

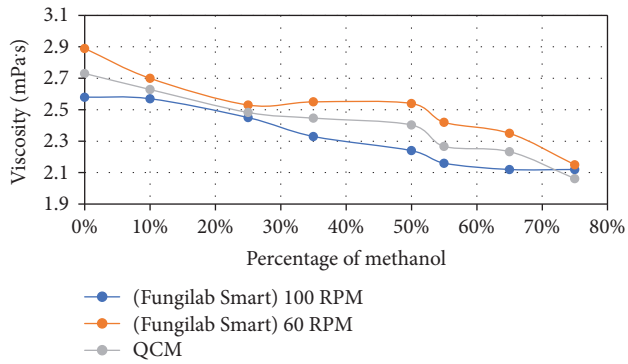

Figure 9: Comparison between the sensor QCR and Fungilab Smart.

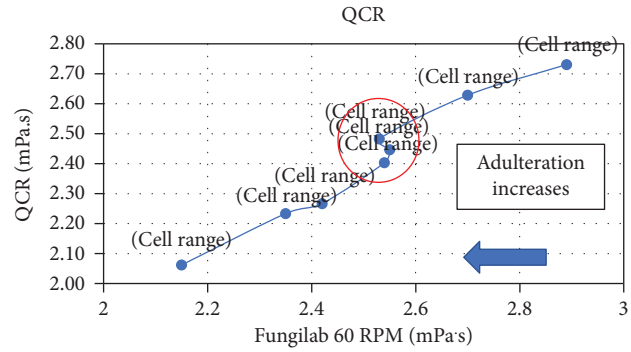

Figure 10: Comparison between the sensor QCR and Fungilab Smart.

used in the comparison between the prototype QCR and the commercial equipment is tens of microliters and tens of milliliters, respectively. In consequence, the prototype proposed is more efficient about the quantities of the samples used.

5. Conclusions

In the present work, the effectiveness of a low-cost piezoelectric sensor to detect fake liquor has been demonstrated through simple experiments. The capability of the quartz resonator to identify changes in the viscosity of liquid samples through an electronic transduction and characterization of its admittance response allows us to carry out the present study to detect in a clear way the changes in concentration of methanol in a common alcoholic drink like Ron. In consequence, this device could allow the identification of adulterated alcohol with a small amount of sample (tens of microliters).

In a future phase, the device will be optimized in size, its portability will be improved, and it will be connected to a smartphone. In addition, more tests with real adulterated liquor should be conducted with the aim of verifying the presence of minimum concentrations of methanol. The real adulterated liquor samples could be obtained through an agreement with the Colombian police.

Data Availability

Data used to support the findings of this study were supplied by Luis Carvajal under license and so cannot be made freely available. Requests for access to these data should be made to Luis Carvajal (lcarvajala1@ucentral.edu.co).

Conflicts of Interest

The authors declare that there is no conflict of interest regarding the publication of this paper.

Acknowledgments

The current investigation work has been supported by COLCIENCIAS through Grant no. 0375–2013 with project number 6570577636375 and by Universidad Central (Bogotá, Colombia) through the Research Cluster on Converging Sciences and Technologies (NBIC).

References

[1] T. Robert, *Combatting Fake, Counterfeit, and Contraband Alcohol Challenges in the United Kingdom through the Alcohol Wholesaler Registration Scheme (AWRS)*, Federal Regulatory and Compliance Consultant Falls Church, Virginia, 2017.

[2] A. Tsiboukli, "Greek crisis: impact on drug treatment services, research and population," *Nordic Studies on Alcohol and Drugs*, vol. 32, no. 3, pp. 333–337, 2015.

[3] L. Riley, M. Marshall, World Health Organization, and Dept. of Substance Abuse, *Alcohol and Public Health in 8 Developing Countries*, World Health Organization, Geneva, Switzerland, 1999.

[4] D. W. Lachenmeier, *Advances in the Detection of the Adulteration of Alcoholic Beverages Including Unrecorded Alcohol*, Elsevier Ltd, 2016.

[5] J. Zapata, A. Sabogal, A. C. Montes, G. Rodriguez, and J. Castillo, *Una Estimación de la Adulteración y la Falsificación de Bebidas Alcohólicas en Colombia*, Fedesarrollo, 2012.

[6] J. L. Castellanos, A. B. Limón, A. R. Hernández, and D. E. F. Rojas, "Intoxicación por metanol, reporte de un Caso," *Archivos de Medicina de Urgencia de México*, vol. 1, pp. 67–73, 2009.

[7] Departamento Nacional de Planeación - DNP, "Estrategia para la Implementación del Sistema Unico Nacional de Información y Rastreo -SUNIR (Documento Conpes)," *Consejo Nacional de Política Económica y Social República de Colombia*, p. 33, 2009.

[8] Methanol Institute, "Methanol FACTS: adulterated alcohol poisoning: issue summary," 2016, http://www.methanol.org/wp-content/uploads/2016/06/Adulterated-Alcohol-Issue-Summary-20160322-EN-vfinal.pdf.

[9] D. Niño and J. Velandia, *Estudio Descriptivo De Las Intoxicaciones Por Metanol Reportadas En Sivigila 2010-2011 En Colombia*, Universidad de Ciencias Aplicadas y Ambientales (UDCA), 2014.

[10] M. J. C. Pontes, S. R. B. Santos, M. C. U. Araújo et al., "Classification of distilled alcoholic beverages and verification of adulteration by near infrared spectrometry," *Food Research International*, vol. 39, no. 2, pp. 182–189, 2006.

[11] L. A. Carvajal Ahumada, N. Peña Pérez, O. L. Herrera Sandoval, F. del Pozo Guerrero, and J. J. Serrano Olmedo, "A new way to find dielectric properties of liquid sample using the quartz crystal resonator (QCR)," *Sensors and Actuators A: Physical*, vol. 239, pp. 153–160, 2016.

[12] L. Ahumada, M. González, O. Sandoval, and J. Olmedo, "Evaluation of hyaluronic acid dilutions at different concentrations using a quartz crystal resonator (QCR) for the potential diagnosis of arthritic diseases," *Sensors*, vol. 16, no. 11, p. 1959, 2016.

[13] L. A. Carvajal Ahumada, J. E. Pazos Alonso, J. J. Serrano Olmedo, and O. L. Herrera Sandoval, "Diseño y Evaluación de un micro viscosímetro de bajo costo utilizando un resonador de cristal de cuarzo y Arduino," in *Congreso Internacional de Ciencias Básicas e Ingeniería de Universidad de los Llanos*, p. 11, Asociación Mexicana de Medicina de Urgencia, 2016.

[14] E. J. Calvo, R. Etchenique, P. N. Bartlett, K. Singhal, and C. Santamaria, "Quartz crystal impedance studies at 10 MHz of viscoelastic liquids and films," *Faraday Discussions*, vol. 107, pp. 141–157, 1997.

[15] M. Pax, J. Rieger, R. H. Eibl, C. Thielemann, and D. Johannsmann, "Measurements of fast fluctuations of viscoelastic properties with the quartz crystal microbalance," *Analyst*, vol. 130, no. 11, pp. 1474–1477, 2005.

[16] M. Cassiède, J. H. Paillol, J. Pauly, and J.-L. Daridon, "Electrical behaviour of AT-cut quartz crystal resonators as a function of overtone number," *Sensors and Actuators A: Physical*, vol. 159, no. 2, pp. 174–183, 2010.

[17] V. E. Granstaff and S. J. Martin, "Characterization of a thickness-shear mode quartz resonator with multiple nonpiezoelectric layers," *Journal of Applied Physics*, vol. 75, no. 3, pp. 1319–1329, 1994.

[18] T. Nakamoto and T. Kobayashi, "Development of circuit for measuring both Q variation and resonant frequency shift of quartz crystal microbalance," *IEEE Transactions on Ultrasonics, Ferroelectrics and Frequency Control*, vol. 41, no. 6, pp. 806–811, 1994.

Hindawi
Journal of Sensors
Volume 2018, Article ID 6926594, 6 pages
https://doi.org/10.1155/2018/6926594

Research Article

Study on Attenuation Properties of Surface Wave of AE Simulation Source Based on OPCM Sensor Element

Ziping Wang[1], **Xian Xue**[1], **Xingjia Li**[1], **Zhengxuan Jiang**[1] and **Karthik Reddy**[2]

[1]*Faculty of Civil Engineering and Mechanics, Jiangsu University and National Center for International Research on Structural Health Management of Critical Components, Zhenjiang 212013, China*
[2]*Department of Mechanical & Aerospace Engineering, North Carolina State University, Raleigh, NC 27606, USA*

Correspondence should be addressed to Ziping Wang; wzpxx2004@126.com

Received 7 December 2017; Revised 13 February 2018; Accepted 28 February 2018; Published 12 April 2018

Academic Editor: Aniello Falco

It is of great significance to grasp the ultrasonic attenuation characteristics of materials for the nondestructive testing of materials. The dynamic properties of a piezoelectric composite material (OPCM) with self-developed transverse anisotropy have been analyzed using the experiment in this work. The OPCM sensor is attached to the surface of the iron plate and concrete structures to sense the surface waves generated by acoustic emission (AE). The experiment results show that OPCM sensor elements have unique advantages compared to piezoelectric ceramic materials (PZT). Further, by comparing the signals of isotropic and anisotropic materials, the attenuation characteristics of surface waves propagating in different materials are studied, and a new method for measuring the attenuation coefficient of surface waves is demonstrated.

1. Introduction

Surface waves have been widely used for damage detection in many engineering structures [1–3]. The sensors, which receive the surface waves, play an important role in damage detection. In 1885, Lord Rayleigh discovered surface acoustic waves in semi-infinite isotropic solid bodies and has since been used for signal processing techniques [4], including filtering [5], delay [6], pulse compression [7], correlation, and convolution [8]. It has been used in such fields as radar, aerospace, communications, and damage detection [9, 10]. Moreover, with the development of SAW technology, various kinds of new low-loss sensors such as Rayleigh-type SAW, shear-type SAW, and BG wave were developed. The generation and emergence of various sensor simulation theories are the conditions for the development and application of new fields of SAW sensors with excellent performance [11]. It is due to the essential characteristic of SAW that sound waves propagate along the substrate surface, making SAW sensitive to physical, chemical, or other mechanical perturbations of its surface, thereby making it possible to produce a wide variety of highly sensitive sensors [12]. The basic principle is that when the physical or chemical parameters act on the surface of a SAW transducer is changed, the disturbance of SAW propagation will cause the variation of velocity and amplitude. The corresponding damage detection signals will be recorded by SAW sensors.

In addition to good flexibility, high strength, large ultimate strain, light weight, and other advantages provided by piezoelectric materials, OPCM sensor elements have a flat cross-anisotropic characteristic that can distinguish the planar structure of various components of a stress wave [13–15]. In this study, the feasibility of frequency chosen by AE broken pencil signals was verified by testing natural frequency ranges of SAW sensors. The attenuation characteristics of surface wave generated by AE simulation source in iron and concrete plate is tested by broken lead experiments. When the sample thickness is more than 2 to 3 wavelengths, the stress waves excited on the surface of the sample are mainly Rayleigh waves, which propagate longer distances. This is because the spread of the wave attenuation is much smaller than the longitudinal and transverse

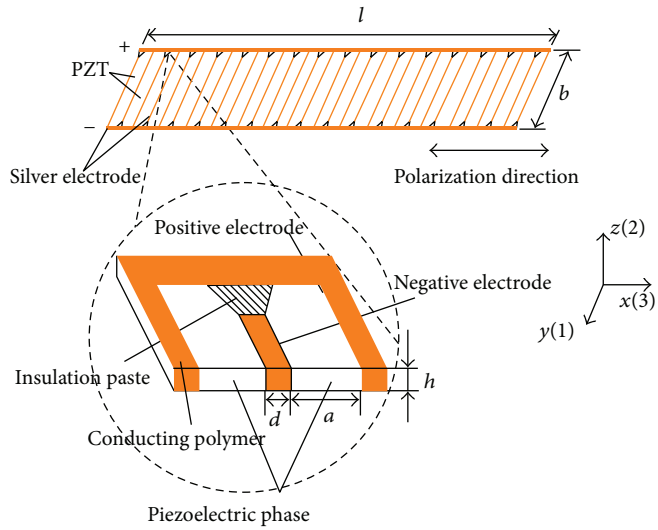

Figure 1: 1-1 OPCM sensing element structure.

Table 1: Piezoelectric ceramics' physics and electricity performance.

Density 10^3 kg/m^3	Curie temperature: ˚C	Compliance constant 10^{-12} m^2/N			Poisson's ratio	Dielectric constant		Piezoelectric constant 10^{-12} C/N			Coupling coefficient: %		
		S_{11}^E	S_{33}^E	S_{55}^E	μ	ε_{33}^σ	ε_{11}^σ	d_{31}	d_{33}	d_{15}	k_{31}	k_{33}	k_{15}
7.45	260	15	9	22	0.32	2100	2400	245	530	816	36	70	68

waves. Therefore, Rayleigh waves generated by the broken lead can be used to assess the performance of the sensor element and to analyze the attenuation characteristics effectively.

2. Dynamic Performance Analysis of 1-1 OPCM Sensor Element

The first step to construct OPCM elements is to design the piezoelectric phase of the element. Additionally, the volume ratio of the piezoelectric in the composite should be taken into account, including the effects of the elastic constants of the polymer material to impact the OPCM elements' mechanical and electric characteristics. Taking the above factors into account, the OPCM sensor element was developed [16, 17], as shown in Figure 1. The length of the OPCM sensor element l is 13.8 mm, its width b is 4 mm, and is thickness h is 0.7 mm. The electrode interval a is 1 mm, and the electrode width d is 0.1 mm. The piezoelectric phases of the OPCM sensor are cut from the same monolithic and already polarized P-51 piezoelectric ceramic plate to ensure that the piezoelectric material properties are consistent. Table 1 shows the material properties of P-51 PZT. The substrate material of DAD-40 is conductive epoxy adhesive. The shear strength at normal temperature is 14.7 MPa, and the volume resistivity is less than $1.0 \times 10^{-3}\ \Omega$ cm. The interdigitated electrodes were shown in Figure 1, and two sides of the electrode can generate opposite electric polarity. The manufacturing process of two electrodes with opposite polarities was provided. It can form a good insulation tape to prevent electrical leakage. The resistance of the insulated region, between the two electrodes, is measured, and it is found to be more than 200 MΩ.

In order to obtain the frequency response of OPCM sensor element and set the range of frequency, the oscilloscope was used to record the waveform from two different directions in the experiment. When the excitation frequency was changed point by point, the corresponding variation voltage was recorded by the oscilloscope, and then the resonant frequency of two component voltages from directions x and y with OPCM sensor element can be gotten. When the test frequency changes from 20 kHz to 400 kHz, the OPCM sensing element receives the amplitude and encrypts the measuring point when the amplitude suddenly increases. The frequency is the resonant response frequency of the sensing element in this direction. Figure 2 shows the amplitude-frequency characteristic curve obtained from the frequency and voltage testing experiment.

The resonance frequency of the OPCM sensor in direction 3 is 173 kHz. The maximum amplitude at the resonant frequency is 41 mV, while the 1-direction amplitude is low, which shows the orthotropic performance.

3. Attenuation Characteristic Experiment

3.1. Specimen Preparation. The iron plate used in the experiment is of size 1000 mm × 1000 mm × 20 mm with density of 7.8×10^3 kg/m^3, whereas the size of the standard curing concrete specimen is 700 mm × 700 mm × 200 mm, and the density is 2452 kg/m^3. The concrete specimen is prepared with the mass mixing proportion (cement : gravel : sand :

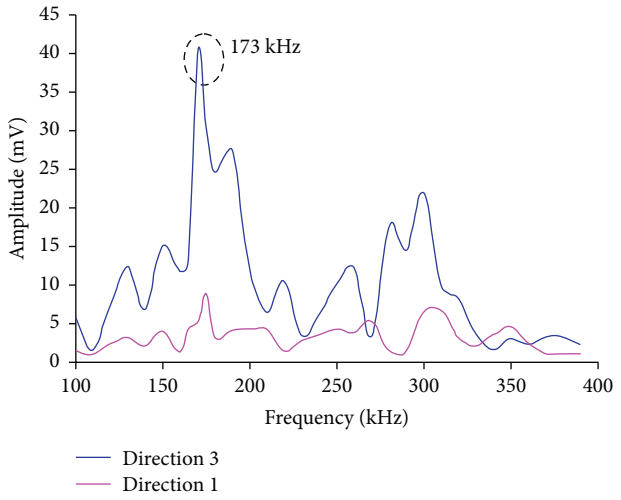

Figure 2: Amplitude-frequency curve.

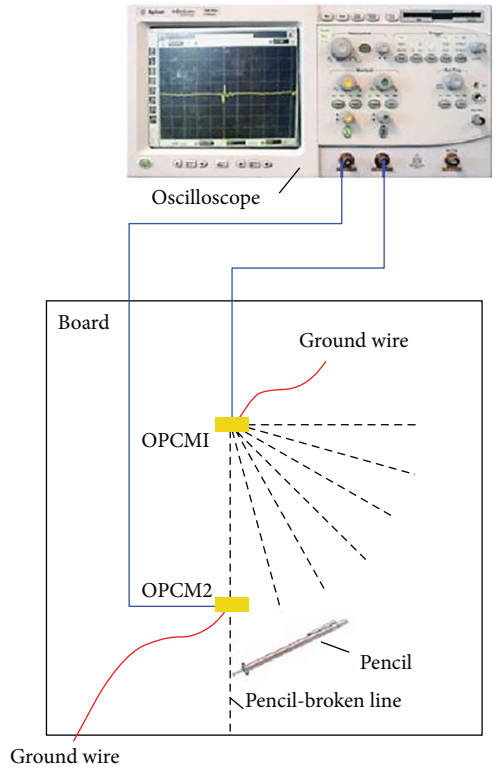

Figure 3: Experimental setup.

water) of 1 : 2.86 : 1.25 : 0.49, and the maximum size of gravel is 16 mm, and the water-cement ratio is 0.49.

The OPCM elements should be polished first before pasting it to the surfaces of the iron plate and concrete specimen with AB glue. The interval from the border is 200 mm. The HB pencil with a diameter of 0.5 mm and length of 2.5 mm is used in the broken lead experiments. The signal from the pencil broken at 30° at each measuring point simulates the AE signal in the structures.

3.2. Experiment Equipment and Experiment Content. Figure 3 shows the experimental setup used for this work. The dashed lines indicate the test lines of the polarization direction of sensing elements of the OPCM sensor. The interval of the pencile-broken points is 10 mm. The first OPCM sensor is used to test the directional performance of polarization and wave attenuation characteristic. By using a second OPCM sensor, the surface wave velocities of two materials can be calculated from the measured time difference. In this experiment, the velocity error depends on the sampling length. The Agilent54820A waveform generator, whose sampling length is set as 32768 pts and sampling frequency is set to 2.5 MHz, is used to break the pencil with band frequency from 50 kHz to 400 kHz [18] at given points along the direction of the OPCM sensor. The experimental testing setups of two kinds of plate are as shown in Figure 4.

In the test, the signals are collected from the iron plate and concrete along the direction of polarization of the OPCM sensing element and at every 15° along the direction from 0° to 90° for different lead lengths. The velocity of the surface wave was tested in the iron plate and concrete, separately.

4. Experimental Results and Discussion

4.1. Surface Wave Propagation Characteristics in Different Materials. Figure 5 shows the waveform generated from the surface of the iron and concrete specimens with SAW sensors, respectively. Three typical waveforms tested by OPCM SAW sensors were selected to analyze. The results show that the wave amplitudes were attenuated on the iron plate more regularly than that on the concrete. This is because the concrete is an anisotropic material, and particles of different sizes cause reflection and scattering. Next, the amplitudes of the concrete are smaller than those of the iron plate, and this indicates that the attenuation of the wave in concrete is faster. Figure 6 shows the spectrums of the typical waves in concrete plate that were analyzed, and it is analogous in the iron plate. The resonance frequency testing results indicates that the SAW sensor can receive pencil-broken signals with it's special frequency. The velocity of SAW can be calculated from the signal travel time difference. It is found that the surface velocity is 2958 m/s in the iron plate and 2103 m/s in the concrete material. The surface velocity values validate the correctness and feasibility to test the Rayleigh wave velocity. Before recording the signals, the pencil core must be broken at least three times to get the stable signals. The experiments are repeated for a number of times, and the surface velocity values obtained from each run are consistent with the nondispersion characteristics of Rayleigh wave, and the recorded signals are considered mainly to be Rayleigh waves.

The OPCM sensor was stuck on the surface of iron plate and concrete specimen. The signals from different angle points can be collected 200 mm away from the center of the senor. Only 20 mV amplitude peak can be received in the polarization direction (90°), and no signals are received in other directions. This phenomenon further verifies the good cross-anisotropy of the developed OPCM sensor elements.

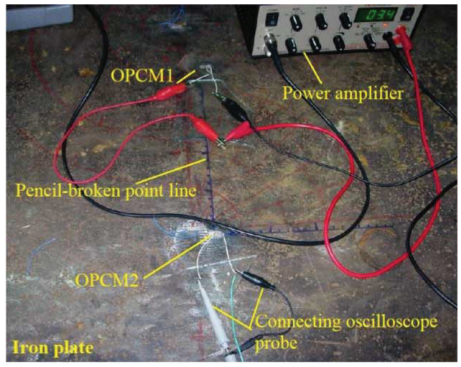

(a) Attenuation characteristic testing experimental setup of the metal plate

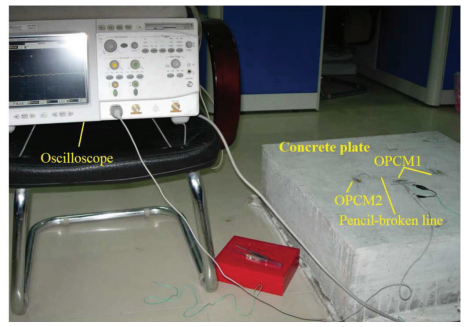

(b) Attenuation characteristic testing experimental setup of the concrete plate

Figure 4: Two kinds of plate testing sample.

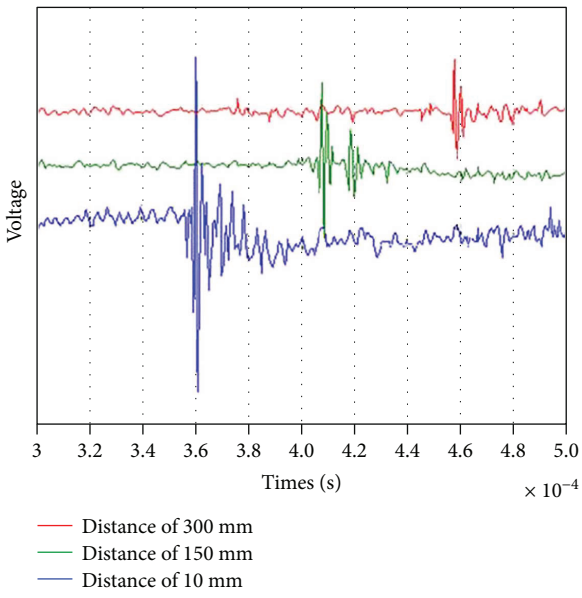

(a) Different distance waveforms in metal plate

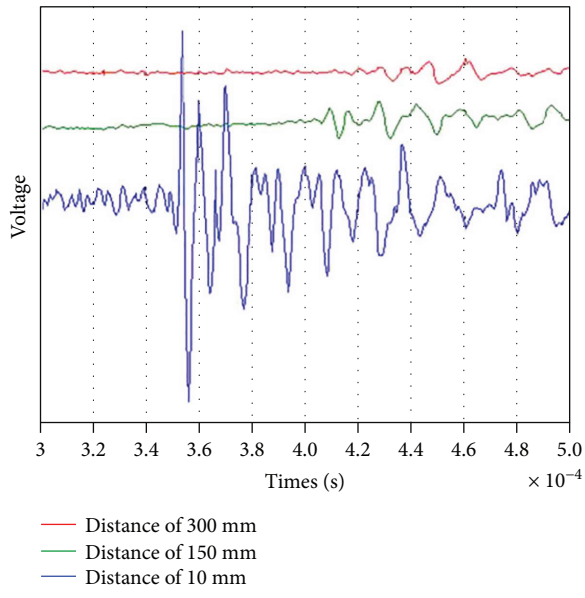

(b) Different distance waveforms in concrete plate

Figure 5: Typical waveform record in metal and concrete plates.

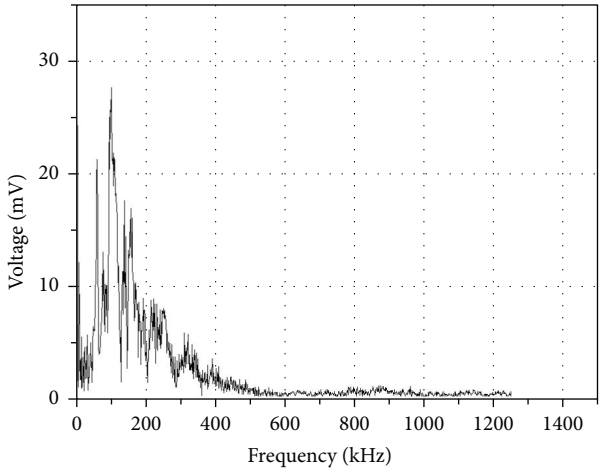

Figure 6: Spectrum analysis diagram of typical signals.

4.2. Wave Attenuation Characteristics of Different Materials. In the experiment, the signal generated by the by broken pencil is very weak. A lead signal was measured every 10 mm away from the center of the sensing element in the polarization direction of the sensing element, and the corresponding surface wave amplitude is calculated. Figure 7 shows the distance-amplitude curve. The results show that the maximum propagation distance measured in the iron plate is 460 mm, and the attenuation is observed up to a distance pf 260 mm. In case of the concrete specimen, the maximum distance measured is 300 mm, and the attenuation is observed up to a maximum distance of 150 mm. The results show that the amplitude of the wave decreases with propagation distance for both concrete and iron plates. However, the wave attenuates quickly, with propagation distance, in concrete compared to iron. In order to study the attenuation performance of surface wave, a mathematical

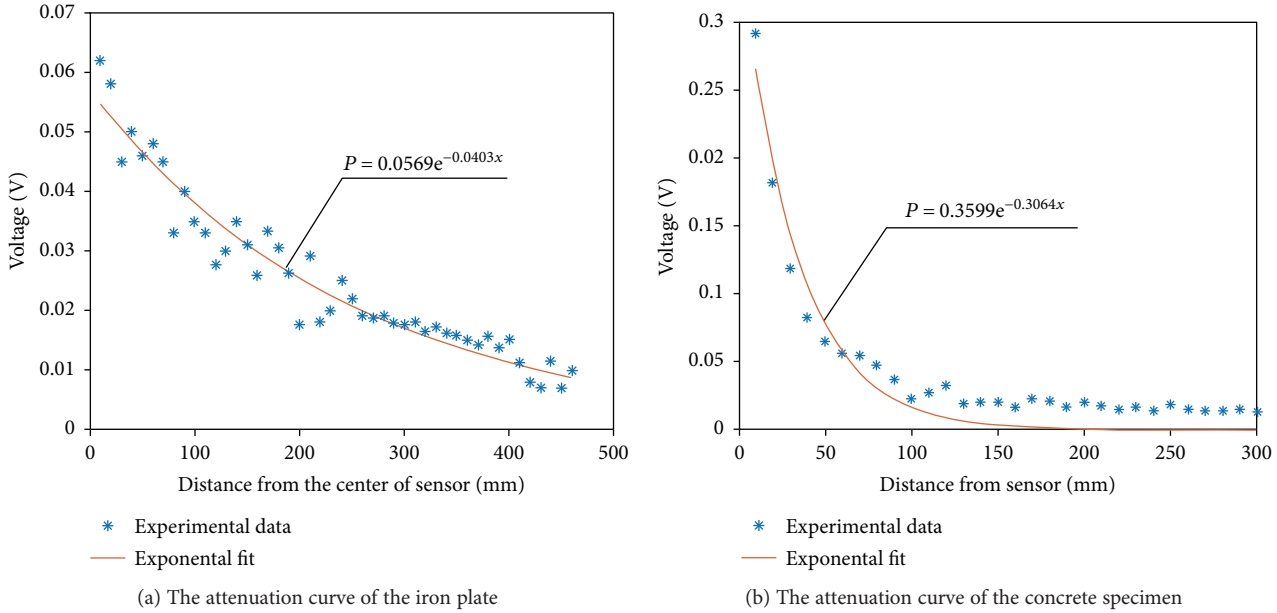

(a) The attenuation curve of the iron plate

(b) The attenuation curve of the concrete specimen

Figure 7: Relation between peak value and propagation distance.

fit is obtained from the amplitude data of Figure 7 and the propagation distance. The results show that the amplitude peak shows an exponential decline with the propagation distance x as shown in Figure 7. The attenuation law of the surface wave is an exponential decay, which can be expressed as $P = Ae^{-nx}$, where A is the constant related to the material, and n is the attenuation coefficient that controls the surface waves decay rate. Figure 7 shows that the attenuation coefficients of SAW are 0.0403 and 0.3064 in iron and concrete specimen, respectively. It has provided a method to test the attenuation coefficients.

5. Conclusions

The developed AE tests are successfully conducted to study the wave propagation phenomena in the iron plate and concrete specimens using the 1-1 OPCM sensor. The single-point frequency-amplitude test results in its resonant frequency, which proves the feasibility of the AE broken pencil signal test and can be used in subsequent experiments to provide excitation frequency selection. The experiment is conducted multiple times on the same material using different OPCM sheets. The attenuation characteristics of the surface wave and wave speeds are obtained from the experiments. The attenuation characteristics of surface wave generated by the AE simulation source in iron and concrete materials are studied. The characteristics of the surface wave and its propagation velocity in different materials are analyzed. The waveforms recorded at different positions on iron and concrete plates show that the increasing peak values of the surface wave deviated from the sensing element are decreased rapidly exponentially and decayed rapidly in concrete. According to the material attenuation coefficient obtained experimentally, it can provide guidance for the study of amplitude compensation and impedance matching in multielement transducers.

Conflicts of Interest

The authors declare that there is no conflict of interests regarding the publication of this paper.

Acknowledgments

This work was financially supported by the National Natural Science Foundation of China (Grant nos. 11402101 and 11520101001) and Jiangsu University Foundation (14JDG022).

References

[1] J. Y. Kim and S. I. Rokhlin, "Surface acoustic wave measurements of small fatigue cracks initiated from a surface cavity," *International Journal of Solids and Structures*, vol. 39, no. 6, pp. 1487–1504, 2002.

[2] C. Y. Cheng, S. S. Huang, C. M. Yang, K. T. Tang, and D. J. Yao, "Detection of third-hand smoke on clothing fibers with a surface acoustic wave gas sensor," *Biomicrofluidics*, vol. 10, no. 1, article 011907, 2016.

[3] R. Yasukuni, R. Fukushima, T. Iino, and Y. Hosokawa, "Pulsed-laser-activated impulse response encoder: sensitive detection of surface elastic waves on biomimetic microsized gel spheres," *Applied Physics Express*, vol. 10, no. 11, article 117001, 2017.

[4] M. F. Lewis, "Rayleigh waves-a progress report," *European Journal of Physics*, vol. 16, no. 1, pp. 1–7, 1995.

[5] J. Ivanov, C. B. Park, R. D. Miller, and J. Xia, "Analyzing and filtering surface-wave energy by muting shot gathers," *Journal of Environmental and Engineering Geophysics*, vol. 10, no. 3, pp. 307–322, 2005.

[6] B. D. Zaitsev, I. E. Kuznetsova, N. E. Zemnyukov, V. I. Proidakov, and A. A. Teplykh, "Plate acoustic waves for low frequency delay line delaying signals up to 0.5 ms," *Physics Procedia*, vol. 3, no. 1, pp. 533–539, 2010.

[7] F. G. Herring, P. M. Krencik, and C. F. Vasile, "High performance surface-wave pulse compression," in *1973 Ultrasonics Symposium*, pp. 472–477, Monterey, CA, USA, November 1973.

[8] E. A. Ash and E. G. S. Paige, *Rayleigh-Wave Theory and Application*, Springer, Berlin Heidelberg, 1985.

[9] V. Giurgiutiu and J. Bao, "Embedded ultrasonic structural radar with piezoelectric wafer active sensors for the NDE of thin-wall structures," in *ASME 2002 International Mechanical Engineering Congress and Exposition*, pp. 31–38, New Orleans, LA, USA, November 2002.

[10] X. Yan, W. Huang, S. R. Kwon, S. Yang, X. Jiang, and F. G. Yuan, "A sensor for the direct measurement of curvature based on flexoelectricity," *Smart Materials and Structures*, vol. 22, no. 8, article 085016, 2013.

[11] T. Wang, R. Green, R. Nair et al., "Surface acoustic waves (SAW)-based biosensing for quantification of cell growth in 2D and 3D cultures," *Sensors*, vol. 15, no. 12, pp. 32045–32055, 2015.

[12] V. Lonescu, "Design and analysis of a Rayleigh saw resonator for gas detecting applications," *Romanian Journal of Physics*, vol. 60, pp. 502–511, 2015.

[13] Y. Luo and B. Q. Tao, "The OPCM strain gauges for strain and stress measurement of orthotropic material structures," *Acta Mechanica Solida Sinica*, vol. 13, no. 4, pp. 337–345, 2000.

[14] Z. P. Wang, Y. Luo, G. P. Zhao et al., "Design and optimization of an OPFC ultrasonic linear phased array transducer," *International Journal of Mechanics and Materials in Design*, vol. 13, pp. 1–13, 2015.

[15] J. S. Popovics, W. Song, J. D. Achenbach et al., "One-sided stress wave velocity measurement in concrete," *Journal of Engineering Mechanics*, vol. 124, pp. 1345–1353, 2016.

[16] Z. Wang, Y. Luo, and T. Sun, "Design and validation of an orthotropic piezoelectric composite material phased array sensor used to nondestructive detection," *Sensor Letters*, vol. 13, no. 10, pp. 852–856, 2015.

[17] Z. Wang, Y. Luo, G. Zhao, B. Q. Xu, and F. G. Yuan, "Design of an OPCM phased array transducer for damage detection in a concrete structure," *Research in Nondestructive Evaluation*, vol. 27, no. 4, pp. 204–215, 2016.

[18] A. Gu, Y. Luo, and B. Xu, "Continuous condition monitoring of reinforced concrete using an active diagnosis method," *Structural Health Monitoring*, vol. 15, no. 1, pp. 104–112, 2016.